High-Accuracy Optical Clock Based on the Octupole Transition in $^{171}Yb^{+}$

An der Fakultät für Mathematik und Physik der
Gottfried Wilhelm Leibniz Universität Hannover

zur Erlangung des Grades

Doktor der Naturwissenschaften
Dr. rer. nat.

genehmigte Dissertation

von

Nils Huntemann
geboren am 25. Juni 1982 in Kassel

2014

Referent: PD Dr. Ekkehard Peik
Korreferent: Prof. Dr. Piet O. Schmidt
Korreferent: Prof. Dr. Alan A. Madej
Tag der Promotion: 15. Juli 2014

Zusammenfassung

Zeit und Frequenz sind die am genauesten messbaren physikalischen Größen. Nahezu alle höchst präzisen Messverfahren in der Grundlagenforschung und Technik beruhen auf dem Messen und Vergleichen von Frequenzen. Die zugehörige SI Einheit Sekunde wird in Cäsium-Fontänenuhren mit einer relativen Unsicherheit im 10^{-16} Bereich realisiert. Stabilere Frequenzen mit deutlich kleineren systematischen Unsicherheiten lassen sich mit sogenannten optischen Uhren erzeugen, bei denen die Frequenz hoch stabiler Laser auf verbotene optische Übergänge von lasergekühlten, gespeicherten Atomen abgestimmt wird.

Die vorliegende Arbeit diskutiert die Realisierung einer optischen Uhr, die den extrem schmalen $^2\mathrm{S}_{1/2}(F=0) \rightarrow {}^2\mathrm{F}_{7/2}(F=3)$ Oktupol-Übergang eines einzelnen, in einer Paul Falle gespeicherten $^{171}\mathrm{Yb}^+$ Ions als Referenz nutzt. Über die bekannten Vorteile des Systems hinaus, wie die große Masse und eine natürliche Linienbreite im nHz Bereich, ergaben die hier vorgestellten experimentellen Untersuchungen ein überraschend kleines Quadrupol Moment des angeregten Zustands $\Theta(F, 7/2) = -0.041(5)\ ea_0^2$. Desweiteren wurden genaue Sensitivitäten der Übergangsfrequenz für elektrische und magnetische Felder bestimmt, die durch Spektroskopie des zweiten Uhrenübergangs von $^{171}\mathrm{Yb}^+$, dem $^2\mathrm{S}_{1/2}(F=0) \rightarrow {}^2\mathrm{D}_{3/2}(F=2)$ Quadrupol-Übergang, charakterisiert werden können.

Ein hochstabiler Laser ermöglicht die erstmalige experimentelle Untersuchung des sogenannten “hyper-Ramsey” Anregungsverfahren, durch das die dominierende Frequenzverschiebung, die Lichtverschiebung durch den Abfragelaser, um viele Größenordnungen reduziert wird. Abwechselndes Abfragen mit dem neuen Verfahren und mit einzelnen Rabi Pulsen erlaubt eine Steuerung der “hyper-Ramsey” Parameter und garantiert eine dauerhafte Unterdrückung der Lichtverschiebung, sodass diese nur noch einen unwesentlichen Beitrag zur systematischen Unsicherheit des Normals liefert.

Die Frequenzverschiebung durch thermische Strahlung wurde mit Hilfe nahinfraroter Laserstrahlung untersucht und die differentiellen Polarisierbarkeiten für beide Uhrenübergänge bei verschiedenen Wellenlängen bestimmt. Diese Daten können für Tests theoretischer Untersuchungen dienen und ermöglichen derzeit eine Korrektur der Verschiebung für den Oktupol-Übergang mit einer relativen Unsicherheit von 2.6×10^{-18} und einen Bestimmung der differentielle statische skalare Polarisierbarkeit $\Delta\alpha_s^{dc} = 0.893(30) \times 10^{-40}\mathrm{Jm}^2\mathrm{V}^{-2}$.

Die Frequenzen beider Uhrenübergänge wurden bestimmt, wobei die erzielte Unsicherheit im wesentlichen durch die der Fontänenuhren limitiert war. Durch den Vergleich mit einer optischen Gitteruhr ergab sich die Instabilität des Oktupol-Frequenznormals zu $\sigma_y(\tau) = 5.3 \times 10^{-15}/\sqrt{\tau(\mathrm{s})}$. Eine Abschätzung aller relevanter frequenzverschiebender Effekte ergibt gegenwärtig eine relative systematische Unsicherheit von 3.9×10^{-18}, was vermutlich die derzeit kleinste aller Atomuhren darstellt.

Stichworte: Optisches Frequenznormal, stabile Laser, Präzisionsspektroskopie.

Abstract

Time and frequency are the most precisely measurable physical quantities. Nearly all of the high precision measurement techniques in basic research and engineering are based on the measurement and comparison of frequencies. The associated SI unit second is realized by caesium fountain clocks with a relative uncertainty in the 10^{-16} range. More stable frequencies with considerably smaller systematic uncertainties can be generated by so-called optical clocks, in which the frequency of highly stable lasers is referenced to forbidden optical transitions of laser-cooled trapped atoms.

This thesis discusses the realization of an optical clock based on the extremely narrow $^2\mathrm{S}_{1/2}(F=0) \rightarrow {}^2\mathrm{F}_{7/2}(F=3)$ octupole transition of a single $^{171}\mathrm{Yb}^+$ ion confined in a Paul trap as the reference. Beyond the known advantages of the system, like the large mass and a natural linewidth in the nHz range, the experimental investigations presented here reveal a surprisingly small quadrupole moment of the excited state $\Theta(F, 7/2) = -0.041(5)\ ea_0^2$. Furthermore, precise sensitivities of the transition frequency to electric and magnetic fields have been determined. These fields can be characterized by spectroscopy on the second clock transition of $^{171}\mathrm{Yb}^+$, the $^2\mathrm{S}_{1/2}(F=0) \rightarrow {}^2\mathrm{D}_{3/2}(F=2)$ quadrupole transition.

A highly stable laser permits the first experimental investigation of the so-called "hyper-Ramsey" excitation scheme that reduces the dominating frequency shift, the light shift induced by the probe laser, by several orders of magnitude. Alternating interrogation with the new method and with single Rabi pulses enables control the "hyper-Ramsey" parameters and guarantees a constant suppression of the light shift, so that its contribution to the systematic uncertainty of the standard is negligible.

The frequency shift induced by thermal radiation was studied via the effect of near-infrared laser radiation and the differential polarizabilities have been determined for both clock transitions at various wavelengths. These data can be used for tests of theoretical predictions and currently permit a shift correction for the octupole transition with a relative uncertainty of 2.6×10^{-18} and to infer the static differential scalar polarizability $\Delta\alpha_s^{dc} = 0.893(30) \times 10^{-40}\mathrm{Jm}^2\mathrm{V}^{-2}$.

The frequencies of both clock transitions have been measured with an uncertainty essentially limited by that of the caesium fountain clocks. The comparison with an optical lattice clock yields the instability of the octupole frequency standard to be: $\sigma_y(\tau) = 5.3 \times 10^{-15}/\sqrt{\tau(\mathrm{s})}$. An evaluation of all relevant frequency shift effects leads at present to a relative systematic uncertainty of 3.9×10^{-18}, which appers to be the smallest among all atomic clocks.

Keywords: optical frequency standard, stable lasers, precision spectroscopy.

Contents

1 Introduction

Time has ever been a mystery for mankind, something that is not easy to describe, and that is perceived in very different ways. One way of experiencing time is the observation of periodic phenomena. This leads to Einstein's idea: *It might appear possible to overcome all the difficulties attending the definition of "time" by substituting "the position of the small hand of my watch" for "time"* [1]. In this respect, time can be measured by counting the number of passing cycles of a stable periodic process. Such a phenomenon is provided by the rotation of celestial bodies and served as a reference for the second by the definition as *1/86 400 of the mean solar day* until 1956. However, measurements with quartz oscillators showing irregularities in the rotation of the earth made this an unsatisfactory definition [2,3]. But also the frequency provided by quartz oscillators is neither absolutely stable nor reproducible, but critically depends on temperature.

The most stable frequencies known so far are those of radiation corresponding to transitions between two states of unperturbed atoms. Furthermore, according to the equivalence principle, these frequencies should be independent on place and time. We also believe that they are specific and highly reproducible, since atoms of the same species are identical. As a consequence, atomic transitions seem to provide ideal frequency references.

The most common way to realize an atomic frequency standard is the following: Atoms are prepared in a well defined state and are interrogated on a narrow atomic transition by radiation generated from a stable oscillator. A discriminator signal can be generated by observing changes in the transition probability, while stepping the frequency of the radiation. The generated signal is used in a feedback loop to control the frequency of the oscillator and ensures that the oscillator's frequency corresponds to the atomic resonance. Imperfections in the measurement process and perturbations of the atomic states by residual fields, however, cause a frequency offset between the unperturbed transition frequency ν_0 and that of the oscillator. The relative uncertainty $\delta\nu/\nu_0$ of the applied correction determines the accuracy of the realized frequency standard. This uncertainty estimate can be tested in comparisons with other standards, providing confidence in the evaluated correction and the realization of the unperturbed frequency or guiding toward undiscovered effects.

The first realization of such an atomic clock was achived in 1955 at the National Physical Laboratory (UK) referencing the hyperfine transition of the ground state of caesium atoms [4, 5]. Since this type of clock showed advantages over systems

based on other atomic transitions within the following years, in 1967/68 the 13$^{\text{th}}$ Conférence Générale des Poids et Mesures decided to define the SI second based on the most precise measurement of the Cs-clock frequency in terms of ephemeris time [6], as:

The second is the duration of 9 192 631 770 periods of the radiation corresponding to the transition between the two hyperfine levels of the ground state of the caesium 133 atom.

These atomic clocks made use of Ramsey's method of separated oscillatory fields which permitted the recording of a resonance line shape with a width that is essentially limited by the Fourier-transform of the total interaction time, without shifts and broadening through inhomogeneous excitation [7]. The interaction time is in turn limited by the velocity of the thermal atoms traveling along the Ramsey cavity. In laboratory systems of typical length ≈1 m, interrogation periods of ≈10 ms are achieved corresponding to a resonance width of 50 Hz.

The advent of laser cooling enabled the realization of the atomic fountain clock [8, 9], where a laser-cooled cloud of atoms is launched against gravity using laser light. On their way up, the atoms pass a microwave cavity. After reaching a height of typically 1 m, they fall down, passing the cavity a second time. In this way, the spatially separated oscillatory fields of the beam clocks are replaced by two temporally separated interactions with the microwave field [10]. The separation of the two interaction periods of about 0.5 s allows for observation of the resonance signal with a width of 1 Hz. With the 50 times reduced linewidth, and the comparably smaller velocity of the Cs atoms, the SI second can nowadays be realized in caesium fountain clocks with fractional frequency uncertainties slightly larger than 10^{-16} [11, 12].

1.1 Characterization of frequency standards

Atomic frequency standards are typically characterized by their accuracy and instability. As mentioned before, the accuracy is related to the systematic uncertainty in effects that alter the standard's frequency from that of the unperturbed atomic resonance. The other main property of a frequency standard is its instability that specifies how the observed frequency fluctuates and drifts over time. Thus a reference needs to be generated by another clock to detect the fluctuations, in other words, frequency instability is the result of a relative frequency measurement. Most commonly, the instability is quantified by the Allan deviation [13]

$$\sigma_y(\tau) = \sqrt{\frac{1}{2(M-1)} \sum_{i=1}^{M-1} (y_{i+1} - y_i)^2}, \tag{1.1}$$

where y_i is a set of M frequency measurements that consists of individual measurements equally spaced in segments of duration τ. If the comparison comprises at least three uncorrelated standards, the individual instabilities can be inferred [14]. Compared to the standard deviation, the Allan deviation has the advantage that it does converge for flicker frequency noise. If the Allan deviation is also calculated for larger measurement intervals obtained by averaging over periods of single frequency measurements, types of oscillator and measurement system noise can easily be identified in a double logarithmic plot of the Allan variance versus the averaging time as shown in Fig. 1.1. With the information on the noise type, the averaging time required to reduce the statistical uncertainty of a frequency comparison to a certain level can be inferred. Note that the Allan deviation does not distinguish between white phase noise and flicker phase noise.

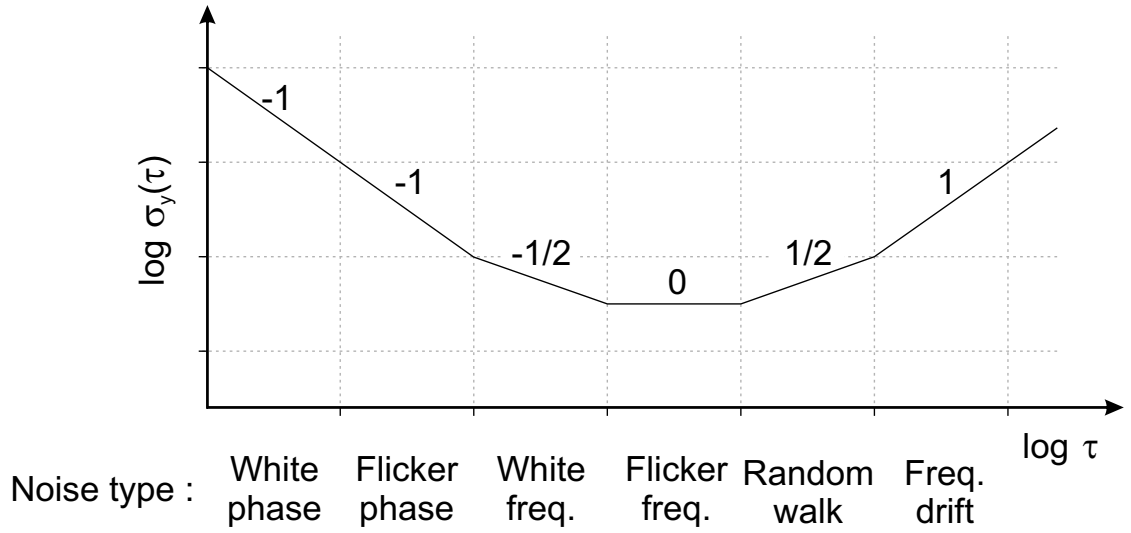

Figure 1.1: Allan deviation $\sigma_y(\tau)$ versus the averaging time τ for 5 different noise types and a constant frequency drift. The numbers are the slope of $\sigma_y(\tau)$ in a double logarithmic plot.

As a consequence of the quantum nature of the atomic resonance [15], the instability at an averaging time τ of an ideal atomic frequency standard, as introduced above, can be described by

$$\sigma_y(\tau) = \frac{\Delta\nu}{\nu_0}\frac{1}{K\sqrt{N}}\sqrt{\frac{T_c}{\tau}}, \tag{1.2}$$

where N is equal to the number of interrogated atoms, assuming an uncorrelated atomic state, K is on the order of unity and depends on the shape of the resonance signal observed around the transition frequency ν_0, and the $\Delta\nu$ describes the width

of the observed resonance feature. The latter is inversely proportional to the interrogation time T_i, which is a part of the total duration of an interrogation cycle T_c.

From Eq. 1.2 it is clearly visible that a large number of atoms, narrow linewidths obtained by long coherent interactions, and in particular high transition frequencies are desirable. It should be noted that the necessary measurement time to achieve a given statistical uncertainty is reduced with ν_0^2 for otherwise unchanged parameters.

1.2 Optical frequency standards

Pursuing the idea of atomic clocks based on transitions with higher frequencies lead to constraints set by the availability of controllable local oscillators and instruments to compare and count the realized frequencies. Both such tools have recently become available for frequencies in the optical spectrum: lasers whose frequencies are stabilized to optical resonators [16,17] provide short-term instabilities presently approaching the 10^{-17} range [18] and optical frequency comb generators provide a convenient tool to phase-coherently compare frequencies in the optical and the microwave regime with uncertainties in the 10^{-19} range [19, 20].

Equally important milestones for frequency standards based on narrow optical transitions have been passed by trapping and cooling thousands of neutral atoms in optical lattices [21, 22] or single ions in radio frequency traps [23–25]. The precise control of the motion of the trapped particles prevents large Doppler shifts and allows for recoil-free spectroscopy with interaction times limited by the short-term instability of the probe laser system.

Since the beginning of this century, optical frequency standards employing various atomic species and reference transitions are investigated in many laboratories worldwide. Profiting from their $\approx 10^5$ times larger transition frequency, so-called optical clocks achieve significantly smaller uncertainties and instabilities than their microwave counterparts [26–34]. While clocks based on neutral atoms confined in an optical lattice have demonstrated superior instabilities resulting from the large number of atoms [35], single-ion clocks were known for their significantly smaller systematic uncertainties [27], due to the smaller sensitivities of their reference transition frequencies to external fields, in particular to that of thermal radiation. Recently, high-accuracy measurements of this sensitivity [34, 36–38] in combination with precise characterization of the radiation field at the position of the atoms [32, 39] or application of cryogenic environments for the atoms [40] have permitted comparable uncertainties for optical lattice clocks [32, 34]. Ultimately, the accuracy of lattice clocks might be limited by residual interaction effects of the atoms.

The outstanding precision of optical clocks makes them of interest as sensitive probes in areas such as relativistic geodesy [41], where the gravitational redshift

of distant clocks is evaluated to determine the difference of the gravity potential between the positions of the clocks. On the contrary, these clocks can be used to test the fundamental assumption for relativistic geodesy, the local position invariance, e.g. by comparing the redshift observed with clocks based on different transitions [42, 43]. Since the local position invariance also refers to position in time, temporal variations of fundamental constants are investigated by repeated comparisons of transition frequencies with different sensitivities on the constants [26, 44–47]. The octupole transition of $^{171}Yb^{+}$ is known for its particularly high sensitivity on the finestructure constant α [63].

1.3 Optical frequency standards with a single $^{171}Yb^{+}$ ion

At the Physikalisch-Technische Bundesanstalt (PTB) we investigate optical frequency standards based on the narrow transitions provided by a single $^{171}Yb^{+}$ ion confined in a radio frequency Paul trap [23]. $^{171}Yb^{+}$ provides several advantages, some of which are obvious from the term diagram depicted in Figure 1.2. The indicated transitions for laser-cooling, repumping and the so-called clock transitions are at convenient wavelengths and thus can all be driven by external-cavity diode laser systems, which reduces the technical efforts and improves the reliability of the system. The ion shows extremely long storage times, probably related with the fact that the 370 nm laser light used for cooling should also be capable to photo dissociate the YbH^{+} molecule [49]. This might explain, why Yb^{+} is used in various experiments with traped ions [50–55]. The relatively large mass of the ion and a convenient linewidth of the cooling transition lead to a small residual motion after Doppler cooling. The corresponding small Doppler shifts are advantagous for the realization of an optical frequency standard. Furthermore, due to the nuclear spin of 1/2, the clock transitions can be excited between $m_F = 0$ components of the hyperfine manifold, so that the transition frequencies are insensitive to small magnetic fields.

Aside from these technical advantages, $^{171}Yb^{+}$ is of particular interest since it offers two optical reference transitions with high quality factor which have rather different physical characteristics. An optical frequency standard based on the electric quadrupole (E2) transition connecting the $^2S_{1/2}(F = 0)$ ground state with the $^2D_{3/2}(F = 2)$ state that has a natural lifetime of 53 ms [56], has been pioneered at PTB [57] and has been established as one of the secondary representations of the SI second [58]. The electric octupole (E3) transition between the ground state and the $^2F_{7/2}(F = 3)$ state was first studied at the National Physical Laboratory (UK) [59]. The extraordinary features of this transition result from the long natural lifetime of the $^2F_{7/2}$ state in the range of several years [59, 60] and from its

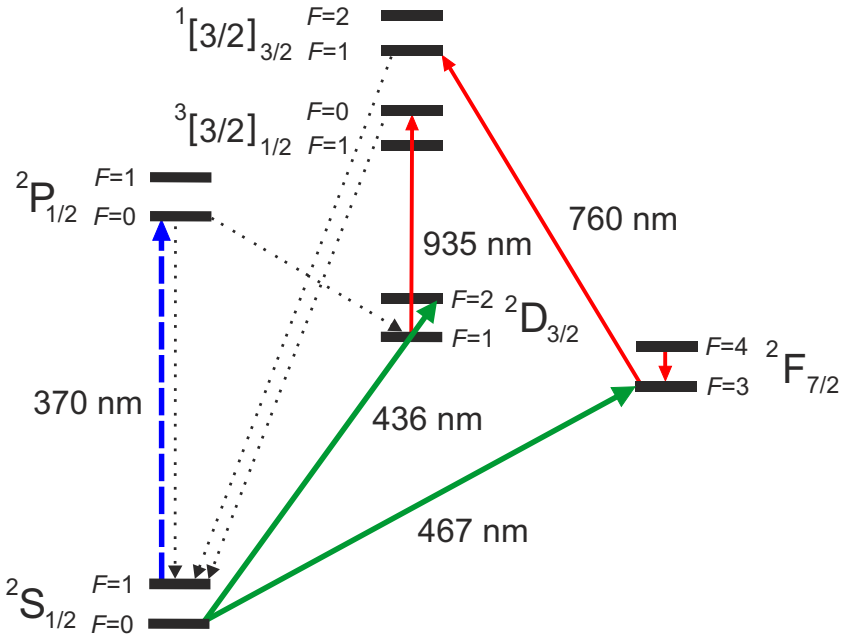

Figure 1.2: Partial level scheme of $^{171}Yb^+$. The solid green arrows indicate the reference transitions: The octupole (E3) transition at 467 nm and the quadrupole (E2) transition at 436 nm. The cooling transition is shown blue dashed and red arrows represent repumping transitions. Relevant spontaneous decay paths are indicated by dotted lines.

electronic configuration ($4f^{13}6s^2$) consisting of a hole in the $4f$ shell surrounded by a spherically symmetric $6s$ shell. Since the octupole transition can be resolved with a linewidth that is virtually unaffected by spontaneous decay and determined only by the available laser stability, a quantum projection noise limited single-ion frequency standard with very low instability can be realized.

To understand the very specific electronic structure of singly-ionized ^{171}Yb, it is helpful to separate the low lying states into two groups. An alkali-like configuration: comprising a completely filled $4f$ shell and a single valence electron, and a two-valence-electron configuration with a hole in the 4f shell. The $^2S_{1/2}$ ground state, the upper level of the cooling transition ($^2P_{1/2}$) and the excited state of the quadrupole transition discussed here, the $^2D_{3/2}$ state, belong to the alkali-like group. The $^2F_{7/2}$ state and the excited states of the repump transitions belong to the other. It seems to be intuitive that LS coupling is appropriate for the $^2F_{7/2}$ state, since it is well characterized as a single hole state. For most of the others low-lying excited states of the same part of the term scheme, however, another coupling scheme is appropriate, to which some refer as JK and others as J_1L_2 coupling [61]. Here, the total angular momentum of parent-level J_1, describing the inner part of the electronic system, couples to the orbital angular momentum of

the valence electrons L_2 obtaining the quantum number K. The spin of the valence electrons S_2 is then coupled with K to obtain the total angular momentum J of the level with the term symbol $^{2S_2+1}[K]_J$.

As a consequence of the complicated electronic structure, strong limitations are expected in a monovalent theoretical description, but a treatment of all 15 valence electrons makes the calculation very difficult, so that currently no precise theoretical predictions for the atomic parameters are available [62].

These difficulties were also limiting *ab initio* calculations of the dependence of the electronic structure on variations of the fine structure constant α. Here, significantly larger relative uncertainties are acceptable, as the very large relativistic contributions to the $^2\mathrm{F}_{7/2}$ state energy $[\Delta(E(^2\mathrm{F}_{5/2}) - E(^2\mathrm{F}_{7/2}))/h \approx 300$ THz] lead to a particularly strong sensitivity of the octupole transition frequency on α [48, 63]. It has also been found that the corresponding transition frequency shift of the quadrupole transition is ≈6 times smaller, but has the opposite sign. Therefore, measurements of the frequency ratio of the quadrupole and the octupole transition in one trapped $^{171}\mathrm{Yb}^+$ ion are a convenient way to test the constancy of α.

The octupole transition has been known to be an attractive reference transition [64], but because of the extremely small oscillator strength of the octupole transition, which is about 8 orders of magnitude smaller than that of most other transitions used in optical clocks, its excitation requires particularly high spectral power density. To achieve π-pulse excitation by a 30 ms long rectangular pulse, an intensity of 10 W/mm^2 is required. This large intensity leads to nonresonant couplings to higher-lying levels and thereby introduces a significant light shift (≈500 Hz) of the transition frequency. This strong light shift and the difficulty to efficiently excite the octupole transition have impeded the realization of an optical frequency standard and detailed investigations of systematic shifts, which are both presented in this thesis.

1.4 Outline of the Thesis

This thesis describes the realization of an optical frequency standard based on the octupole transition of a single $^{171}\mathrm{Yb}^+$ ion and reports on the present status of a frequency standard based on the quadrupole transition.

The main concepts and components of the experimental setup are introduced in chapter 2. A short discussion of the principles of trapping and cooling single ions is given and a new repump transition that can efficiently depopulate the long living $^2\mathrm{F}_{7/2}$ state is reported. High resolution spectroscopy on the octupole transition is achieved with a new probe laser system.

In chapter 3 shift effects of the $^2\mathrm{S}_{1/2}(F=1) \rightarrow {}^2\mathrm{D}_{3/2}(F=2)$ transition and the $^2\mathrm{S}_{1/2}(F=1) \rightarrow {}^2\mathrm{F}_{7/2}(F=3)$ transition due to external fields are evaluated by measuring the relevant atomic parameters, for instance the quadrupole moment $\Theta(F, 7/2)$, differential electric polarizabilities and sensitivities to the second-order Zeeman shift. Finally, present estimates for all known relevant systematic frequency shifts and the corresponding uncertainties of the $^{171}\mathrm{Yb}^+$ standards are given.

In chapter 4 the recently proposed "hyper-Ramsey" spectroscopy is experimentally investigated and its application in an optical frequency standard is demonstrated.

In chapter 5 comparisons of the two optical frequency standards of $^{171}\mathrm{Yb}^+$ with caesium fountain clocks are presented. These results might be used for tighter constraints on temporal variations of fundamental constants.

1.5 Publications

Parts of the work presented here, have been previously published as listed below.

The realization of an optical frequency standard based on the octupole transition using a real-time extrapolation technique to cancel the light shift, a measurement of the transition frequency versus a fountain clock, first measurements of the static scalar differential polarizability of the octupole transition and the quadrupole moment of the $^2\mathrm{F}_{7/2}$ state:

- N. Huntemann, M. Okhapkin, B. Lipphardt, S. Weyers, Chr. Tamm, and E. Peik, Phys. Rev. Lett. **108**, 090801 (2012).

The first experimental demonstration of the so-called "hyper-Ramsey" spectroscopy method without its application in a frequency standard:

- N. Huntemann, B. Lipphardt, M. Okhapkin, Chr. Tamm, E. Peik, A. V. Taichenachev, and V. I. Yudin, Phys. Rev. Lett. **109**, 213002 (2012).

The first measurement of an optical transition frequency with a caesium fountain clock using an optically stabilized microwave oscillator demonstrated on the quadrupole transition of $^{171}\mathrm{Yb}^+$:

- Chr. Tamm, N. Huntemann, B. Lipphardt, V. Gerginov, N. Nemitz, M. Kazda, S. Weyers, and E. Peik, Phys. Rev. A **89**, 023820 (2014).

The measurement of the octupole transition frequency versus two fountain clocks has been used to infer the $5\mathrm{s}^2\,{}^1\mathrm{S}_0 \rightarrow 5\mathrm{s}5\mathrm{p}\,{}^3\mathrm{P}_0$ transition frequency of $^{87}\mathrm{Sr}$ based on the frequency ratio of the two optical frequency standards:

- S. Falke, N. Lemke, C. Grebing, B. Lipphardt, S. Weyers, V. Gerginov, N. Huntemann, C. Hagemann, A. Al-Masoudi, S. Häfner, S. Vogt, U. Sterr, and C. Lisdat, New J. Phys. **16**, 073023 (2014).

Parts of the calculations of electric polarizabilities were given in

- V. I. Yudin, A. V. Taichenachev, M. V. Okhapkin, S. N. Bagayev, Chr. Tamm, E. Peik, N. Huntemann, T. E. Mehlstäubler, and F. Riehle, Phys. Rev. Lett. **107**, 030801 (2011).

2 Experimental Setup

This chapter will introduce the main concepts and components of the experimental setup. It starts with a short discussion of the principles of trapping and cooling single ions, followed by a report on a new repump transition that more rapidly depopulates the long living $^2\mathrm{F}_{7/2}$ state. Furthermore, the basic interrogation sequence and its elements will be described. Finally, the last part of this chapter deals with a new probe laser system to excite the octupole transition offering several advantages over a previously used one [65].

2.1 Trapping and Cooling of a Single Yb^+ Ion

The basic idea to investigate properties of the unperturbed atomic structure via precision spectroscopy of trapped ions was introduced in 1956 by Hans Dehmelt [66]. He proposed to trap ions in a small volume for a time that is significantly longer than it would be achievable for example in double resonance experiments in vapor cells. A convenient experimental instrument to realize trapping, ideally for an infinite amount of time, is the three dimensional quadrupole ion trap invented by Wolfgang Paul [23]. As seen from the Laplace equation an attractive potential to confine the ion cannot be realized by static electric fields, however, dynamical trapping can be achieved by the use of time dependent electric fields. The electrodes of our Paul trap (see Fig. 2.1) are machined according to number 4 in Ref. [67] scaled to match $z_0 = 1$ mm. The time dependent electric potential inside the trap with a characteristic size r_0 is

$$\phi(\mathbf{r}, t) = (U_0 + V_0 \cos(\Omega t)) \frac{(1+\epsilon)x^2 + (1-\epsilon)y^2 - 2z^2}{\kappa r_0^2}. \tag{2.1}$$

The voltage applied to the central ring electrode is comprised of a static component U_0 and a dynamical contribution of amplitude V_0 oscillating at an angular frequency of Ω. The shape of the electrodes determines the coefficient κ, where $\kappa = 2$ corresponds to electrodes that perfectly match a hyperbolic equipotential surface and should equal 2.16 for our trap geometry [67]. Deviations from a cylindrical symmetry of the trap potential are described by ϵ. The motion of the single ion with a mass m and the charge Q in this potential can be described by a set of Mathieu equations

$$\frac{\mathrm{d}^2 r_i}{\mathrm{d}\tau^2} + (a_i - 2q_i \cos 2\tau) = 0 \tag{2.2}$$

with the dimensionless parameters

$$a_i = \frac{8\gamma_i Q U_0}{m\Omega^2 \kappa r_0^2}, \quad q_i = \frac{4\gamma_i Q V_0}{m\Omega^2 \kappa r_0^2}, \quad \tau = \frac{\Omega}{2}t, \quad \gamma_i = \begin{cases} 1+\epsilon & i = x \\ 1-\epsilon & i = y \\ -2 & i = z. \end{cases} \tag{2.3}$$

In the case of $|a_i|, q_i \ll 1$ and $U_0 < V_0$ stable solutions of Eq. 2.2 can be written as

$$r_i(\tau) = \underbrace{r_i \cos\frac{2\omega_i \tau}{\Omega}}_{\text{secular motion}} + \underbrace{\left(r_i \cos\frac{2\omega_i \tau}{\Omega}\right)\frac{q_i}{2}\cos 2\tau}_{\text{micromotion}}, \qquad i = x, y, z. \tag{2.4}$$

Here one can clearly see two separable parts of the motion and their correlation. The second part describes the oscillation of the ion with the frequency of the radio frequency voltage that creates the trap field. For averaging times larger than $1/\omega$, the mean kinetic energy of the micromotion forms a pseudo-potential

$$\Phi(r_i) = \frac{m}{4Q}\omega_i^2 r_i^2. \tag{2.5}$$

So that the first part of Eq. 2.4 can be interpreted as the harmonic motion in this pseudo-potential. According to [68] the frequency of the secular motion is

$$\omega_i = \frac{\Omega}{2}\sqrt{a_i - \frac{(a_i-1){q_i}^2}{2(a_i-1)^2 - {q_i}^2} - \frac{(5a_i+7){q_i}^2}{32(a_i-1)^3(a_i-4)}} \tag{2.6}$$

which simplifies for the approximation $|a_i|, q_i \ll 1$ to

$$\omega_i = \frac{\Omega}{2}\sqrt{a_i + \frac{1}{2}{q_i}^2}. \tag{2.7}$$

Residual stray electric fields or effective phase differences of the potentials on the electrodes can shift the equilibrium position of the ion from the trap center. In this case the ion will not be located in the field free trap center but will be affected by so-called excess micromotion. The additional mean squared field and the induced motion of the ion can cause significant shifts of the observed transition frequencies of the trapped particle via the quadratic Stark and the quadratic Doppler effect, respectively. Different methods were investigated to detect micromotion [69]. A cancellation of the residual field can be achieved by applying a compensating electric field. Figure 2.1 is a picture of the trap used in the experiments. Due to their proximity, voltages on the electron gun, the Yb oven and between the endcap electrodes can be used to null the electric field at trap center. The compensation field is adjusted by minimizing residual changes of the mean position of the ion that are associated with lowering the trap potential close to the boundary of the stable

region [70]. The position is visible on a monitor screen that shows a magnified image of the ion in the trap detected on an intensified CCD camera. By choosing a positive or a negative offset voltage on the ring electrode, the trap becomes shallow either along the trap axis or in the radial plane. Due to the large magnification and the orientation of the trap relative to the detector, changes of the mean position of the ion related with the electric field induced by the compensation voltages are distinguishable and clearly visible. The quality of the compensation can be assumed to be similar for the three orientations. In particular, the voltage adjustment between the endcaps serves as a test case. From repeated compensation procedures with very different initial voltages, the reproducibility of the compensation voltage is found to be better than 3 mV, which is assumed as the uncertainty for this compensation voltage. With a finite element calculation, the electric field E_z along the trap axis resulting from a dc voltage U between the two endcap electrodes at a distance of $2z_0$ was calculated to be

$$E_z = k\frac{U}{2z_0}, \quad k = 0.80. \tag{2.8}$$

The design goal of $2z_0$ was 0.987 mm, which should be realized with an uncertainty of a few percent. This leads to a comparable uncertainty of the electric field, since the imperfections of the numerical calculation are expected to be much smaller. With Eq. 2.8 a residual electric field of less than ± 2.4 V/m along the trap axis can be calculated from the uncertainty of the voltage used to compensate stray electric fields. This residual field can shift the ion from the minimum of the trap potential along the trap axis. For the two orthogonal orientations similar residual fields are expected.

Ions are created inside the trap potential for example by photoionization or electron impact ionization and can be expected to possess initial kinetic energy on the order of 1 eV. The motional energy of the trapped particles needs to be reduced to a regime where the associated Doppler broadening will not dominate the observed resonance spectra linewidth, but the ion is localized significantly better than the wavelength of the interrogating laser light field. As it can be seen from Eq. 2.4, a reduction of secular motion will also reduce the corresponding part of the micromotion. In 1975 Wineland and Dehmelt as well as Hänsch and Schawlow proposed the idea of laser cooling for electromagnetically trapped ions and a gas of neutral atom. Near resonant laser light can be employed to achieve optical pumping into low lying motional states. In 1978 cooling of ions using a red detuned laser was first demonstrated by Wineland, Drullinger and Walls [71] on Mg+ ions in a Penning trap, and independently by Neuhauser *et al.* [24] on Ba^+ ions in a Paul trap. The same technique that was applied to cool Ba^+ ions, is used in the experiments described here, to reduce the kinetic energy of a single trapped Yb^+ ion by scattering photons on the strong $^2S_{1/2}(F = 1) \rightarrow {}^2P_{1/2}(F = 0)$ transition at 370 nm.

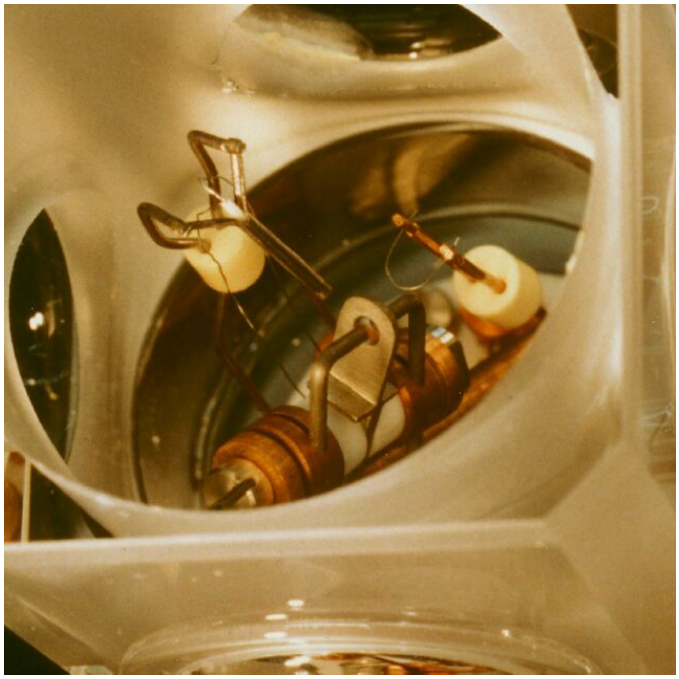

Figure 2.1: Picture of the ion trap in its quartz glass vacuum chamber. The Yb^+ oven is visible on the left and the electron source on the right. The picture has been taken through the window used for fluorescence detection. Attached to the central glass cube, the four orthogonal tubes for the cooling, probe and repump laser beams can be seen on the outer part.

A review of the basic concepts of laser cooling is given in [72] and in more detail laser cooling of ions is described in [73–75]. In our experiments the cooling transition is excited by a frequency doubled external cavity diode laser providing 10 μW of power that is focused to a beam waist of $\approx$50 μm at the position of the ion in the trap [76]. A few milliwatts of light from another external-cavity diode laser at 935 nm are focused to a similar beam waist in order to avoid population trapping in the $^2D_{3/2}$ metastable level. The so-called repump laser excites the ion to the short living $^3[3/2]_{1/2}$ manifold, which in turn decays predominantly to the ground state [77]. A microwave sideband at 14.7 GHz on the cooling laser depopulates the lower lying hyperfine level ($F = 0$) of the ground state and by that closes the cooling cycle. A strong magnetic field under an angle to the laser polarization leads to an appropriate splitting of the Zeeman manifold, and ensures that population trapping in Zeeman sublevels of the $^2S_{1/2}(F = 1)$ state does not prevent efficient laser cooling [78]. The absolute value of the magnetic field and the polarization of the cooling laser light are adjusted to maximize the fluorescence rate, whereas the cooling light intensity is reduced to prevent saturation. Under

these conditions, the frequency of the cooling light is detuned by about half of the natural linewidth of 19.6 MHz [79] and leads to $\approx 10^4$ detected photons per second.

A more detailed discussion of the cooling process as well as its limitations in the case of a single $^{171}Yb^+$ ion can be found in chapter 3 of Ref. [80] and in Ref. [78]. For the experiments discussed here, it should be sufficient to summarize some of their results and discuss related limitations. The process of cooling the ion is carried out under the assumption of a weak binding ($\omega_i \ll \Gamma$) of the ion in the trapping potential. Since the spontaneous decay rate on the cooling transition is much bigger than the angular frequencies of the secular motion. According to [15], where the trap potential is approximated to be a pure one-dimensional harmonic well and low intensities as well as low velocities are assumed, the final steady-state energy after Doppler cooling can be expressed as

$$E_D = (1+\alpha)\frac{\hbar(\Gamma^2 + 4\Delta^2)}{-16\Delta} = \frac{1}{2}k_B T_D. \tag{2.9}$$

Here k_B denotes the Boltzmann constant, α describes the angular distribution of the fluorescence, and is assumed to be equal to 1/3, and Δ is the detuning from the resonance of the cooling transition. The energy is minimal under the condition $\Delta = -\Gamma/2$ and the temperature T_D of the ion at Doppler cooling limit is $T_D = 2\hbar\Gamma/3k_B = 0.63$ mK. The minimum temperature that can be achieved is essentially limited by the natural linewidth of the cooling transition. On general grounds, one expects such a limit for processes in a two-level atom because $\hbar\Gamma$ represents the smallest energy scale in the system. In the case of both clock transitions, the ion is in a regime of strong binding ($\omega_i \gg \Gamma$) and the motional sidebands are well resolved. For low intensities and modulation indices, the amplitude of the observed sidebands at the secular frequency ω_i in comparison with the amplitude of the carrier at the transition frequency ν_0 can be used to calculate the temperature of the ion T_i. According to Refs. [69, 81]:

$$T_i = \frac{2mc^2}{k_B}\left(\frac{\omega_i}{2\pi\nu_0}\right)^2 \sum_{l=1,2,3} R_{l,i}, \tag{2.10}$$

where m is the mass of the ion and c the speed of light. $R_{l,i}$ is the sideband-to-carrier intensity ratio for the laser beam propagation direction l and the secular motion along the principal axis i. In our trap only one beam propagation direction is used, so that it is assumed that the observed energy $k_B \sum_i T_i$ for one direction is equal to 1/3 of the total kinetic energy of the ion. Following this idea, Fig. 2.2 shows a measurement performed on the quadrupole transition of the ratio of the two radial secular sidebands and the carrier intensity as a function of a waiting period after Doppler cooling. The pulse area is adjusted to be smaller than $\pi/2$ and short excitation pulses of 0.5 ms avoid variations of the excitation probability induced by frequency drifts of the probe laser. The excitation probability was

determined from 700 interrogations. In this way, the temperature after Doppler cooling has been measured to be $T = 1.1$ mK which is less than a factor of 2 more than the calculated temperature at the Doppler limit which can be expected since the cooling scheme is not a perfect two level system (see Ref. [78]). The increase of thermal energy with time leads for the quadrupole and the octupole spectroscopy to mean temperatures during the probe pulses of 1.4 mK and 2.0 mK with an interrogation time of 30 ms and 250 ms, respectively. Furthermore, a mean heating rate $d\langle n\rangle/dt = 190(60)$ s^{-1} has been deduced, where $\langle n\rangle$ equals the mean number of motional quanta in one radial harmonic well.

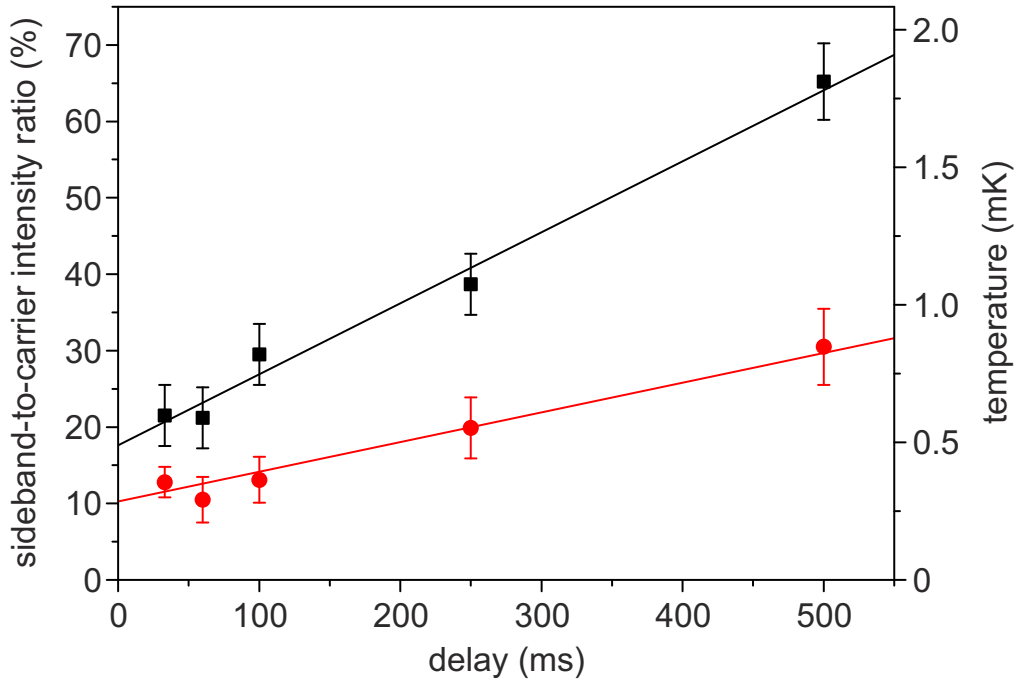

Figure 2.2: Measurements of the sideband-to-carrier intensity ratio with various delays after Doppler cooling for the two sidebands, resulting from radial secular motion of the ion. The intensities are determined as the excitation probability obtained with 700 interrogations using 0.5 ms long pulses. The ratio can be used to calculate the temperature of the ion (see text). The radial sideband frequencies differ by less than 1% and the difference in the observed ratio results presumably from a different orientation of the motion with respect to the cooling laser.

It is possible to further reduce the initial temperature of the ion by scattering photons on the red-detuned secular sidebands of the forbidden quadrupole transition. In this way it would be possible to transfer the ion to the motional ground state of the trap potential, as it was first demonstrated in an experiment with a

single Hg^+ ion [82]. For the experiments described in the following, only Doppler cooling on the 370 nm transition was used.

As a result of the residual secular motion, the ion is affected by the electric field that constitutes the trap potential. Furthermore, uncompensated electric stray fields $\mathbf{E}_{DC}$ can displace the ion's mean position $\mathbf{r\prime}$, so that it does no longer coincide with the minimum of the trap potential. According to Ref. [69] the time averaged square of the electric radio frequency field at the position $\mathbf{r\prime}$ is

$$\langle E_i^2(\mathbf{r\prime})\rangle_i = \frac{m\Omega^2 k_B T_i}{2Q^2}\frac{a_i^2+2q_i^2}{2a_i+q_i^2} + 8\left(\frac{q_i E_{DC,i}}{2a_i+q_i^2}\right)^2. \tag{2.11}$$

The first part results from the secular motion and is equal to 2.0×10^3 V^2/m^2 for an effective temperature $T_i = 1.1$ mK after Doppler cooling for the normal trap parameters $a_i = 0$ and $q_z = 0.22$. For the spectroscopy on the octupole transition with a long interrogation time of ≈250 ms and an increased kinetic temperature, this contribution grows to 2.9×10^3 V^2/m^2. The second part of Eq. 2.11 results from the displacement due to uncompensated electric fields $E_{DC,i}$. Assuming $E_{DC} < 2.4$ V/m for the z-axis as discussed above, the second term is expected to be smaller than 1.0×10^3 V^2/m^2. Therefore, the mean kinetic temperature of the ion causes the larger contribution to the time averaged electric field that induces shifts of the atomic levels via the quadratic Stark effect and thus changes the reference transition frequencies. This shift effect is discussed in detail in section 3.2.

In our experiments the single ion is created inside the trapping field by electron impact ionization of atoms from an ^{171}Yb oven. The trap setup utilized in the experiments offers also the possibility to trap $^{172}Yb^+$ ions created from a second oven, however, this opportunity was not used. Alternatively, ytterbium ions could be produced by photo-ionization [83, 84]. In this case, neutral Yb is resonantly excited by laser radiation at 399 nm from the $^1S_0$ ground state to the $^1P_1$ level from which light of the cooling laser at 370 nm (two-color) or a second photon at 399 nm (one-color) finalizes ionization by promoting an electron to the continuum. This technique is utilized in a second $^{171}Yb^+$ ion trap system at PTB. In contrast to the electron impact ionization, photo-ionization offers a significantly higher efficiency and therefore it reduces the amount of evaporated atoms per loading. The main advantage is that the electron source does not need to be utilized, and the related changes of the stray electric fields due to patch charges after the loading process [85] can be avoided.

In the trap used for the experiments described here, changes of the stray field after loading an ion subside within days and become undetectable a few months after the loading process as shown in Fig. 2.3. The ion is typically stored for several months and in most cases lost accidentally during the stray field compensation, where the trapping potential is strongly reduced. The extremely long storage

times of single ions are related to the fact that we increase the residual gas pressure whenever no experiments involving laser cooling are performed and that the 370 nm laser light used for cooling should also be capable to photo dissociate YbH^+ [49].

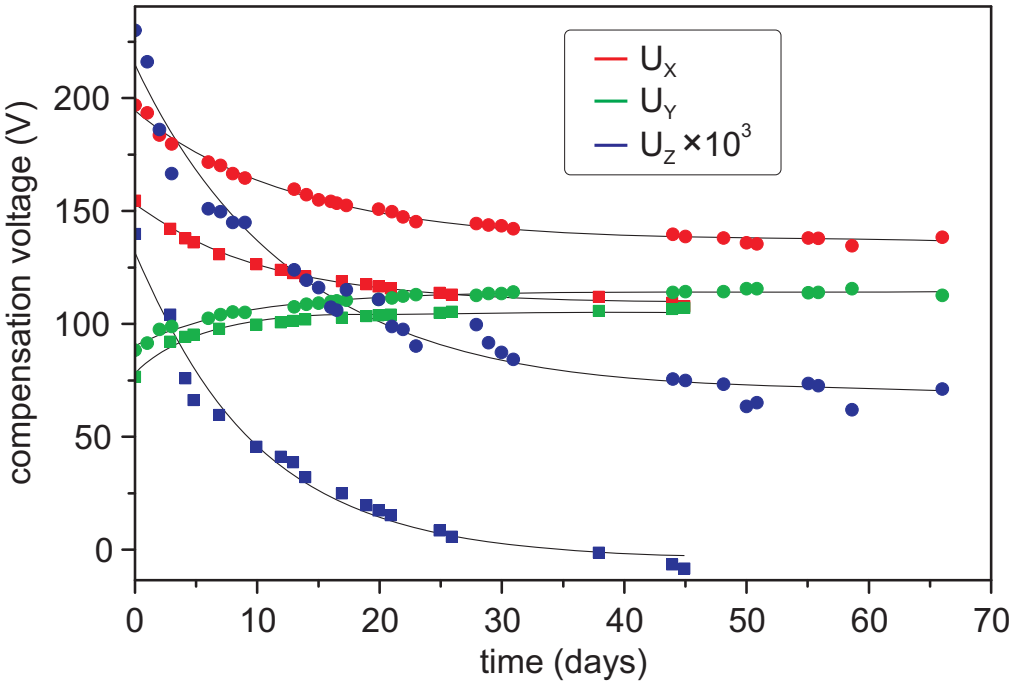

Figure 2.3: Temporal variation of the electric field compensating voltages after loading an ion to the trap. The different colors represent the three voltages (U_x, U_y, U_z). The circles show the data taken in a first measurement, squares data from a second period. The lines are fits to the data and yield a time constant between 6 and 13 days.

2.2 The Basic Interrogation Sequence

All experiments on the quadrupole and on the octupole transition were carried out by use of the so-called electron shelving technique, where the excitation to the metastable level is detected by absence of fluorescence while probing on the cooling transition [86]. The ion is Doppler cooled and subsequently interrogated on the forbidden transition. Successful excitation to the long-living state is indicated by absence of fluorescence at the beginning of the following cooling period. After state detection, the metastable level is depleted via excitation by light from a so-called repump laser to a short-living level, from which the ion decays back to the cooling cycle and the sequence is repeated. Figure 2.4 illustrates the basic experimental sequence for the spectroscopy of the quadrupole and octupole transition of $^{171}Yb^+$.

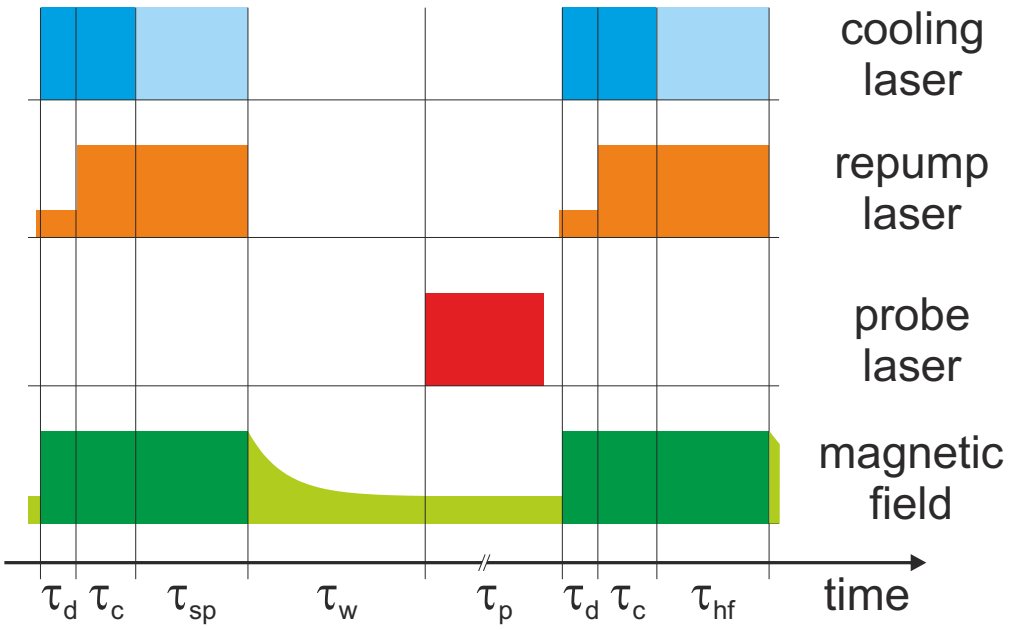

Figure 2.4: The basic experimental sequence for the spectroscopy of the clock transitions. During the state detection period τ_d and the Doppler cooling τ_c a microwave sideband of the cooling laser ensures efficient cooling. During τ_{sp} the sideband is switched off to prepare the ion in the F=0 hyperfine sublevel of the ground state. A waiting period τ_w ensures the decay of the large magnetic field to obtain a small and constant magnetic flux density during the probe period τ_p. The subsequent state detection, where the intensity of the repump lasers is strongly reduced, constitutes the beginning of the next cycle.

The interrogation with the cooling laser is separated in 3 parts: During the first 6 ms the state is detected by the electron shelving technique. During this and the subsequent part, a microwave sideband at 14.7 GHz depletes the $F = 0$ hyperfine component of the ground state and Doppler cooling is performed for 9 ms. By turning off the sideband and continuously driving the cooling transition as well as the 935 nm repump transition, the ion is trapped in the $F = 0$ ground state via branching from the excited state with high probability within 20 ms and resulting in a vanishing fluorescence signal. Successful preparation in the ground state is decided upon the voltage of the low-pass filtered output signal of the discriminator amplifier of the photomultiplier at the end of this period. The time constant of the low-pass filter is ≈2 ms. The strong magnetic field of ≈460 μT during the cooling period is switched off. A waiting time of 30 ms is required to ensure a sufficient decrease of the magnetic flux density has happened. During the interrogation a stable and weak magnetic field with a flux density of 3.58 μT is created with

an orthogonal set of coils and mechanical shutters block the cooling and repump light. The final state of the ion is detected at the beginning of the next cycle by counting the number of detected photons within 6 ms. In case of spectroscopy on the $^2S_{1/2}(F = 0) \rightarrow {}^2D_{3/2}(F = 2)$ quadrupole transition, the same laser that closes the cooling cycle by depleting the $^2D_{3/2}(F = 1)$ state, can serve as a repump laser via non-resonant excitation of the $^2D_{3/2}(F = 2) \rightarrow {}^3[3/2]_{1/2}(F = 1)$ transition if the light intensity is significantly increased. To avoid unwanted depletion of the $^2D_{3/2}(F = 2)$ state by the 935 nm laser light during the detection period, its intensity is strongly reduced by switching the drive power of an acousto-optic modulator, so that only the $^2D_{3/2}(F = 1)$ state is depleted. Methods to efficiently repump the ion from the long living $^2F_{7/2}$ state that is either populated by collisions or during spectroscopy on the octupole transition, will be discussed in the next section.

2.3 Repumping from the $^2F_{7/2}$ State

2.3.1 The $^2F_{7/2} \rightarrow {}^1[5/2]_{5/2}$ Repump Transition

The first experiments on driving the highly forbidden octupole transition at PTB with a diode laser system [65] indicated inefficient repumping by long dwell times of a few seconds in the long living $^2F_{7/2}$ state. At that time its two hyperfine sublevels were depopulated after excitation and state detection by light from one external-cavity diode laser system at 639 nm [87] as indicated in Fig. 2.5. The laser frequency was swept over two ≈200 MHz intervals separated by ≈3.6 GHz to permit excitation from all Zeeman sublevels for both hyperfine states. After successful excitation of the ion to the $^1[5/2]_{5/2}$ state, the ion decays to either the $^2D_{3/2}$ state and will be brought back to the cooling cycle by the 935 nm repump laser, or it decays to the $^2D_{5/2}$ state. In the latter case, the ion most likely returns back to the $^2F_{7/2}$ state or to the ground state. The branching ratio for the decay to the $^2F_{7/2}$ state has been measured to be 83(3)% and a lifetime of 7.2(3) ms has been determined for the $^2D_{5/2}$ state with $^{172}Yb^+$ [88]. The described cycling between metastable levels explains, why the ion remained dark for very long times. This effect is amplified if the ion was not returned within the first cooling period, since the switching of the strong magnetic field can result in the population of other Zeeman sublevels of the $^2F_{7/2}(F = 3, 4)$ states, from where excitation to the $^1[5/2]_{5/2}$ state is unlikely. The resulting dead times of the interrogation sequence prevented an efficient laser stabilization to the octupole transition.

In a first step, two sidebands with maximum relative intensity were created on the 639 nm light by a resonant electro-optic modulator at 1.81 GHz that corresponds to half of the hyperfine splitting of the $^2F_{7/2}$ state [89]. In this way, simultaneous excitation from both hyperfine sublevels to the $^1[5/2]_{5/2}$ state is achieved. An

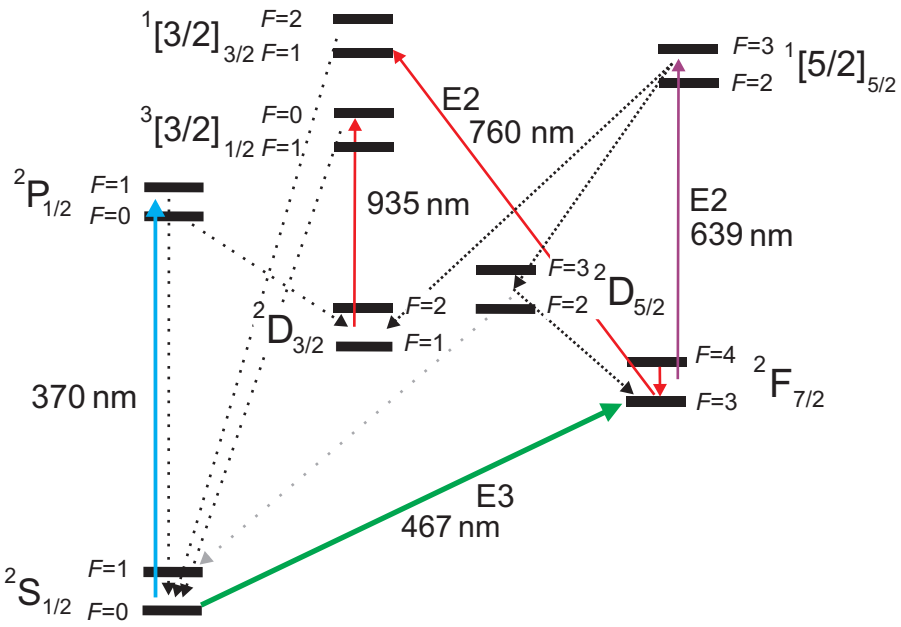

Figure 2.5: The partial level scheme of $^{171}Yb^+$ compares the two repump transitions from the $^2F_{7/2}$ state at 639 nm and 760 nm. Repumping of the $F = 4$ hyperfine sublevel to $F = 3$ is achieved via a magnetic dipole transition driven by a mircrowave field. The dotted lines indicate spontaneous decay channels.

additional frequency dither on the repump laser ensures excitation from different Zeeman components. This technique showed a clear improvement, however, in many cases the ion did not show fluorescence within the cooling cycle after state detection or even several cooling periods later.

To investigate the efficiency of the repump process, the frequency of the probe laser system was tuned to be resonant with the octupole transition, the pulse area was adjusted to excite the ion with a probability of ≈80% to the $^2F_{7/2}(F = 3)$ state and the fluorescence signal was continuously recorded. In this way, an effective lifetime of 250(25) ms was deduced for the $^2F_{7/2}$. Since the repump laser is only on during the cooling periods, this corresponds to 10 interrogation cycles.

In Ref. [88] a similar experiment was performed with $^{172}Yb^+$, which does not possess hyperfine structure. Here, the ion was simultaneously irradiated by the cooling laser light at 370 nm, the repump laser light at 935 nm and resonantly excited on the $^2S_{1/2} \rightarrow {}^2D_{5/2}$ transition at 411 nm. The $^2F_{7/2}$ state was populated by branching from the $^2D_{5/2}$ state and the rate and the duration of dark events in the detected fluorescence were compared for two different repump lasers, the one at 639 nm and another one that excites the $^2F_{7/2} \rightarrow {}^3[5/2]_{3/2}$ transition at 864 nm. The experiment clearly indicated superior efficiency for the 639 nm transition.

Since the transition at 411 nm was resonantly excited while the dark periods were measured, cycling between the metastable levels as described before might have been reduced by stimulated decay, but a comparable mean dwell time of 172 ms has been reported.

An intuitive way to understand the difference in the excitation probability on the two repump transitions can be found if the inner electronic configuration of $4f^{13}$ that does not change for the two transitions, is neglected, and only the outer part is taken into account. The two $6s^2$ valence electrons of the $^2F_{7/2}$ state can be seen as the helium-like ^1S ground state. Excitation to the $^1[5/2]_{5/2}$ state that has an outer electronic configuration of 5d6s(^{1}D) corresponds to a transition within the singlet configuration, whereas the excitation to the $^3[5/2]_{3/2}$ state with an outer electronic configuration of 5d6s(^{3}D) corresponds to a singlet-triplet transition and thus a lower excitation probability.

2.3.2 The $^2F_{7/2} \rightarrow {}^1[3/2]_{3/2}$ Repump Transition

It should be noted that due to the fact that the ground state and the $^2F_{7/2}$ state are connected via an electric octupole transition, repumping can not be achieved by dipole excitation and subsequent dipole decay but demands e.g. an electric quadrupole excitation and subsequent dipole decay. Together with the information described above, strict requirements for an efficient repump scheme can be concluded. The intermediate state should be a level that has a singlet like configuration, offers direct dipole decay to the ground state and can be excited via an electronic-quadrupole transition. Furthermore, it is convenient if the transition can be driven with a diode laser setup. All these requirements are fulfilled if the $^1[3/2]_{3/2}$ state with an outer electronic configuration of 5d6s(^{1}D) is chosen. In our experiment the required laser light intensity is provided by an external-cavity diode laser system at 760 nm and its frequency is long-term stabilized to the length of a 2 cm thick glass etalon. A fast frequency dither enables excitation from all Zeeman sublevels and a discriminator signal for stabilization purposes is generated by lock-in detection of light reflected from the etalon.

The first experiments with the new repumping scheme indicated a significantly improved repumping compared to the use of the 639 nm laser. 3 mW of laser radiation at 760 nm are focused to $\approx$50 μm at trap center and can be switched by an acousto-optic modulator and a mechanical shutter. With this laser, the resonant frequency of the $^2F_{7/2}(F = 3) \rightarrow {}^1[3/2]_{3/2}(F = 1)$ transition was determined to be 394.4250(3) THz and 394.4338(3) THz for the $^2F_{7/2}(F = 3) \rightarrow {}^1[3/2]_{3/2}(F = 2)$ transition. The uncertainty in the frequency measurements results from the accuracy of the employed wavemeter. The corresponding hyperfine splitting of 8.8(4) GHz of the $^1[3/2]_{3/2}$ state is significantly larger than that of other levels with the same electronic configuration at a similar energy.

Since the $F = 4$ hyperfine level of the $^2F_{7/2}$ state is only populated approximately once per hour by collisions, no fast repumping process is required to deplete the state. After detection of dark periods longer than 10 s that indicate population of the $F = 4$ state, microwave radiation at 3.6 GHz drives the hyperfine transition to the $F = 3$ state from where the ion is returned to the cooling cycle. In this way, no direct repumping from the $F = 4$ component with light from the 760 nm laser system is required. The polarization and frequency of the repump light, as well as the spatial overlap with the ion in the trap are optimized by minimizing the length of dark periods, when the octupole transition is driven with a high Rabi frequency. Under such conditions, the repump efficiency was tested and Fig. 2.6 shows a histogram of the duration of the dark period after the beginning of the cooling period. This clearly shows the significantly higher efficiency of the new repumping scheme. From the data shown in Fig. 2.6 a residual lifetime in the $^2F_{7/2}$ state of 1.6 ms can be inferred, since the lifetime of the $^1[3/2]_{3/2}$ state of 28.6 ns [90] is negligible.

2.4 Probe Laser System

The first laser system to excite the highly forbidden octupole transition at PTB is described in detail in Ref. [65]. This system was used to realize the first precise transition frequency measurement at PTB (see section 5.1) and to measure parts of the atomic parameters discussed in chapter 3. In this laser system the frequency of a commercially available laser diode at 934 nm was stabilized to the length of a 75 mm long reference cavity made of ultra low expansion glass using the Pound-Drever-Hall locking technique [16]. Phase modulation at 13.5 MHz for the discriminator signal was created with an electro-optical modulator (EOM) made of a high-resistivity potassium titanyl phosphate (KTP) crystal with facets cut under Brewster's angle. The use of KTP results in a low sensitivity to temperature fluctuations, so that an active temperature stabilization to avoid phase offset drifts is not required. The reference cavity was mounted horizontally inside a vacuum chamber surrounded by a massive copper cylinder, which provided a homogeneous temperature distribution. The temperature of this cylinder and the vacuum chamber were actively temperature stabilized by a two-stage servo system. The vacuum chamber, the mode matching optics, the EOM and an optical isolator were installed on a commercially available passive vibration isolation platform. A few 10 μW of laser radiation from the diode laser system were guided by a 5 m long single-mode polarization-maintaining fiber to the platform. To avoid instabilities due to the fiber, the polarization of the light was carefully aligned to the fiber using a quarter and a half waveplate. In a frequency ratio measurement together with the ultra-stable laser that is employed to drive the quadrupole transition [85], a

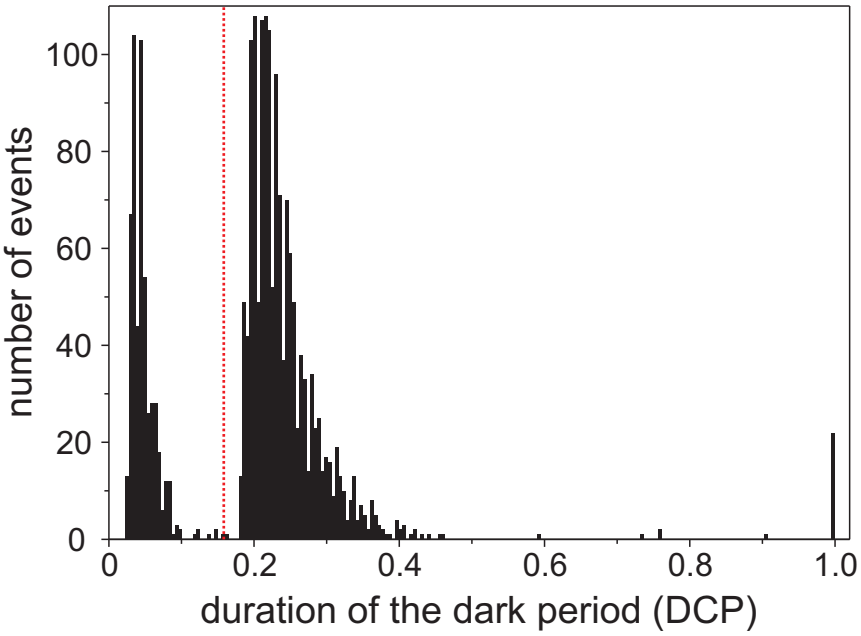

Figure 2.6: Histogram of the fluorescence off times after the beginning of the first cooling period subsequent to the probe pulse period. The time is measured in units of the duration of the cooling period (DCP) that is equal to 35 ms. The dotted red line indicates the time, when the repump laser at 760 nm is switched on. Therefore, for events with shorter duration, the $^2F_{7/2}$ state was not successfully populated. The number of events at 1 DCP is the summation of all events where the fluorescence did not return within one cooling period. If repumping was unsuccessful, stimulated decay during the subsequent probe period is avoided by not applying probe pulses until the fluorescence reoccurs.

fractional frequency instability of less than 2×10^{-15} at 1 s of averaging time has been observed, which is the combined instability of both lasers.

To achieve sufficient laser power for frequency doubling and exciting the highly forbidden octupole transition, the output light of the stabilized master laser was used to injection lock a 935 nm laser diode with a maximum output power of 300 mW. A small part of the slave laser output was brought to the frequency comb generator. The main part was coupled to an enhancement cavity for frequency doubling in a 6 mm long $KNbO_3$ crystal cut for angle-tuned phase matching at room temperature. The length of the cavity was stabilized by the Hänsch-Couillaud method [91] with a two stage servo system acting on piezoelectric transducers mounted under two mirrors of the enhancement cavity. The achieved bandwidth of the frequency lock of about 50 kHz sufficiently suppressed acoustic perturbations,

however, residual fast-frequency noise of the diode laser lead to relative fluctuations of the optical power of the frequency doubled light of about 10% for Fourier frequencies above 50 kHz. Under optimal conditions, 15 mW of 467 nm light were available and sent as a free beam to the second laser table on which the ion trap was installed. Using the old repump scheme, it was possible to excite the octupole transition by 90 ms long pulses and record spectra of the octupole transition with a maximum excitation probability of about 65% together with a minimum linewidth of 13 Hz as the full width at half maximum of a fitted Lorentzian profile, which corresponds to an essentially Fourier-limited resolution [65].

In a first step to improve the achievable resolution, an injection locked blue-emitting laser diode was installed close to the ion trap, so that fast intensity fluctuations are minimized. Significant path length fluctuations have been observed between the optical table on which the probe laser system was installed and the table on which the slave laser and the ion trap were mounted. To suppress such fluctuations, the free space link was replaced by a 5 m long single-mode polarization-maintaining optical fiber. Most of the optical path between the slave laser and the ion trap were enclosed with aluminum tubes to prevent air turbulence that can cause significant pointing fluctuations. Due to the high maximum output power of the slave laser of 20 mW, up to 12 mW were focused to a beam waist diameter of $\approx$40 μm at trap center. In combination with the new repump laser that prevents long dwell times in the $^2F_{7/2}$ state, the setup allowed us to observe the octupole transition with a Fourier-limited linewidth of 6.6 Hz by excitation with 120 ms long rectangular pulses as presented in Fig. 2.7. The necessary power to achieve a pulse area close to π was approximately 0.5 mW. The obtained quality factor of the atomic resonance of 9.7×10^{13} was limited by the frequency instability of the probe laser system, which was in turn limited by the thermal noise of the employed reference cavity [92].

It should be noted that the observed resonance was frequency shifted due to the light shift of the probe laser system by about 28 Hz. Due to the fact that this shift effect scales linearly with the intensity but the pulse area scales with the square-root of the intensity, longer probe pulse durations should reduce the shift effect significantly. The effect and techniques to cancel it by extrapolation are discussed in detail in subsection 3.2.3 and 3.2.4. Another advantage of extended interrogation times are improved quality factors of the resonance and hence an improved frequency instability of the optical frequency standard.

2.4.1 The new reference cavity

Different ideas to reduce the Brownian thermomechanical noise of the cavity mirrors and the spacer that limits the short-term frequency stability have been investigated. This includes an increase in the length of the cavity spacer, which results in a bigger beam diameter on the cavity mirrors [17, 93], the use of materials with

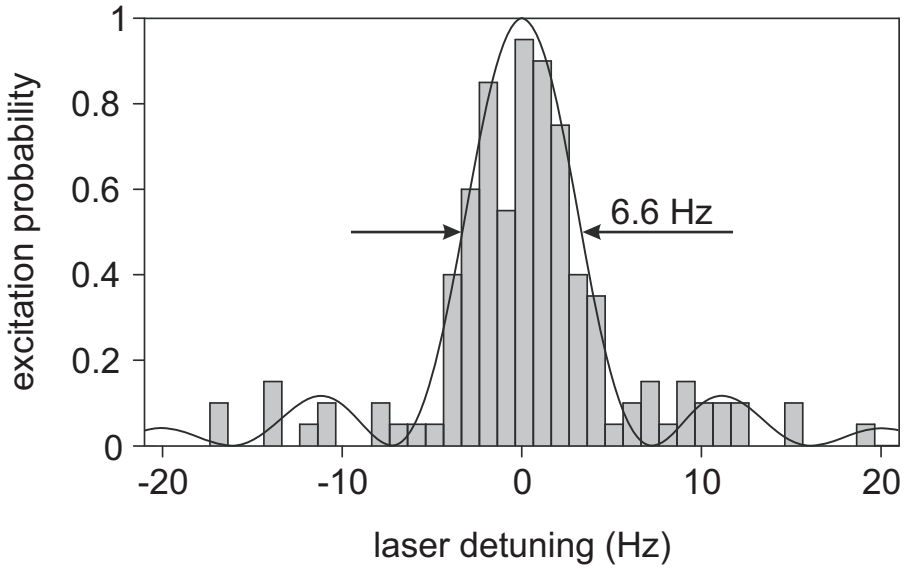

Figure 2.7: Excitation spectrum of the $^2\mathrm{S}_{1/2}(F=0) \rightarrow {}^2\mathrm{F}_{7/2}(F=3)$ transition obtained with a probe pulse duration of 120 ms. For each laser detuning step, 20 measurement cycles were performed. The solid line shows the theoretical line shape for a π-pulse excitation.

higher quality factor as mirror substrates [18, 94] and as cavity spacers [18, 95, 96]. Another way to reduce this effect is to operate at cryogenic temperatures, however, significant acoustic perturbations might be produced by the cooling system. Additionally, the experimental complexity increases significantly if cryogenic temperatures are required.

We use a 100 mm long cavity spacer made of Asahi AZ glass that offers a vanishing coefficient of thermal expansion (CTE) at about 22 °C in combination with optically contacted mirrors with fused silica substrate that should reduce the thermomechenical noise. The very different thermal expansion of fused silica and the Asahi AZ glass spacer results in a significant decrease of the zero crossing of the CTE. To compensate this effect, rings made of Corning's ultra-low expansion glass are optically contacted on the back of the mirrors [97]. With the help of a finite element simulation $T(CTE = 0) = 17$ °C for our combination has been predicted [98]. The cavity is mounted on 4 support rods, at positions that minimize acceleration sensitivity [98, 99]. 2 support rods are installed on flexure mounts to avoid an overdetermined system and thus improve the vibration insensitivity in the corresponding optical plane [100]. A photograph of the mounted reference cavity is presented in Fig. 2.8.

The fact that the reference cavity is operated at a temperature where the thermal expansion coefficient is close to zero reduces the requirements on the temperature control. The setup consists of an aluminum cylinder surrounding the cavity as a

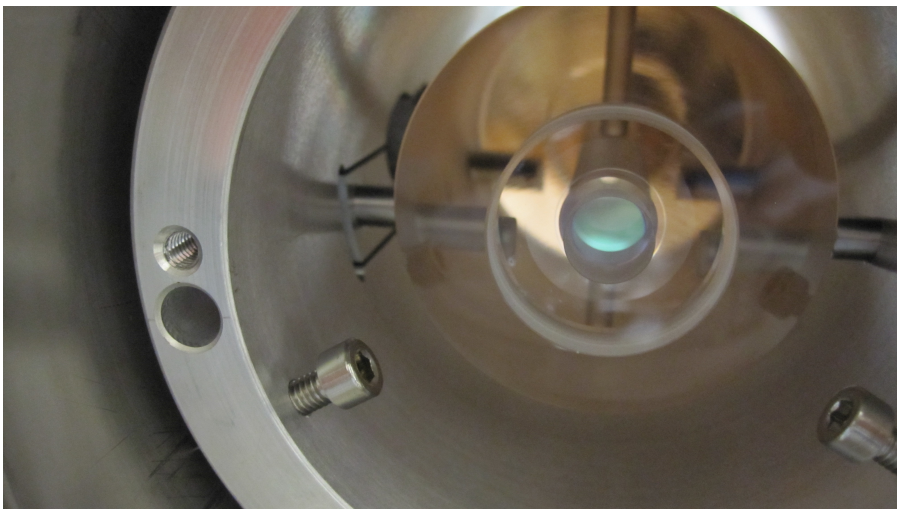

Figure 2.8: The new reference cavity of the octupole probe laser system installed on a mount that reduces its sensitivity against vibrations.

passive heat shield in the vacuum and an aluminum box that contains the vacuum chamber with the cavity. The temperature of the box is controlled with an integrating servo system via 4 Peltier elements installed between the mounts of the box and the optical breadboard of the vibration isolation platform. To improve temperature isolation of the box from the environment, it is enclosed by few centimeter thick extruded polystyrene foam. In this way, an averaged electric power of only 50 mW is necessary to operate the chamber around 17 °C. A change of the reference value of the temperature controller leads to a change of the frequency of the probe laser that is stabilized to the length of the cavity with a time constant of 13 h.

For the first tests of the new reference cavity, a few 100 μW of the laser light from the old 934 nm probe laser system [65] were frequency shifted to match with one of the fundamental cavity resonances. Similar to the first setup, a discriminator signal is created with the Pound-Drever-Hall technique [16] and used to servo the frequency offset with an accousto-optic modulator. The high frequency stability of the probe laser facilitates optimizing mode matching of the laser beam to the high-finesse cavity. A coupling efficiency of 81% has been measured, the finesse was determined to be 500,000 and about 30% of the light in front of the cavity is transmitted on resonance.

To determine the thermal expansion of the cavity as a function of its temperature, the temperature of the aluminum box was adjusted and the frequency of the light stabilized to one TEM_{00} resonance was measured against a H-maser at our frequency comb generator. From the thermally induced frequency variation, the corresponding length variation ΔL was inferred. The result of this measurement is

shown in Fig. 2.9. All values are corrected for the linear creep of the cavity length. The observed dependence clearly follows the expected quadratic dependence with a sensitivity of 1.0×10^{-9} K^2. From the results obtained while increasing the temperature, a minimum at 16.96 °C was determined. Although the frequency and the temperature can be measured with high precision, an uncertainty of 0.08 K is expected from imperfection of the isothermal creep correction and a residual variation temperature, since no temperature sensor is installed close to the cavity. Thus a sufficient long waiting time was required to ensure that the cavity was in thermal equilibrium with the housing. After adjusting the temperature controller to the minimum of the quadratic fit to the obtained data, the frequency of the probe laser was found to be slightly larger than expected. This might be related with the fact that the minimum was reached by reducing temperature, whereas T(CTE=0) has been determined while increasing. Repeated measurements gave the same $T(CTE = 0)$, but also a small frequency difference at the minimum temperature depending on the process that was used to reach the point, which might be understood as a small hysteresis effect of the material.

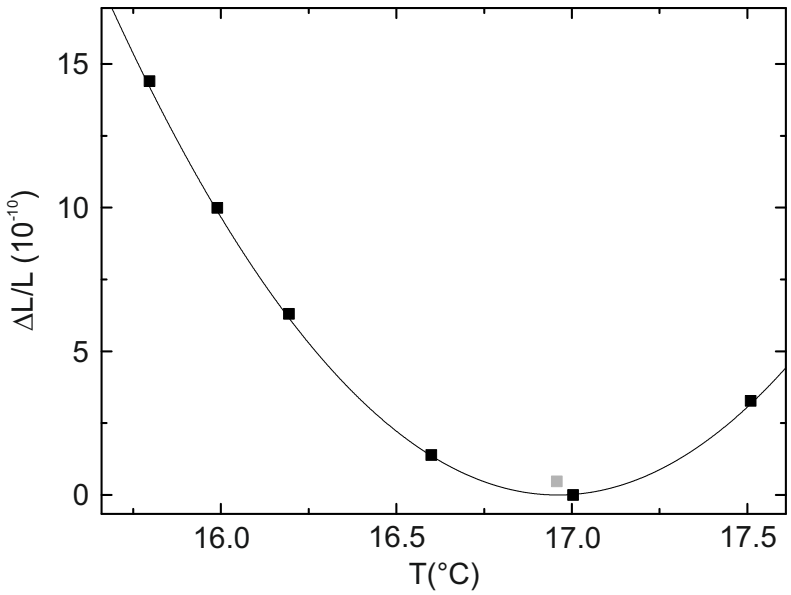

Figure 2.9: Relative length of the new reference cavity as a function of its temperature. The values are inferred from frequency measurements of the laser system that uses the cavity as the reference. All values are corrected for a linear drift of the cavity length. The black symbols represent data obtained while increasing the temperature and the solid line is a quadratic fit. The gray square was measured after recooling the cavity to the temperature at the center of the fit.

Another effect that can induce significant fluctuations of the probe laser frequency results from a variation of the amount of light that circulates in the cavity and heats the mirrors. A sensitivity of 50 Hz/μW of the probe laser frequency on the light power sent to the cavity has been found. After stepping up the optical power, the frequency changes within a few seconds, long term variation due to heat transfer to the mirror substrate and the cavity spacer do not lead to significant frequency changes, because of the minimized sensitivity against temperature variations. To avoid possible frequency instability due to power variations, we use only 10 μW of optical power and actively stabilize the amount of light in the cavity. Therefore we servo the power of the AOM before the cavity to obtain a constant signal from a photodetector that monitors the transmitted light. The bandwidth of this loop system is $\approx$1 kHz, limited by the low-pass characteristic of the optical cavity.

To test the sensitivity of the reference cavity to vibrations, the cavity setup on the passive vibration isolation platform was set into oscillations with an amplitude of $\approx$0.5 cm and a frequency close to the mechanical resonance of the system of $\approx$0.5 Hz. The acceleration was measured with a micro-electro-mechanical system based accelerometer whose output signal was low-pass filtered to optimize the measurement contrast. The simultaneous output for 3 different axis of motion is used to verify that an individual axis of motion is driven. The induced frequency shift was measured against the stable probe laser system that excites the quadrupole transition using the fiber-laser based frequency comb generator. From the measurement depicted in Fig. 2.10, the fractional frequency sensitivity against accelerations were determined to be $3.6(4) \times 10^{-12}\mathrm{m}^{-1}\mathrm{s}^2$ perpendicular to the optical path, $5.9(5) \times 10^{-12}\mathrm{m}^{-1}\mathrm{s}^2$ along the optical path and $11.1(6) \times 10^{-12}\mathrm{m}^{-1}\mathrm{s}^2$ if the cavity is accelerated vertically. The uncertainty in the measurements results from the limited resolution of the acceleration sensor and the residual acceleration in other directions. The measured sensitivities are comparable to the results obtained in Ref. [99] based on a similar design. Due to the low sensitivity in combination with the low level of seismic noise in our laboratory and the suppression by the vibration isolation platform [101], no related limitations of the short-term frequency instability are expected.

In order to determine the short-term frequency instability of the new probe laser system its frequency needs to be compared to other frequency references. For short averaging intervals an infrared laser at 1.5 μm stabilized to a silicon single-crystal optical cavity can serve as a reference. The thermal noise of the silicon cavity leads to an estimated flicker floor of the fractional frequency instability of $\sigma_y = 7 \times 10^{-17}$ [18]. In a comparison with other lasers, a fractional short-term stability at 1 s of better than 2×10^{-16} has been demonstrated [18]. In a comparison with the fiber-laser based frequency comb generator located in our building, the instability of the laser referencing the silicon cavity is expected to be increased due to residual noise from the 200 m fiber link between the buildings and the

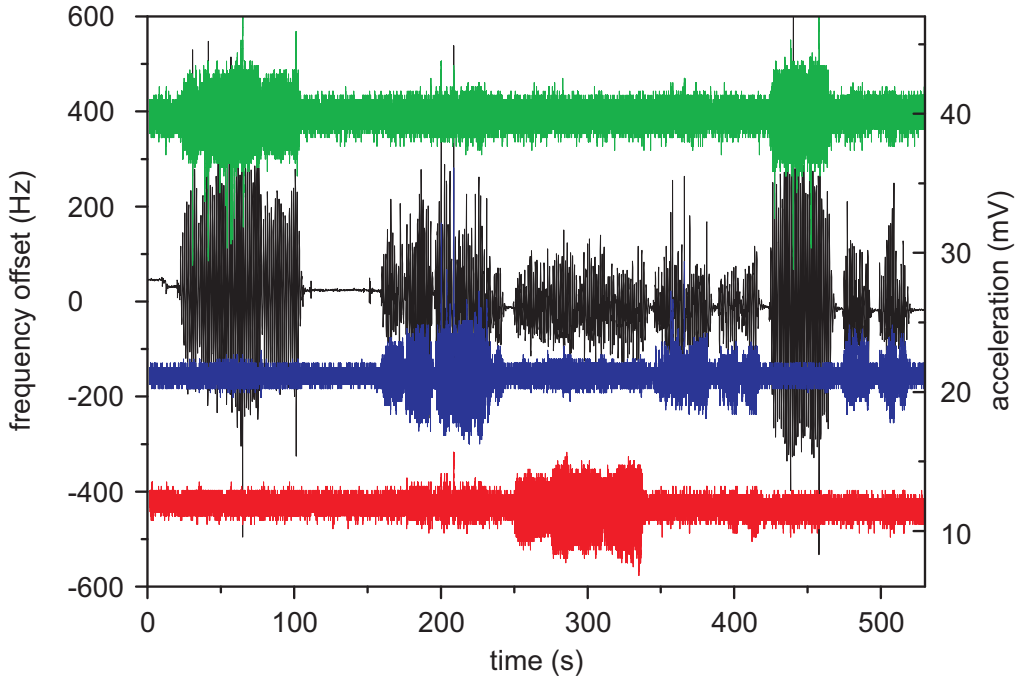

Figure 2.10: Measured frequency offset (black line) of the probe laser system versus the probe laser for the quadrupole transition resulting from accelerations of the reference cavity. The cavity is accelerated on the vibration insensitive platform along the optical path (blue line) and perpendicular to this direction (red line) as well as vertically (green line). The acceleration was measured with a micro-electro-mechanical system based accelerometer with a sensitivity of about 40 mV $m^{-1}s^2$.

length fluctuations of short pieces of unstabilized fibers in the comb setup. In Fig. 2.11 the observed fractional instability of the frequency ratio of the new probe laser system and the laser stabilized to the silicon cavity is shown. A significant improvement over the fractional frequency instability of the old probe laser setup of about 2×10^{-15} at 1 s [65] resulting from the use of fused-silica mirrors and the longer spacer is observed. The thermomechanical noise floor of the new reference cavity has been calculated according to Ref. [92] to be 4.1×10^{-16}. The measured combined fractional frequency instability of 5×10^{-16} shows that the achieved stability of the new probe laser is very close to its fundamental limit.

Due to the improved short-term stability of the probe laser system, significantly longer coherent interrogations are possible. Figure 2.12 shows a spectrum of the octupole transition with a Fourier-limited linewidth of 2.4 Hz obtained by excitation with 335 ms long rectangular probe pulses. The necessary power to achieve a pulse area close to π was approximately 60 μW. The obtained quality factor of the

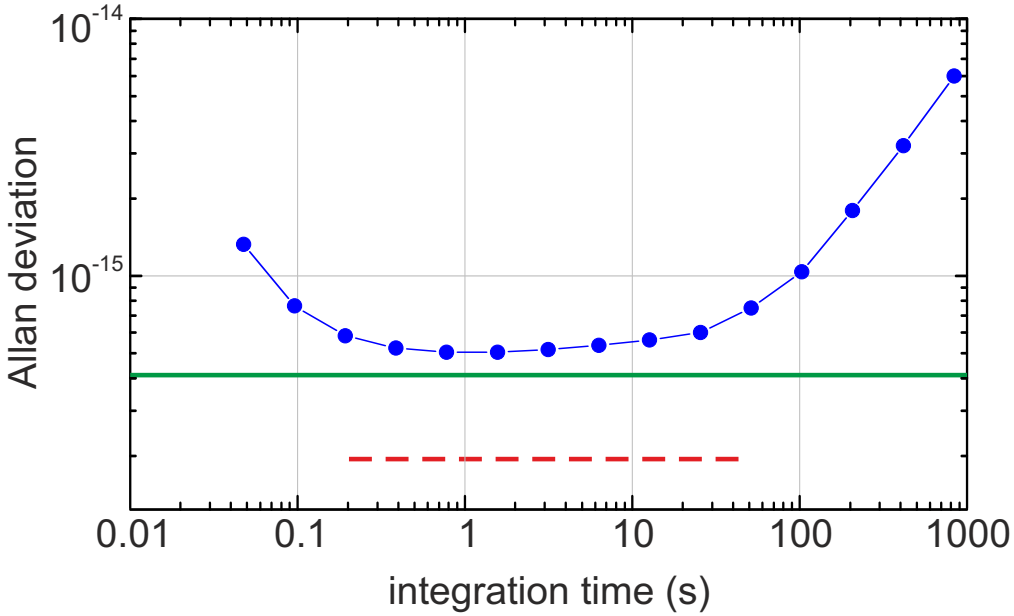

Figure 2.11: The blue dots show the relative Allan deviation of the frequency ratio of the octupole probe laser system referencing the new cavity and a fiber laser at 1.5 μm locked to a silicon single-crystal cavity [18]. The line connecting the points is a guide to the eye. The green line shows the calculated thermal noise limit of the new cavity and the red dashed line indicates the expected frequency instability of the 1.5 μm laser at the frequency comb generator in our laboratory (see text).

atomic resonance is 2.7×10^{14}. The center of the resonance is shifted by ≈4 Hz from the unperturbed transition frequency due to the light shift.

To investigate the frequency instability for longer averaging intervals, the frequency of the stabilized laser is measured using the frequency comb generator versus an H-maser. The H-maser has a very small long-term frequency drift and is therefore an appropriate reference. In this way, the frequency drift of the new probe laser system was measured for ≈10 h and the result is presented in Fig. 2.13. The data was recorded in April 2011 and a predominately linear drift of the probe laser frequency with a rate of 46 mHz/s has been observed. The non-linear residuals are smaller than 4 mHz/s on a timescale of several hundreds of seconds resulting from changes of the drift rate of less than 5×10^{-6} Hz/s^2. The magnitude of the linear drift rate has constantly decreased, and reached a value of 22 mHz/s in Dec 2013. Residual variations are most likely related with a residual temperature sensitivity of the system, but should not degrade the systematic uncertainty of the optical frequency standard.

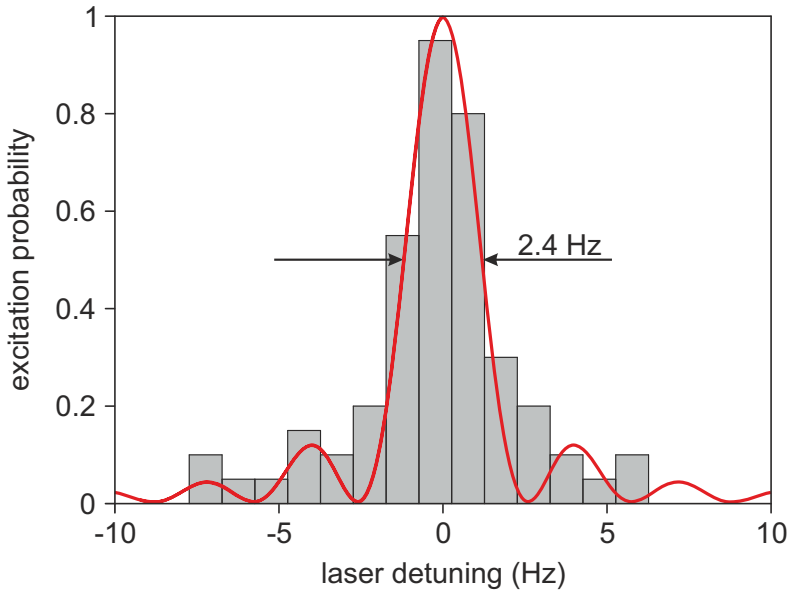

Figure 2.12: Excitation spectrum of the $^2S_{1/2}(F=0) \rightarrow {}^2F_{7/2}(F=3)$ transition obtained with a probe pulse duration of 335 ms. For each laser detuning step, 20 measurement cycles were performed. The solid line shows the theoretical line shape for a π-pulse excitation.

2.5 Laser Stabilization to forbidden transitions

In an optical frequency standard, the frequency of a probe laser with a sufficiently low short-term instability is stabilized to a narrow optical transition. The most widely used way to generate the required discriminator signal is to probe the atomic transition with alternating frequency detunings ($\nu_L \pm \delta_m$) that correspond to half of the resonance width. With this information, the central frequency is steered to equalize the excitation probability in the two cases. This is also the basic idea of the algorithm used in the digital servo system realized in our experiment and described in detail in Refs. [85, 102]. The closed-loop control corrects the frequency of the probe laser system ν_L by changing the frequency of the RF signal of the AOM in front of the high-finesse cavity. After $2z$ valid interrogations of the ion, a frequency correction f_c is calculated from the number of successful excitations with negative n_- and positive n_+ frequency detuning δ_m as

$$f_c = g \cdot \delta_m \frac{n_+ - n_-}{z}. \tag{2.12}$$

The coefficient g defines the gain of the loop system and has been set close to 0.1. Since a two level system realized with a single ion provides the frequency reference, the probe laser has a sufficiently short-term stability and the interrogation time mainly determines the cycle time, the so-called quantum-projection noise [15] is

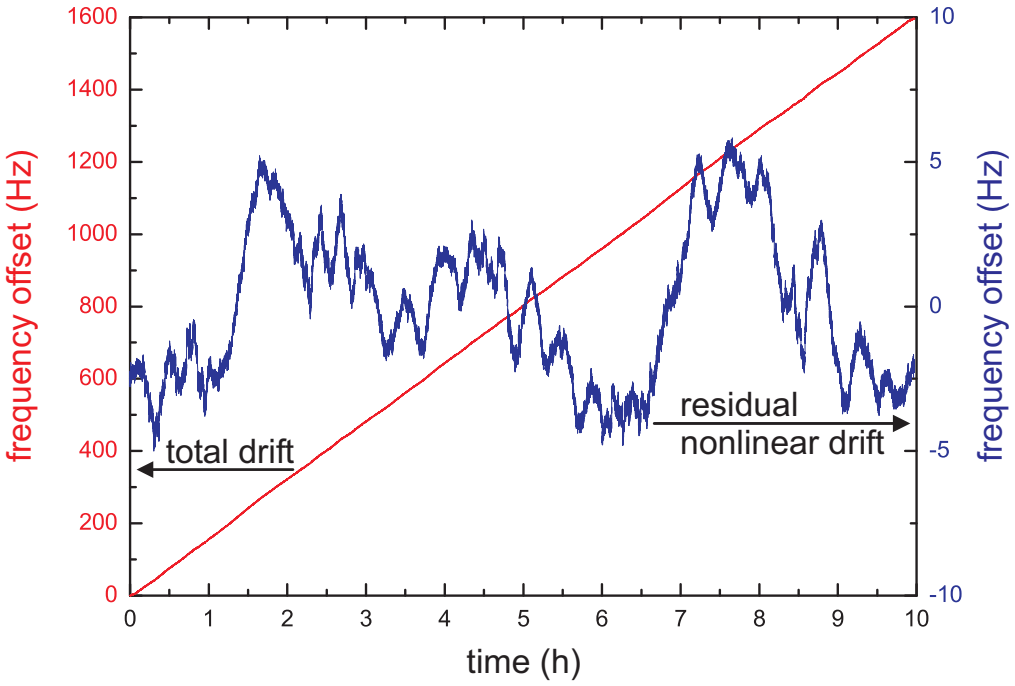

Figure 2.13: The red line shows the frequency of the probe laser system stabilized to the new reference cavity as a function of time. A linear fit yields a drift rate of 46 mHz/s and the residual nonlinear drift causes variations smaller than ±5 Hz over 10 h related with changes of the drift rate of less than 5×10^{-6} Hz s^{-2}. The measurement was performed in April 2011, a few months after mounting the cavity in its vacuum chamber.

the dominant contribution to the instability of the frequency standard for long averaging times. Short detection, cooling and state preparation periods result in small dead times and by that ensure a negligible instability contribution due to the so-called Dick effect [103]. An important feature of the laser frequency loop system used in our experiment is the fact that it realizes a second-order integrating servo i.e. an additional digital loop system generates an error signal similar to Eq. 2.12 on a timescale of 10 s and steers a frequency drift correction that cancels the dominantly linear frequency drift caused by the relaxation of the optical reference cavity. In this way, a significant frequency offset between the atomic resonance and the constantly drifting probe laser frequency is avoided. A residual servo error is expected only from the limited gain of the loop system to compensate frequency drift rate changes of the probe laser system [28]. The corresponding uncertainty is presently only a minor contribution to the total systematic uncertainty of the quadrupole and octupole optical frequency standard.

Since the loop-system that steers the frequency of the probe laser system is realized in a fully digital fashion with computer control, it is possible to modify the servo system, so that not only one control-loop stabilizes the laser frequency to the atomic resonance, but two independent servo systems act alternately. In combination with switching between two sets of parameters, the related frequency difference can be measured without an external reference. The statistical uncertainty of such a measurement results only from quantum projection noise and a reduced systematic uncertainty of the measurement can be obtained, because most interfering frequency shift effects appear equally for both configurations. To ensure an efficient common mode rejection, the active servo system and the respective set of parameters are alternated after 4 interrogations [85]. In this way it is possible to measure small systematic frequency shifts as described in chapter 3. This technique is also an essential element of the light shift cancellation technique described in subsection 3.2.4 and the controlled "hyper-Ramsey" scheme of section 4.3. To ensure that the instability of the probe laser system is not degraded by switching it's frequency to the value of the active state, the probe laser frequency, as measured at the frequency comb, is adjusted only for one of the states. The frequency offset that appears in the other mode, is balanced by controlling the frequency of the acousto-optic modulator that is used to create the probe laser pulses.

3 Frequency Shift Effects of the Yb^+ Clock Transitions

In this chapter shift effects of the $^2S_{1/2}(F = 0) \rightarrow {}^2D_{3/2}(F = 2)$ and the $^2S_{1/2}(F = 0) \rightarrow {}^2F_{7/2}(F = 3)$ transition of $^{171}Yb^+$ due to external fields will be discussed. Additionally this chapter treats effects that introduce offsets of the observed transition frequency without affecting the atomic structure.

Most of the shift effects discussed in this chapter have been experimentally investigated with an alternating servo system that has been introduced in section 2.5. The first section of this chapter will discuss the Doppler shift, resulting from residual motion of the trapped ion and the next section deals with the quadratic Stark effect and its appearance in very different frequency regimes. Afterwards, shift effects due to the interaction of the quadrupole moment of the excited states with electric field gradients are investigated. Zeeman shifts resulting from the interaction with magnetic fields and shifts due to collisions with background gas molecules are subsequently addressed, before shifts of the observed transition frequency are investigated, that are not resulting from shifts of the atomic levels, but are induced by imperfections of the measurement process. Finally, uncertainty budgets of the optical frequency standards based on the quadrupole and the octupole transition are compared.

3.1 Doppler Shift

The motion of the ion in the trap relative to the laboratory frame causes a difference between the observed probe laser frequency in the rest frame of the ion $\nu\prime$ and in the laboratory frame ν:

$$\frac{\nu\prime}{\nu} = \gamma\left(1 - \frac{v_\parallel}{c}\right), \quad \gamma = \frac{1}{\sqrt{1 - v^2/c^2}}. \tag{3.1}$$

Here c denotes the speed of light, v the absolute value of the ion's velocity with respect to the laboratory frame and $v_\parallel$ is the speed along the wave vector of the probe laser beam. During the operation as a frequency standard, a digital servo system ensures that the probe laser frequency in the rest frame of the ion $\nu\prime$ equals

the atomic transition frequency ν_0, so that a shifted frequency is observed in the laboratory frame. The so-called Doppler shift can be written as

$$\begin{aligned}\frac{\delta\nu}{\nu_0} = \frac{\nu-\nu_0}{\nu_0} &= \left(\gamma\left(1-\frac{v_\parallel}{c}\right)\right)^{-1} - 1 \\ &= \frac{\langle v_\parallel\rangle}{c} - \frac{\langle v^2\rangle}{2c^2} + \frac{\langle v_\parallel\rangle^2}{2c^2} + \mathcal{O}\left(\frac{v^3}{c^3}\right). \end{aligned} \tag{3.2}$$

The angle-brackets denote the time average over the duration of the probe pulse, that is usually several 10 ms long. The first term describes the first-order Doppler shift. The time average of the fast oscillating micromotion and secular motion, that results in observable sidebands of the spectrum and mainly determines $v_\parallel$ does not lead to a net first-order Doppler shift ($\langle v_\parallel\rangle/c$). Here, only changes of the ion's mean position along the wave vector during the entire measurement process or such changes of the position of the ion, that appear simultaneously with each interrogation, are important. These shifts are in detail discussed in sections 3.6 and 3.8 of this chapter. The second term of (3.2) is a consequence of Einstein's special relativity theory [104], and is called the second-order Doppler shift or transversal Doppler effect, since it is also observable for velocities perpendicular to the wave vector. In 1938 Ives and Stilwell were able to verify an additional quadratic shift as the mean shift of the frequencies of radiation from moving hydrogen atoms observed at 0° and 180° relative to their velocity [105]. Using Mößbauer spectroscopy the shift effect was measured for rotating systems [106, 107], but the first direct observation of the frequency shift perpendicular to the direction of motion was achieved in 1979 by Hasselkamp *et al.* [108].

The secular motion and the micromotion are both contributing to the second-order Doppler shift, but show different dependence due to their individual character of motion. As discussed in chapter 2, the secular motion is thermal motion that results from the temperature of the ion in the trap potential and can be assumed to be equal in all three directions, see Eq. 2.11, whereas the micromotion is driven motion that results from acceleration through the radio frequency trap field. According to Ref. [69], the second-order Doppler shift due to secular motion is

$$\frac{\delta\nu_{SM}}{\nu_0} = -3\frac{k_B T_D}{2mc^2}. \tag{3.3}$$

Similar to the time averaged square of the electric radio-frequency field described in Eq. 2.11, the second-order Doppler shift due to micromotion consists of two parts and is equal to [69]

$$\frac{\delta\nu_{MM}}{\nu_0} \approx -\frac{1}{mc^2}\sum_{i=x,y,z}\frac{k_B T_i(a_i+q_i^2)}{2(2a_i+q_i^2)} + \frac{4}{m}\left(\frac{Qq_iE_{DC,i}}{(2a_i+q_i^2)\Omega}\right)^2. \tag{3.4}$$

The first part results from non-vanishing amplitude of the secular motion after Doppler cooling. It is equal to the shift induced by the secular motion under normal operation conditions, as expected from a conservation of energy argument [109]. The second part of Eq. 3.4 is a consequence of the excess micromotion that occurs if the ion is displaced from the minimum of the trap potential e.g. by uncompensated stray electric fields. As discussed above, for the z-axis a remaining field of less than 2.4 V/m is expected, which would cause a maximum fractional frequency shift of -1.7×10^{-19}.

Combing the two contributions of thermally induced second-order Doppler shift with that due to uncompensated stray fields for all three directions, one finds $-2.8(1.7) \times 10^{-18}$ for spectroscopy of the quadrupole transition and $-3.7(2.1) \times 10^{-18}$ for operation of the octupole frequency standard with an interrogation time of 250 ms. The uncertainty results from the uncertainty of the ion temperature, that is assumed to be 50%, and from the total possible shift due to uncompensated stray electric fields.

It should be noted that a significant additional micromotion and thus an increased second-order Doppler shift can be induced by a phase difference of non-vanishing RF voltages on the two end caps of the trap in our experiment. Unfortunately, the trap geometry does not allow for optical access from three mutually orthogonal directions, which would be required to measure motion of the ion in all directions, however, for the accessible direction the observed micromotion correspond to the level expected from the observed secular motion i.e. the residual temperature of the ion in the trap.

3.2 Quadratic Stark Shift

The quadratic Stark shift is a very basic phenomenon that results from the interaction of external electric fields with the induced dipole moment of the atom. This shift effect appears with different names for the very different frequency ranges of the disturbing electric field, but is based on the same effect: the shift can be induced by quasi-constant electric fields or appear as light shift, which is the Stark shift induced by the electric field of the light. This section starts with a short introduction to the theory of the Stark shift and continues with a calculation of polarizabilities and a comparison to experimental results. Afterwards, the dominant frequency shift effect in the case of single-pulse excitation of the octupole transition, the dynamic Stark shift induced by the probe laser light, is described. This is followed by the related blackbody radiation shift, which is the dynamic Stark shift induced by the thermal radiation. Connected with this, the differential electric polarizability of the octupole transition is measured, and at the end of this section the frequency shifts due to the thermal radiation and residual interaction with the trap field are calculated.

3.2.1 Calculation of the Differential Polarizability

The theory of the quadratic Stark shift in free atoms has been described in detail by Angel and Sander in Ref. [110], a short introduction to the calculation can be found in [111, 112]. The Stark Hamiltonian

$$H_S = -\boldsymbol{p} \cdot \mathbf{E} \tag{3.5}$$

where $\boldsymbol{p}$ is the electric dipole moment operator and $\mathbf{E}$ the electric field, is usually only a very small contribution to the complete Hamiltonian of the atom, suggesting a perturbative treatment. According to Ref. [110] the quadratic Stark shift using second-order perturbation theory in the (IJ) coupling scheme of a state $|\gamma J F m_F\rangle$ is calculated to be

$$\Delta W_Q S(\gamma, J, F, m_F, \boldsymbol{E}) = -\left(2\alpha_S(\gamma, J) + g(F, m_F, \beta)\alpha_T(\gamma, J, F)\right) \frac{|\mathbf{E}|^2}{4} \tag{3.6}$$

$$g(F, m_F, \beta) = \frac{3m_F^2 - F(F+1)}{F(2F-1)}(3\cos^2\beta - 1). \tag{3.7}$$

The shift scales with the square of the absolute value of the electric field $\mathbf{E}$ and with two parameters, the scalar α_S and the tensor polarizability α_T. The latter results in an angular dependence of the shift on the angle β between the electric field vector and the quantization axis defined by the orientation of the magnetic field that induces the splitting of magnetic sublevels. The dependence of the tensor polarizability $\alpha_T(\gamma, J, F)$ on the hyperfine quantum number F and the nuclear spin I is:

$$\begin{aligned}\alpha_T(\gamma, J, F) &= (-1)^{I+J+F} \left[\frac{F(2F-1)(2F+1)(2J+3)(2J+1)(J+1)}{(2F+3)(F+1)J(2J-1)}\right]^{1/2} \\ &\quad \times \left\{ \begin{array}{ccc} J & F & I \\ J & F & 2 \end{array} \right\} \alpha_T(\gamma, J).\end{aligned} \tag{3.8}$$

The brackets denote the 6J symbol, that is defined as a sum over products of four 3J symbols, which in turn are related with Clebsch-Gordon coefficients. Both parts of the polarizability can be calculated from oscillator strengths $f_{\gamma,J,\gamma',J'}$ and the energy difference of the two related states $(W(\gamma', J') - W(\gamma, J))$ [112].

$$\alpha_S(\gamma, J) = \frac{4\pi\epsilon_0 e^2\hbar^2}{m_e} \sum_{\gamma,' J' \neq \gamma, J} \frac{f_{\gamma,J,\gamma',J'}}{(W(\gamma', J') - W(\gamma, J))^2}, \tag{3.9}$$

$$\begin{aligned}\alpha_T(\gamma, J) &= \frac{4\pi\epsilon_0 e^2\hbar^2}{m_e} \left[\frac{30J(2J-1)(2J+1)}{(2J+3)(J+1)}\right]^{1/2} \\ &\quad \times \sum_{\gamma,' J' \neq \gamma, J} (-1)^{J-J'} \left\{ \begin{array}{ccc} 1 & 1 & 2 \\ J & J & J' \end{array} \right\} \frac{f_{\gamma,J,\gamma',J'}}{(W(\gamma', J') - W(\gamma, J))^2},\end{aligned} \tag{3.10}$$

where ϵ_0 denotes the vacuum permittivity, e is the elementary charge, m_e labels the mass of an electron and $\hbar$ is the reduced Planck constant.

The necessary set of oscillator strengths was for instance calculated in Ref. [60] for the Yb^+ ion. The resulting polarizabilities for the relevant energy levels are presented in table 3.1. The frequency shift of the reference transitions results from the differential shift $\Delta W = \Delta W_e - \Delta W_g$ related with the polarizabilities of the excited state α_e and the ground state α_g. It is straight forward to use the differential polarizability $\Delta\alpha = \alpha_e - \alpha_g$ for shifts of the reference transitions. Using the values for the individual polarizability, the differential static scalar polarizability for the quadrupole transition is $5.29 \times 10^{-40}\mathrm{Jm^2V^{-2}}$ and for the octupole transition $1.86 \times 10^{-40}\mathrm{Jm^2V^{-2}}$.

Table 3.1: Calculated static scalar α_S and tensor α_T electric polarizabilities for the states relevant for the two clock transitions of $^{171}Yb^+$. All values are given in $10^{-40}\mathrm{Jm^2V^{-2}}$.

	f values from [60]	corrected f values [112]
$\alpha_S(^2\mathrm{S}_{1/2})$	8.9	9.6
$\alpha_S(^2\mathrm{D}_{3/2})$	14.2	15.2
$\alpha_T(^2\mathrm{D}_{3/2}, F=2)$	-11.5	-12.2
$\alpha_S(^2\mathrm{F}_{7/2})$	10.8	10.8
$\alpha_T(^2\mathrm{F}_{7/2}, F=3)$	-0.15	-0.02

As proposed in Ref. [112] by S. Lea, the theoretical oscillator strengths f_c from Ref. [60] can be corrected using the ratio of experimentally determined lifetimes τ_e and those resulting from the calculation τ_c according to $f_i = f_c(\tau_c/\tau_e)$. The calculated static polarizabilities based on the corrected oscillator strengths are presented in table 3.1. In most of the cases relevant for the calculation of $\alpha_S(^2\mathrm{F}_{7/2})$, f_i agrees well with f_c. For the $^2\mathrm{S}_{1/2}$ and $^2\mathrm{D}_{3/2}$ state, however, the theoretical lifetimes of the two most important states ($^2\mathrm{P}_{3/2}$ and $^2\mathrm{P}_{1/2}$) in the calculation of the static scalar polarizability of the $^2\mathrm{S}_{1/2}$ state are about 10% larger than the experimental value. This might be related with the fact, that in the latter case, transitions between states with a filled 4f shell and the opened $4f^{13}$ shell are important. The scalar polarizability of the $^2\mathrm{F}_{7/2}$ state appears largely unaffected by using oscillator strengths based on lifetime corrections, whereas the polarizability of the $^2\mathrm{S}_{1/2}$ and $^2\mathrm{D}_{3/2}$ states increases by $\approx$7%. Since the two values contribute equally to the differential polarizability of the quadrupole transition, its value remains constant, whereas a significant change is observable for the octupole transition.

The remarkable resemblance of the polarizabilities of the upper and lower state of the octupole transition is surprising: by neglecting the $4f$ shell a significant

difference in the polarizabilities of the $^2\mathrm{F}_{7/2} : 6s^2$ and the $^2\mathrm{S}_{1/2} : 6s$ state would be expected, so that an important effect has to result from the $4f$ electrons. Therefore, a significantly improved theoretical description of the differential polarizability requires a treatment of all 15 valence electrons with high accuracy. Possible improvements might be expected from calculations similar to those performed for isoelectric elements in Ref. [113].

3.2.2 Measurement of the Static Electric Polarizability

As discussed above, the calculated polarizabilities have significant uncertainties resulting from limitations in the calculation of the oscillator strength between states within the complex electronic structure of Yb^+. Since the theoretical description can not provide the necessary accuracy, an experimental investigation of the differential polarizability is required. In Ref. [70] a measurement of $\Delta\alpha_s^{\mathrm{dc}}$ of the quadrupole transition was performed by recording the induced frequency shift while changing the mean position of the ion from the center of the trap field along the trap axis. If the field is well characterized, the induced second-order Doppler shift can be calculated and removed. The remaining frequency offset results from the quadratic Stark shift induced by the quasi-static electric field. By measuring the frequency shift for two different orientations of the magnetic field, that defines the quantization axis, the static differential polarizabilities of the $^2S_{1/2}(F = 0) -^2 D_{3/2}(F = 2, m_F = 0)$ transition were experimentally determined to be $\Delta\alpha_s^{\mathrm{dc}} = 6.9(1.4) \times 10^{-40}\ \mathrm{Jm^2V^{-2}}$ and $\alpha_T^{\mathrm{dc}} = 13.6(2.2) \times 10^{-40}\ \mathrm{Jm^2V^{-2}}$.

In the case of Rabi spectroscopy on the octupole transition, the displacement within the intensity profile of the probe laser would cause an unacceptably large change of the light shift and interfere with the effect of the quasi-static electric field. To avoid this problem, a fraction of the ac trap drive voltage was applied with a phase shift of $\pi/2$ to one of the end caps of the trap. The additional field induces micromotion of the ion but does not lead to a constant displacement, therefore the light shift should stay constant if the additional RF field is applied. As discussed in chapter 2, the electric field along the trap axis at the position of the ion resulting from a voltage applied to one endcap electrode can be calculated as $0.80 \cdot U/2z_0$, where $2z_0 = 0.987$ mm is the design goal of the distance between the electrodes. From the measured frequency shift for different orientations of the quantization axis, $\Delta\alpha_s^{dc} = 1.3(6) \times 10^{-40}\ \mathrm{JV^{-2}m^2}$ was found and it turned out that the tensor polarizability α_t^{dc} is approximately one order of magnitude smaller than α_s^{dc}. The significant uncertainty in α_s^{dc} results from the statistical uncertainty of the measurements and the actual electric field strength acting on the ion which is also used to correct for the quadratic Doppler effect.

3.2.3 Dynamic Electric Polarizability – Light Shift

If the perturbing electric field is not static, but oscillates at an angular frequency ω_l, the denominators in Eq. 3.9 and 3.11 need to be changed to $(W(\gamma', J') - W(\gamma, J))^2 - \hbar^2\omega_l^2$. The resulting dynamic quadratic Stark effect is the so-called light shift and increases significantly if the frequency of the perturbing light comes close to the resonance of dipole transitions of the involved levels. To avoid shifts by the nearly resonant light from the cooling laser and the repump lasers, mechanical shutters block the laser beams during the probe pulse period. It should be noted that even very small fractions of the intensity during the cooling period e.g. scattered light can cause significant shifts of the reference transition. The matrix elements for the reference transitions are several orders of magnitude smaller than those of dipole transitions and do not contribute. The light shift induced by the probe laser light is caused by off-resonant coupling. Due to the small intensity of the probe laser light, the shift effect present during spectroscopy on the quadrupole transition is very small ($\approx 3 \times 10^{-19}$) [80]. For the octupole transition, however, the huge intensity required for excitation makes the light shift the dominant shift effect for Rabi spectroscopy. But also the thermal radiation from the environment affects the ion and leads to a frequency shift, which is discussed in detail in subsection 3.2.4.

3.2.4 Light Shift Cancellation via Extrapolation

As discussed above, the light shift of the probe laser field leads to a significant frequency shift of the octupole transition. Generally, one expects that the light shift contains both scalar and tensor contributions and that the shift $\Delta\nu_{LS}$ caused by a π-pulse with a Fourier-limited spectral width Δf is proportional to $(\Delta f)^2$. This is a direct consequence of the fact that Δf is proportional to the inverse probe pulse duration, which is proportional to the Rabi frequency and in turn to the required electric field under the assumption of a constant pulse area. By recording excitation spectra of the octupole transition for various probe pulse areas and durations $\Delta\nu = 0.65(5)\ \mathrm{Hz}^{-1}(\Delta f)^2$ is found if the polarization and magnetic field orientation are chosen to maximize the excitation probability.

In previous investigations [114] and in the first experiments with the octupole transition at PTB, the absolute frequency of the octupole transition was determined by measuring the frequency of the center of spectra at different probe light powers and then linearly extrapolating to zero power to correct for the light shift. Figure 3.1 shows such a measurement and the uncertainty of the frequency measurement is mostly determined by the uncertainty of the linear fit, which has in turn a significant uncertainty due to drifts of the probe light power.

With the efficient repump scheme a stabilization of the probe light frequency to the octupole transition became possible and with the interleaved servo technique

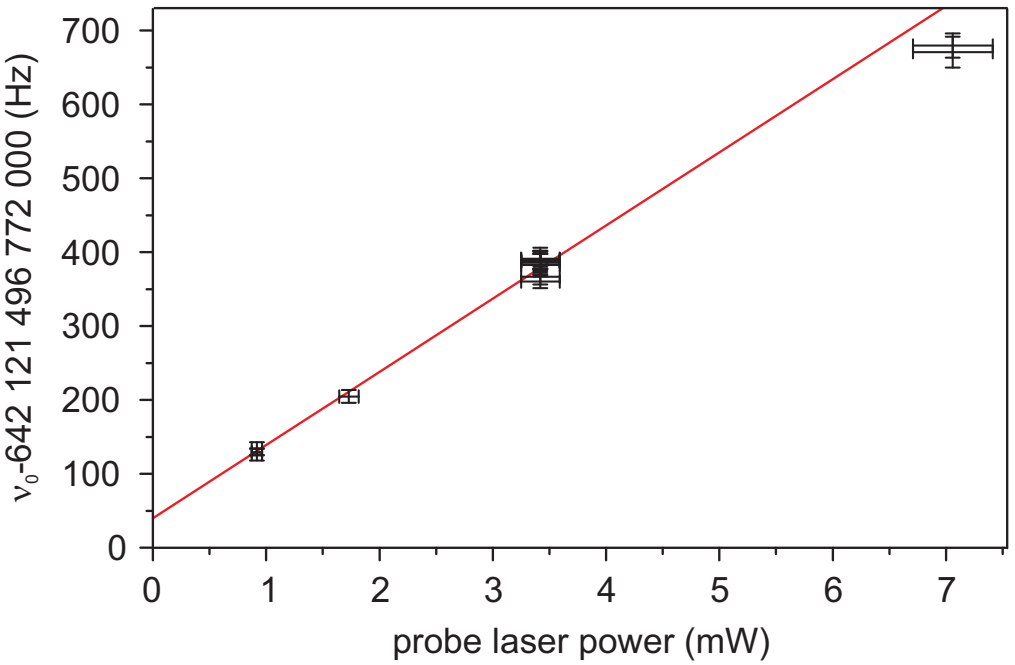

Figure 3.1: Measurement of the unperturbed $^2S_{1/2}(F = 0) \rightarrow {}^2F_{7/2}(F = 3)$ transition frequency ν_0. The measurement data was deduced as the center frequency of recorded spectra for various probe laser powers. The red line is a linear weighted fit to the data and yields $\nu_0 = 642\ 121\ 496\ 772\ 640(8)$ Hz.

the unperturbed frequency was obtained by real-time extrapolation. In this method that is sketched in Fig. 3.2, the probe light power is switched between two settings, so that the intensity of the probe light is alternated between a value I_H and a lower value I_L. The use of an injection locked laser diode at 467 nm results in a high short-term stability of the probe light power and the laser frequency is stabilized to the corresponding light-shifted line center frequencies ν_H and $\nu_L = \nu_H - \nu_{\text{offset}}$ with an independent digital servo system. The unperturbed transition frequency is calculated as $\nu_0 = \nu_H - \nu_{\text{offset}}(1 - I_L/I_H)^{-1}$ so that it depends not on the absolute values of the probe pulse intensities but on their ratio, which is registered together with ν_H and ν_{offset}. For this purpose, the relative intensity of the probe laser light incident on the ion is monitored with a highly linear photodetector mounted behind the trap. A pinhole in front of the photodetector selects the center of the magnified image of the laser beam waist at the position of the ion so that intensity fluctuations due to both total power and pointing instabilities are detected. The high linearity of the photodetector signal in the 10^{-5} range enables the precise measurement of power ratios. Using the real-time extrapolation technique, the frequency of the octupole transition was measured with a fiber-

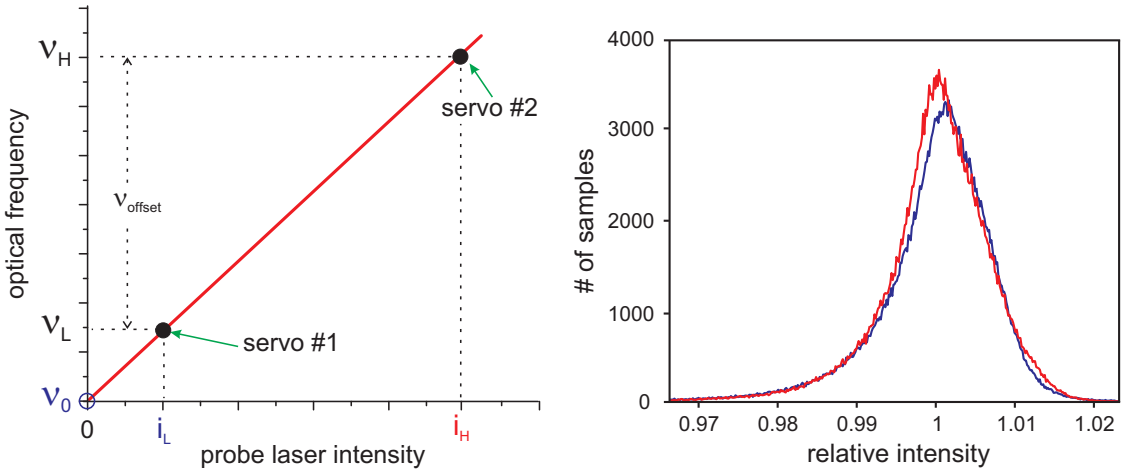

Figure 3.2: On the left: Light shift cancellation by real-time extrapolation. Two alternating servo systems stabilize the laser frequency to the respective line centers ν_H and ν_L for high i_H and low i_L probe laser intensity. The intensity is recorded together with respective frequencies and the unperturbed frequency can be calculated in real-time. On the right: histogram of the relative intensities in the low (blue) and high (blue) mode of operation.

laser-based frequency comb generator [115] using the caesium fountain clock CSF1 [116, 117] in our laboratory as the reference. The results of this measurement are discussed in section 5.2.1. Since the dominant shift of the octupole transition frequency in this measurement is the light shift, it is essential to quantify the uncertainty of the employed extrapolation scheme. No significant contribution to the uncertainty is expected from the nonlinearity of the intensity measurement and higher-order terms in the light shift, as discussed in the following subsection. It furthermore is assumed that the registered average of I_L/I_H reliably represents the intensity ratio at the position of the ion and that probe pulse intensity fluctuations are not correlated with the execution of the measurement cycles. The observed single-pulse intensities I_L and I_H show relative fluctuations of $\approx$1% with a slightly asymmetric distribution presumably resulting from pointing instability. In Fig. 3.2 histograms of I_H and I_L are depicted. Under the assumptions made here, these fluctuations will not lead to an error in the extrapolated frequency and would result in a symmetric distribution of I_L/I_H. The I_L/I_H distributions observed during the absolute frequency measurement, however, show a small asymmetry which is used as a measure for the extrapolation uncertainty. The asymmetry is quantified as the difference between the mean and the most probable value of I_L/I_H. The corresponding deviations in the extrapolated frequencies are in the

range $-27 \ldots 19$ mHz, and the maximum absolute deviation is used as an estimate for the extrapolation uncertainty.

The achieved uncertainty due to the light shift of 4.2×10^{-17} during the first absolute frequency measurement of the octupole transition (see section 5.2.1) can be reduced if the interrogation times are extended, which requires a more stable probe laser. Although the new probe laser system with a lower frequency instability allows us to extend the interrogation times by about a factor of 3 compared to the old one, application of the extrapolation technique will ultimately be limited by the fact that the intensity ratio can not be determined at the position of the ion. The new "hyper-Ramsey" spectroscopy scheme overcomes these limitations and permits significantly smaller uncertainties, as discussed in chapter 4.

3.2.5 Non-linearity of the Light Shift

For application of the light shift extrapolation technique, a high linearity of the light shift versus the light intensity is assumed. Nonlinear contributions can occur if $\Delta m \neq 0$ transitions are not well suppressed especially if the light shift $\Delta\nu_{LS}$ becomes comparable with the Larmor frequency. To experimentally investigate a possible nonlinear contribution of the light shift, the interleaved servo technique is used to measure the difference of the transition frequency with the regular Larmor frequency $\Delta\nu_{Z1}(^2\mathrm{F}_{7/2}, F = 3) \approx 65$ kHz and a smaller value. To maximize the effect, the experiment is performed with maximum intensity of the probe laser light that induces ≈1 kHz light shift. As shown in Fig. 3.3, a frequency offset is measurable if the Larmor frequency is significantly reduced. In this case, the light shift becomes comparable with the Lamor frequency and the light shift can no longer be treated as a small perturbation. The observed frequency offset does neither show $1/(\Delta\nu_{Z1})$ nor $1/(\Delta\nu_{Z1})^2$ dependence, but an empirical fit of $a/b^{\Delta\nu_{Z1}(\mathrm{Hz})}$ via a and b is capable to approximate the measured frequency offset. Here, $a = 2.7(2)$ Hz and $b = 42(2)$ were determine by nonlinear regression. The extrapolated fractional shift for normal operation conditions is in the 10^{-20} range. This supports the assumption of negligible non-linearity of the light shift, but a more profound investigation would be necessary to predict reliably nonlinear contributions of the light shift.

Another way to determine the nonlinear light shift directly requires an extension of the interleaved stabilization technique, so that three different sets of parameters can be used. In this case, the induced frequency shifts should be directly measurable and a nonlinear contribution would be easily observable. Since the shift effect appears to be very small even under extreme conditions and does not lead to uncertainties if the "hyper-Ramsey" spectroscopy technique is used, no further investigations on this subject have yet been performed.

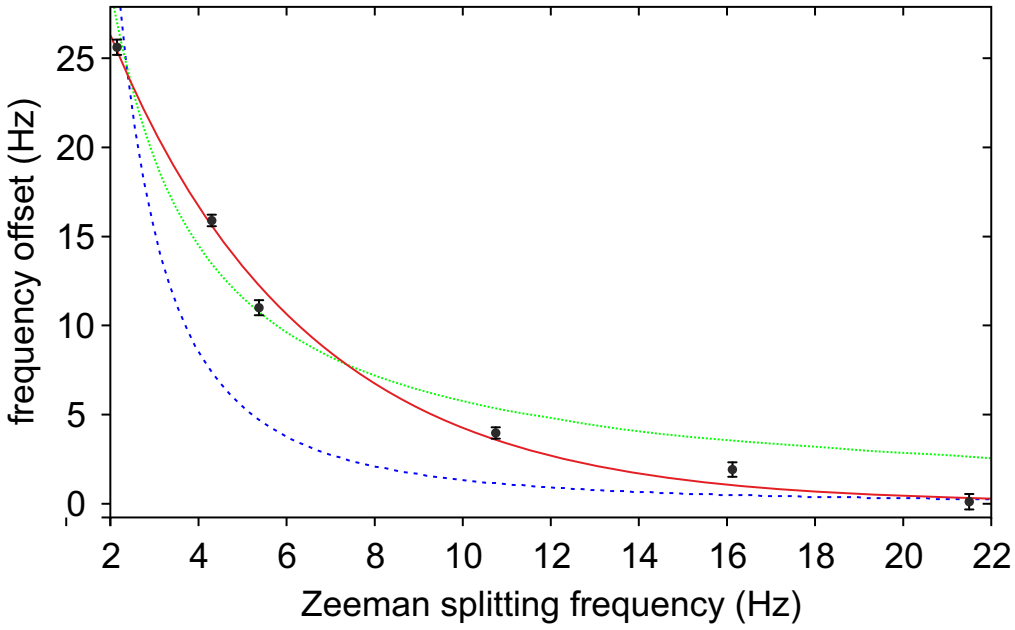

Figure 3.3: Frequency offset of the octupole transition for spectroscopy with ≈1 kHz light shift and reduced magnetic field strength. All measurements are performed using the alternating servo scheme versus operation with a Zeeman splitting frequency $\Delta\nu_{Z1}(^2\mathrm{F}_{7/2}, F = 3) \approx 65$ kHz. The data does neither show $1/(\Delta\nu_{Z1})$ (dotted line) nor $1/(\Delta\nu_{Z1})^2$ (dashed line) dependence, thus an empirical fit of $a/b^{\Delta\nu_{Z1}(\mathrm{Hz})}$ via a and b is performed (solid line).

3.2.6 Blackbody Radiation Shift

The most important contribution to the systematic uncertainty of many optical frequency standards results from the uncertainty in the Stark shift due to the thermal radiation from the environment of the ion or atom. In our case, the temperature rise of a copy of the trap with attached PT100 sensors was measured and the results verified by tests with an IR camera. With this information, a finite element method based simulation was performed, and the effective temperature rise ΔT under the approximation of isotropic radiation was calculated to be 2(1) K [118]. According to the Planck radiation law, the spectral energy density of radiation with a wavelength λ from a blackbody at given temperature T is:

$$u_\lambda(T) = \frac{8\pi hc}{\lambda^5} \frac{1}{e^{\frac{hc}{\lambda k_B T}} - 1}, \tag{3.11}$$

where c is the speed of light, k_B is Boltzmann's constant and h denotes Planck's constant. By spectral integration of $u_\lambda(T)$, the mean-squared electric field is:

$$\epsilon_0 \langle E^2_{BBR}(T) \rangle = \frac{8\pi^5 (k_B T)^4}{15 c^3 h^3} = \epsilon_0 \left(831.95 \frac{\mathrm{V}}{\mathrm{m}} \right)^2 \left(\frac{T}{300\ \mathrm{K}} \right)^4 . \tag{3.12}$$

The position of the maximum of $u_\lambda(T)$ is described by Wien's law and is close to 10 μm at room temperature. This wavelength can be compared to the wavelength of transitions that lead to the differential scalar polarizability of the transition of the ion. The tensor part is averaged to zero under the assumption of isotropic radiation. The longest wavelength of a dipole transition considerably contributing to the differential polarizability of the quadrupole transition is at 2.4 μm and for the octupole transition at 377 nm. In the latter case, the matrix element of the transition from the $^2\mathrm{F}_{7/2}$ to the $^2\mathrm{D}_{5/2}$ at 3.4 μm is so small that its contribution is negligible [88,89]. Since the thermal radiation peaks at much longer wavelength, it is convenient to express the induced shift with the static differential polarizability as

$$\Delta\nu_{\mathrm{BBR}}(T) = -\frac{1}{2h} \Delta\alpha_s^{\mathrm{dc}} \langle E^2_{BBR}(T) \rangle (1 + \eta(T)). \tag{3.13}$$

Here, h is Planck's constant and $\eta(T)$ describes the dynamic character of the shift effect. Figure 3.4 shows the fractional blackbody shift for both transitions calculated with the corrected matrix elements as in table 3.1 [60, 112]. For the quadrupole transition a significant dynamic correction $\eta(300\ \mathrm{K}) \approx 0.13$ has to be considered. In the case of the octupole transition, $\eta(300\ \mathrm{K})$ is a very small correction at room temperature and amounts to less than 0.002.

3.2.7 Measurement of the differential polarizability of the Octupole Transition

As discussed before, all transitions that are relevant for the Stark shift due to thermal radiation have transition wavelengths smaller than 400 nm. Figure 3.7 shows the dynamic differential scalar polarizability of the octupole transition versus the wavelength of the radiation calculated with theoretical matrix elements. It is clearly visible that radiation of near infrared lasers at a wavelength around 1 μm can be used to study the effect of thermal radiation centered at 10 μm. Calculations based on corrected and uncorrected dipole matrix elements predict $(\Delta\alpha_S(1.5\ \mu\mathrm{m})/\Delta\alpha_S(10\ \mu\mathrm{m}) - 1) < 10\%$.

Following this idea, a commercially available fiber laser at 1545 nm with a maximum output power of ≈110 mW, a Nd:YAG at 1064 nm (≈500 mW) and a laser diode at 852 nm (≈300 mW) were used to induce light shifts at the position of the ion. To improve the beam profile, the output modes of the Nd:YAG and the diode laser were cleaned by a single-mode polarization-maintaining fiber, which reduced

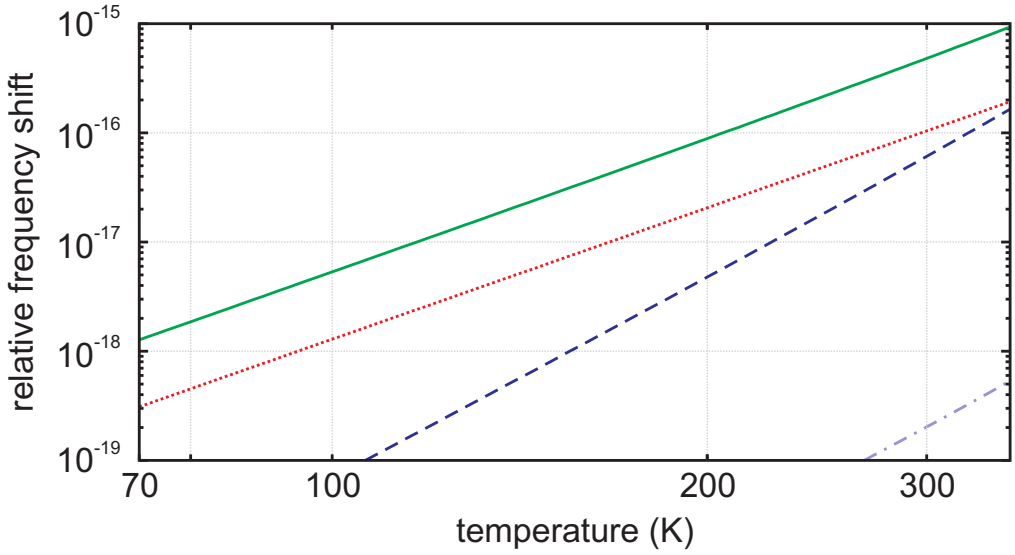

Figure 3.4: Fractional frequency shift of the quadrupole (E2) and octupole (E3) transition of $^{171}Yb^+$ as a function of the ambient temperature that causes the perturbing thermal radiation. The solid line shows the shift effect of the E2 transition calculated using the static scalar differential polarizability $\Delta\alpha_s^{dc}$ and the dashed line is the correction to this value due to the dynamical character of the shift. The shift effect on the E3 transition is depicted by the dotted line and its dynamical correction (dash-dotted) is negligible small.

the available optical power by a factor of 2. In the measurement of the dynamic differential polarizability, the intensity of the laser radiation, the frequency shift and the angle between the electric field and the quantization axis need to be determined. The linear polarization of the laser beam is carefully aligned to minimize losses of the windows of the vacuum enclosure that are mounted close to Brewster's angle. Using the high accuracy with which the orientation of the magnetic field can be adjusted, the tensor part of the light shift can be inferred from two measurements with different orientations of the magnetic field. By averaging the light shift over three mutually orthogonal orientations of the magnetic field, the tensor part is removed and the scalar differential polarization remains [111]. To measure the induced frequency shift, the interleaved stabilization technique is applied. A mechanical shutter blocks the additional laser in all parts of the interrogation scheme, except the corresponding probe pulse period.

Since it is experimentally difficult to determine the beam waist of the light shifting laser at the position of the ion, the experimental setup was modified as depicted in Fig. 3.5. A 3.1 mm thick glass plate was installed oriented to minimize reflection in front of the magnetic shielding that surrounds the ion trap. By tilting

the glass plate the beam is transversely shifted at the position of the ion. Doing so, the laser beam profile can be moved over the ion. The reflection of a HeNe laser beam from the glass plate is used as a pointer on a screen at a distance of approximately 4 m. In this way, the light shift profile can be determined by recording the light shift, the relative laser power and the position of the pointer laser on the screen.

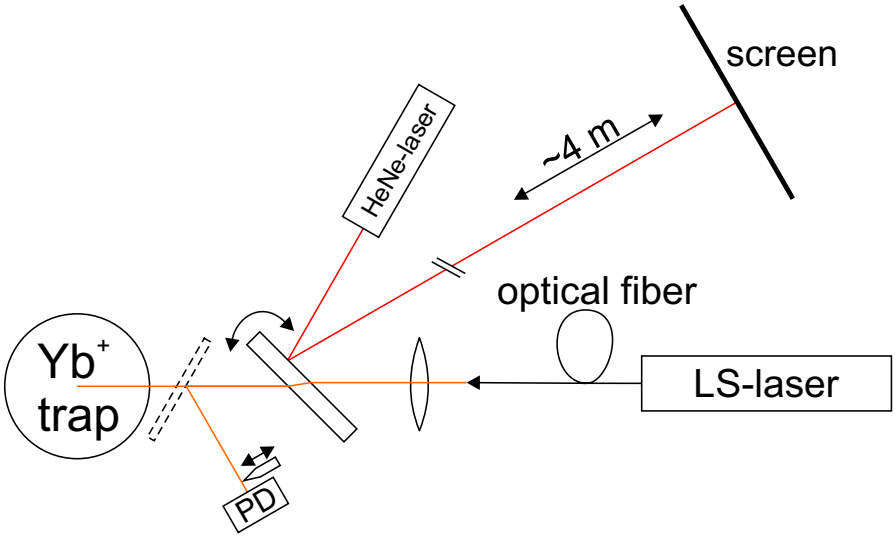

Figure 3.5: Schematic of the setup used to determine the light shift profile. The light shift is measured for various points without the dashed mirror, which is installed after the measurement, and permits a calibration of the displacement on the screen to the length at trap center.

After recording the light shift profile, a mirror was installed in front of the trap to reflect the laser beam, so that the displacement of the laser beam induced by a variation of the angle of the glass plate can be determined. The displacement was measured with a knife edge mounted on a linear stage in front of a photodetector. The position of the beam waist was determined for 8 positions of the pointer beam on the screen in the horizontal and the vertical direction. This enables a calibration of the displacement measured at the screen to the length at trap center and therefore the measured light shift profile. The relative uncertainty of this length calibration is about 1%. Since the glass plate is installed after the focusing lens, variations of the glass plate angle can induce small variations of the position of the focus along the optical axis. However, due to the small angle changes of less than $\pm 5°$, the relatively weak focusing (divergence $\Theta < 0.3°$) and the fact that the ion is close to the beam waist, this effect can be neglected.

Since the reflectivity of the glass plate that induces the displacement slightly varies under angle changes, the change of transmitted optical power was measured

and the light shift profile corrected. This is only a very small correction of less than 1%. The optical power of the laser radiation was measured with a power meter before and after recording the light shift profile. The optical power was assumed to be the geometric mean value of the measurement in front and behind the trap, which agreed within 1%. The power meter was calibrated at PTB's radiometry laboratory using 30 mW laser radiation at 1064 nm with an uncertainty of 0.5%. During the recording of light shifts, the relative optical power at each measurement point was monitored by the output power indication on the laser controller or by the signal of a highly linear photodetector, measuring a small fraction of the total output power. Since this relative optical power measurement was not continuously performed, power fluctuations can not be entirely excluded, so that the uncertainty of the optical power is assumed to be less than 3%. This offers potential to reduce the uncertainty in further measurements.

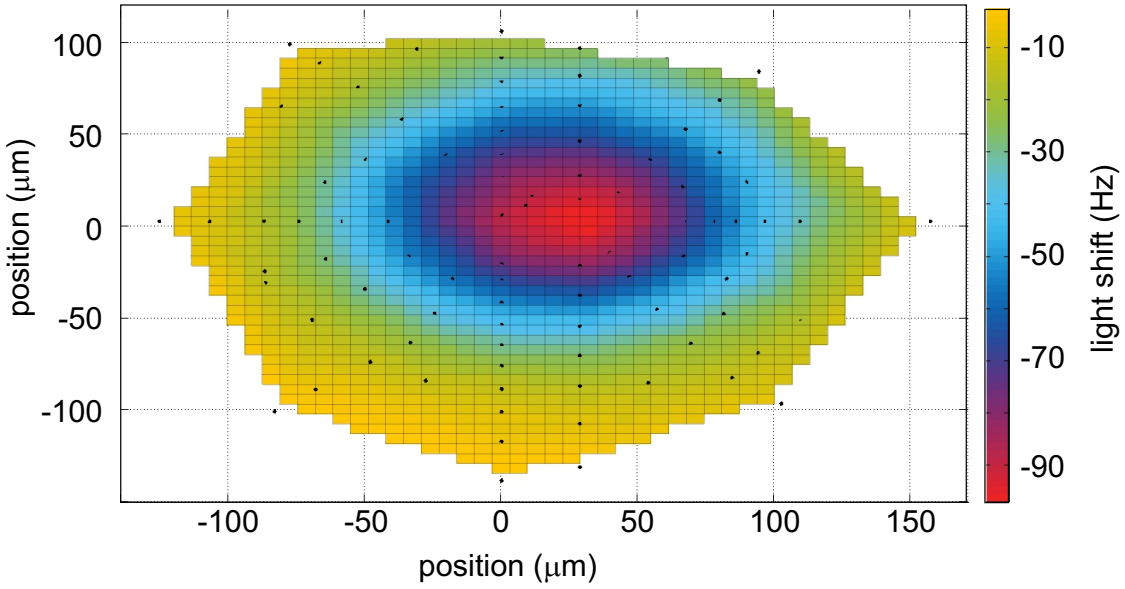

Figure 3.6: Light shift profile induced by the 1.5 μm laser. The black dots indicate measurement points and the color surface is a smoothed linear fit between the points.

Figure 3.6 shows the light shift profile induced by the 1.5 μm laser. It is important to find a limited function that precisely describes the measured values and is integrable. For the measurement at 1.5 μm and 1064 nm the measured distribution is fitted by an intensity distribution similar to that of Hermite-Gaussian modes.

An intensity profile with such symmetry is expected due to the glass plates at Brewster's angle in the beam path. To lowest order such functions are:

$$I_{0,0}(x,y) = I_{00}\, e^{\frac{-2(x-x_0)^2}{\omega_x^2}} e^{\frac{-2(y-y_0)^2}{\omega_y^2}} \tag{3.14}$$

$$I_{1,0}(x,y) = I_{10}\, \frac{2(x-x_0)^2}{(r\omega_x)^2} e^{\frac{-2(x-x_0)^2}{(r\omega_x)^2}} e^{\frac{-2(y-y_r)^2}{(r'\omega_y)^2}} \tag{3.15}$$

$$I_{0,1}(x,y) = I_{01}\, \frac{2(y-y_r)^2}{(r\omega_x)^2} e^{\frac{-2(x-x_0)^2}{(r\omega_x)^2}} e^{\frac{-2(y-y_r)^2}{(r'\omega_y)^2}}. \tag{3.16}$$

For each wavelength at least two measurements were performed. Fitting with $I_{0,0}(x,y)$ gives a very good agreement. The residuals can be approximated by $I_{1,0}(x,y)$ and $I_{0,1}(x,y)$. The remaining values do not show a clear structure and χ^2 is calculated to be close to one. The fitted functions are numerically integrated and the uncertainty of the spatially integrated light shift is estimated from the difference between the single measurements at each wavelength. Additionally, the improvements over the fit with the basic distribution $I_{0,0}(x,y)$ are used to gain confidence in the integrated value. For the measurement at 852 nm, the residuals of a fit with $I_{0,0}(x,y)$ can be described by a second function $I_{0,0}(x,y)$ with a different x_0 and a smaller ω_x and otherwise unchanged parameters. In contrast to the other two lasers, the 852 nm light source was a free running laser diode, so that single mode operation is not guaranteed, which might cause a different intensity profile. Table 3.2 summarizes the differential polarizability measurements.

As shown in Fig. 3.7 the measured $\Delta\alpha_s$ do not agree with the calculations based on the theoretical matrix elements. By using the lifetime correction as discussed in subsection 3.2.1 the agreement becomes better, however, a significant difference remains. In the range between 700 nm and 10 μm both theoretical differential polarizabilities can be approximated as the result of a single transition at about 400 nm plus a constant value, the static differential polarizability:

$$\Delta\alpha_s(\lambda) = \Delta\alpha_s^{\mathrm{dc}} - \frac{f}{\lambda^2 - \lambda_0^2}. \tag{3.17}$$

The same model is assumed for the experimental values. Due to the small number of measured values and the degrees of freedom in the theoretical model, the uncertainty of $\Delta\alpha_s^{\mathrm{dc}}$ is estimated from fits for very different constant λ_0 in the range from 370 nm to 530 nm. In this way, $\Delta\alpha_s^{\mathrm{dc}}$ was found to be equal to $0.893(30) \times 10^{-40}\mathrm{Jm^2V^{-2}}$, where the uncertainty results mainly from the uncertainty due to the optical power measurement. As expected from the theoretical description, the fit of the experimental data shows that $\Delta\alpha_s(1.545\ \mu\mathrm{m})$ and $\Delta\alpha_s^{\mathrm{dc}}$ differ by about 10%. Furthermore, a very small dynamic correction is found since $\Delta\alpha_s(10\ \mu\mathrm{m}) = 0.891(30) \times 10^{-40}\mathrm{Jm^2V^{-2}}$ is very close to $\Delta\alpha_s^{\mathrm{dc}}$. This suggests to express the blackbody radiation shift as

$$\Delta\nu_{\mathrm{BBR}}(T) = 1/(2h)\Delta\alpha_s(10\ \mu\mathrm{m})\langle E_{BBR}^2(T)\rangle. \tag{3.18}$$

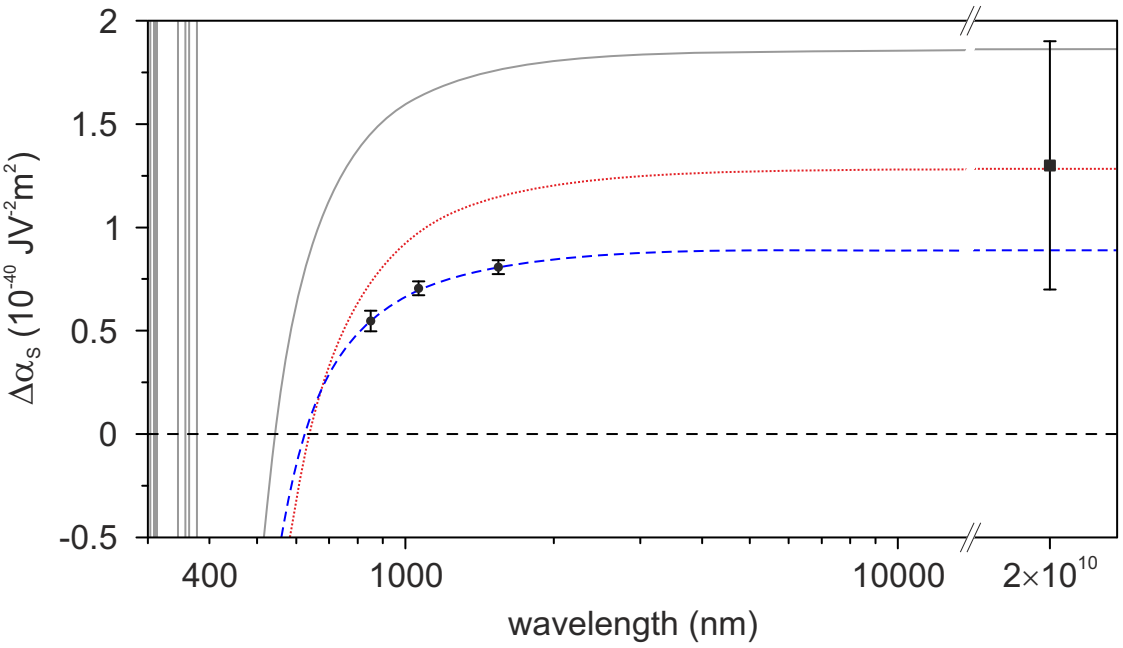

Figure 3.7: Scalar differential polarizability $\Delta\alpha_s$ of the octupole transition as a function of the wavelength. The solid gray line is calculated using tabulated oscillator strengths [60], and for the dotted red line the data were corrected according to experimental life times [112]. The circles show the result using near-infrared laser radiation and the square shows the result obtained with a quasi-static field. The dashed blue line is a fit to the experimental values (see text).

In this way, with the measured value and the effective temperature $T = 298(1)$ K a shift of -45.4(1.6) mHz can be calculated, which corresponds to a fractional frequency shift of $-70.7(2.6) \times 10^{-18}$. The uncertainty here results mostly from the uncertainty of $\Delta\alpha_s(10\ \mu\text{m})$, the uncertainty of the effective temperature leads to an uncertainty of only 1.0×10^{-18}.

The measurements of the light shifts were performed with the orientation of the quantization axis at an angle of 90° and 45° to the electric field of the light shifting laser radiation. This permits an additional comparison of the results obtained from theoretical matrix elements to the experimental data via the tensor polarizability. This part of the polarizability results only from a shift of the $^2F_{7/2}$ level and the dipole transitions contribute in a different way than in the case of the scalar shift (see Eq. 3.9 and Eq. 3.11). The resulting polarizabilities are given in Tab. 3.2 and shown in Fig. 3.8, together with the theoretical results. In contrast to the scalar polarizability, the agreement of the theoretical result with the experimental data is reduced due to the use of a correction based on the experimental lifetimes.

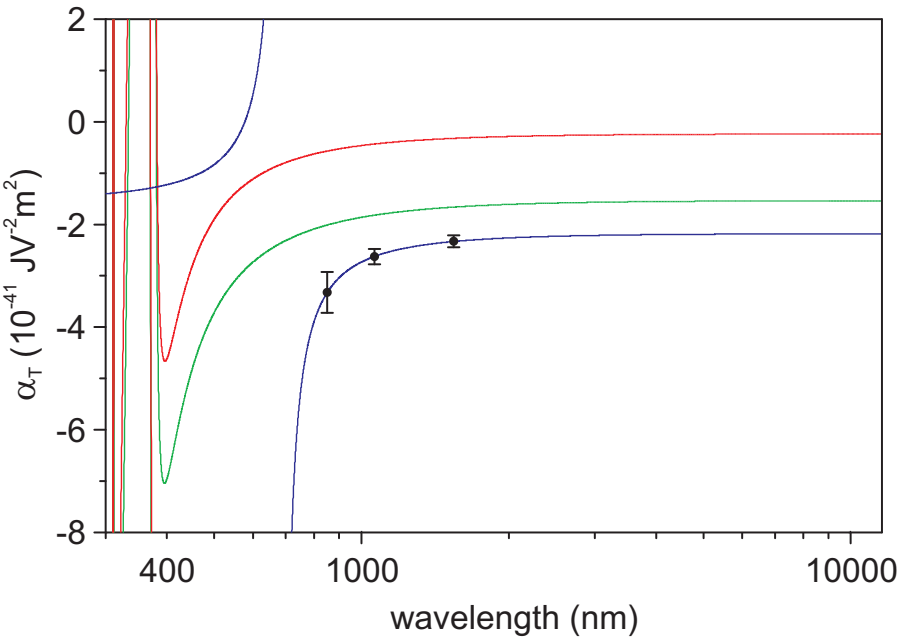

Figure 3.8: Tensor polarizability $\Delta\alpha_T$ of the $F = 3$) hyperfine component of the $^2F_{7/2}$ state as a function of the wavelength of the perturbing laser radiation. The solid green line is calculated using tabulated oscillator strengths [60], and the red line uses a correction based on experimental life times [112]. The circles show the result using near-infrared laser radiation and the blue line is a fit to the experimental values (see text).

After the measurement on the octupole transition, a measurement on the quadrupole transition was performed with each laser. The polarizability of the $^2D_{3/2}$ state for wavelengths larger than 1.4 μm is dominated by the contribution from the transition to the $^2P_{1/2}$ state at 2.4 μm. As a result, no precise information on the response of the quadrupole transition to thermal radiation can directly be obtained from the measurements with the near-infrared lasers. However, the measured dynamic differential polarizability can be used as a test case for theoretical predictions. Furthermore, the combination of all measured scalar differential and tensor polarizabilities of the quadrupole and octupole transition might lead to an optimized set of dipole matrix elements and in turn improve the estimates on $\Delta\alpha_s^{dc}$. For completeness, the results for the quadrupole transition are added to table 3.2.

3.2.8 Quadratic Stark shift induced by the trap field

Beside the electric field of the thermal radiation, the states of the ion are affected by the residual trap field that appears due to uncompensated stray fields and the

Table 3.2: Measured differential scalar electric polarizabilities $\Delta\alpha_S$ and tensor polarizabilities α_T for the two clock transitions of $^{171}Yb^+$ induced by laser radiation of various wavelengths. For the octupole (E3) transition these measurements permit extrapolation to a static perturbing field (dc_{LS}). The last column shows results obtained with a quasi-static electric field (dc). All values are given in $10^{-40}Jm^2V^{-2}$.

	852 nm	1064 nm	1545 nm	dc_{LS}	dc
$\Delta\alpha_S(E3)$	0.547(50)	0.705(34)	0.808(34)	0.893(30)	1.3(6)
$\alpha_T(^2F_{7/2}, F=3)$	-0.332(40)	-0.262(15)	-0.233(12)	-0.218(12)	≈-0.13
$\Delta\alpha_S(E2)$	-16.9(1.5)	-12.2(6)	-9.5(4)	-	6.9(1.4) [70]
$\alpha_T(^2D_{3/2}, F=2)$	-0.79(9)	0.35(7)	8.6(5)	-	-13.6(2.2) [70]

kinetic temperature of the ion in the trap potential as discussed in section 2.1. The mean squared electric field is quantified using Eq 2.11 for the two transitions and the induced shift described with Eq. 3.7. Frequency shifts due to the tensor polarizability average out if the frequency standard is alternately operated at one of three mutually orthogonal directions of the quantization axis [111]. This is similar to the cancellation of the electric quadrupole shift as discussed in the next chapter. Due to the suppression of the tensor shift by at least a factor of 50 and its relatively small magnitude, one can simplify Eq. 3.7 by neglecting its contribution. Hence, the expected fractional frequency shift is $\Delta\nu_{QS}/\nu_0 = -1/(2h)\Delta\alpha_S^{DC}\sum_{i=x,y,z}\langle E_i^2\rangle/\nu_0$ and equals $-1.2(0.6)\times10^{-18}$ for the octupole transition. The larger relative shift of $-6.7(3.7)\times10^{-18}$ for the quadrupole transition results from the significantly larger differential scalar polarizability of $6.9(1.3)\times10^{-40}Jm^2V^{-2}$ [70]. The uncertainties of the frequency shifts mainly result from the uncertainty of the electric field, which contains the total uncertainty due to stray electric fields and assumes 50% uncertainty in the temperature of the ion.

3.3 Electric Quadrupole Shift

After the discussion of frequency shifts due to interaction with the electric field, this section treats the so-called electric quadrupole shift that results from the interaction of the electric quadrupole moment of the state with the gradient of the electric field. Under normal operation conditions, electric fields are well compensated, however, a significant electric field gradient can be present at trap center.

A detailed discussion of the electric quadrupole shift and the derivation of the relevant equations can be found in Ref. [111]. Since the electric quadrupole shift for the $^2S_{1/2}$ state is zero, for the octupole transition only the $^2F_{7/2}(F=3)$ state is

relevant. The shift due to an electric field gradient A can be calculated according to Ref. [111] as

$$\Delta\nu_Q = \frac{5}{7h} A\Theta(F, 7/2)(3\cos^2\beta - 1), \tag{3.19}$$

where h is the Planck constant and β is the angle between the symmetry axis of the gradient and the quantization axis. As also pointed out in Ref. [111] the induced frequency shift averages to zero if the frequency is measured for three mutually orthogonal directions of the magnetic field that defines the quantization axis.

3.3.1 Measurement of the Quadrupole Moments

To determine the electric quadrupole moment $\Theta(F, 7/2)$, the frequency shift induced by a known electric field gradient needs to be measured. For our trap with small deviations from a cylindrical symmetry of the trap potential, the gradient $A = U_0/(\kappa r_0^2)$ is produced by applying a static voltage U_{dc} to the ring electrode. The geometrical factor $1/(\kappa r_0^2) = 7.9989(54) \times 10^5$ m^{-2} was determined by fitting measurements of the secular frequencies obtained using the interleaved servo technique stabilizing at the carrier and the sideband frequency for different dc voltages U_0 to the theoretical dependence given in Eq. 2.6 and Eq. 2.3 (see Fig. 3.9). The fitting is very similar to the determination of the applied electric field gradient in other measurements of electric quadrupole moments of states used in single-ion clocks, e.g. in Ref. [119]. The measurement of $\Theta(F, 7/2)$ was performed using the interleaved servo technique with U_0 alternating between zero and a preset value. Since the selection rules of the octupole transition lead to a very small relative excitation probability for the most sensitive direction $\beta = 0°$, $\beta = 90(1)°$ was chosen. The induced frequency shifts are shown in Fig. 3.10, the slope of the fit yields $\Theta(F, 7/2) = -0.041(5)\ ea_0^2$, where e is the elementary charge and a_0 the Bohr radius. The uncertainty is dominated by the statistical uncertainty of the measured frequency differences. This experimental value is significantly smaller than the theoretical estimate of $\Theta(F, 7/2) = -0.22\ ea_0^2$, obtained by a single-configuration Hartree-Fock calculation [64]. The discrepancy is not surprising in view of the complex electronic configuration of the $^2\mathrm{F}_{7/2}$ state. So far, it was not possible, even with more sophisticated methods, to calculate $\Theta(F, 7/2)$ with a precision comparable with the experimental uncertainty [62].

3.3.2 Stability and Cancellation of the Electric Quadrupole Shift

As discussed in detail in Ref. [85], the variations of the stray field compensating voltages can be used to indicate variations of the stray field gradient. After loading an ion to the trap, these voltages show significant variations that decay within a few weeks (see Fig. 2.3). All measurements reported here were conducted several

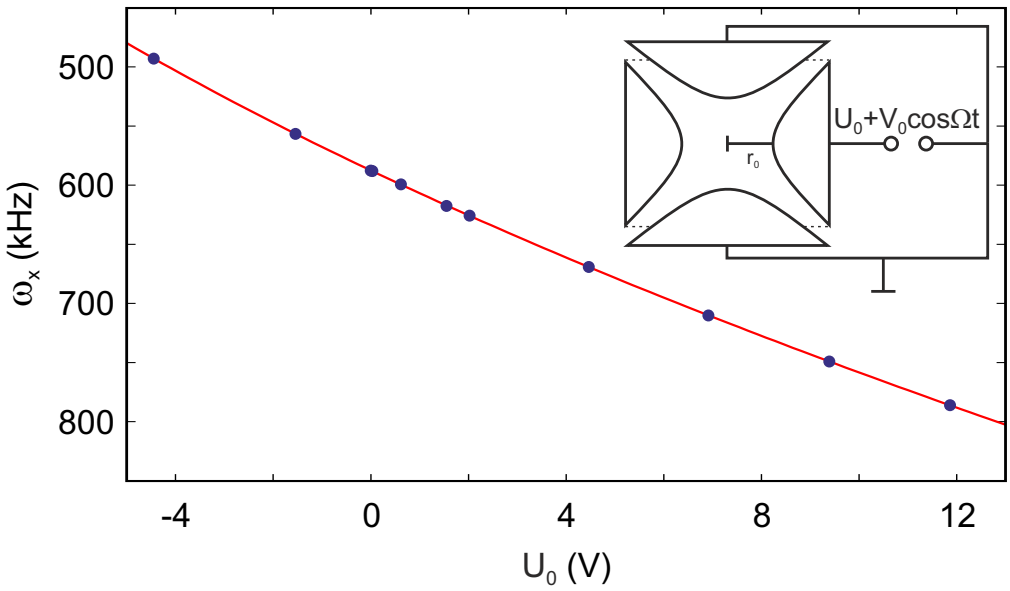

Figure 3.9: Frequency of the first secular sideband ν_x versus the dc voltage U_0 on the ring electrode of the ion trap. The blue dots show the result of a measurement using the interleaved servo technique (see text) with uncertainties smaller than the size of symbol and the line is a fit of the theoretical prediction (Eq. 2.6) to the measurement data.

weeks after loading and the stray field compensation remained stable within the compensation uncertainty.

To estimate the residual electric quadrupole shift induced by electric stray field gradients, measurements are performed with the quadrupole transition. Due to the ≈50 times larger electric quadrupole moment of the $^2D_{3/2}$ state, even small gradients can be detected. For this purpose the interleaved stabilization is used and the orientation of the quantization axis is switched between two settings. In this way, the frequency shifts of the quadrupole transition for each orientation were inferred from three pairs of field directions as 0.41(2) Hz, −0.47(2) Hz, and 0.06(2) Hz, where the uncertainty is predominantly statistical. This investigation was carried out during the measurement of the absolute frequency of the quadrupole transition discussed in section 5.3 and the shifts remained stable within their statistical uncertainty during the measurement period. Since the orientation of the magnetic field used for operation of the frequency standard based on the octupole and the quadrupole transition are different, β will not be the same. However, in no measurement with the quadrupole transition for various β and even directly after loading an ion to the trap, a shift $|\Delta\nu_Q|$ larger than 0.5 Hz had been observed. Due to the significantly smaller quadrupole moment of the $^2F_{7/2}(F = 3)$ state, for the

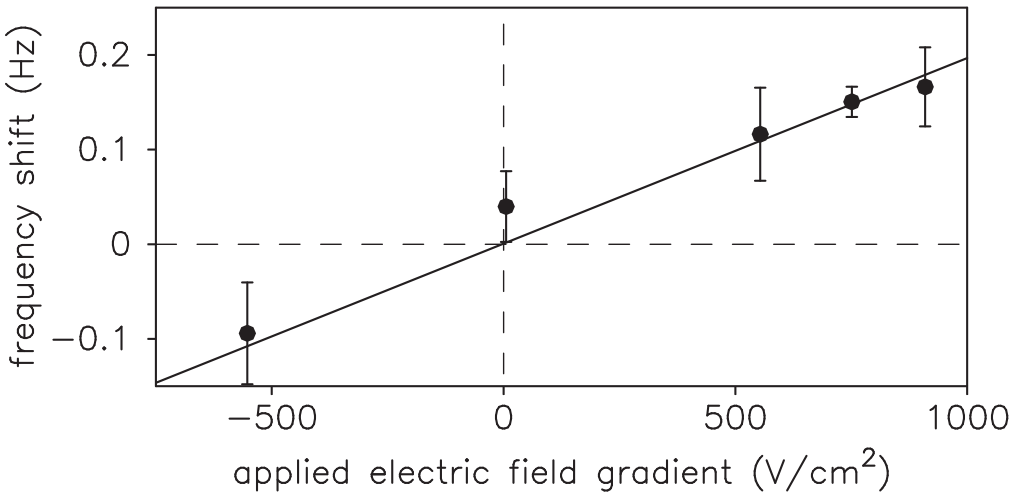

Figure 3.10: Quadrupole shift of the octupole transition frequency resulting from an applied electric field gradient, measured using the interleaved servo technique (see text). The solid line is a linear least-square fit through the origin. The error bars denote statistical uncertainty.

octupole transition this maximum measured shift would result in a relative change of the transition frequency by less than 2×10^{-17}.

As pointed out before, the quadrupole shift can be efficiently suppressed if the observed transition frequency is averaged for three mutually orthogonal directions of the quantization axis. On the other hand this fact can be used to test the accuracy with which a set of mutually orthogonal directions is realized. Therefore, an electric field gradient was induced by setting the dc voltage on the ring electrode $U_0 = 12.5$ V and measuring the induced frequency shift on the quadrupole transition for three pairs of orientations. The determined shifts averaged to zero within their statistical uncertainty and show a suppression of the shift effect through averaging by more than a factor of 50. This result supports an uncertainty of 1° for the two angles that are used to describe the magnetic field orientation in our trap. If this technique is used for the suppression of the quadrupole shift on the octupole transition for normal operation conditions, the shift averages to zero with an uncertainty of 3.1×10^{-19}. For the quadrupole transition an uncertainty of 1.6×10^{-17} results from the significantly larger electric quadrupole moment $\Theta(\mathrm{D}_{3/2}) = 2.08(11)\ ea_0^2$.

3.4 Zeeman Shift Effects

In the presence of an external magnetic field the hyperfine states split into their Zeeman components. In our experiment a weak magnetic field with a flux density

of 3.58 μT creates a well defined quantization axis for the interaction of the ion with laser radiation. The Hamilitonian that describes this effect has the following form [111]:

$$H_Z = g_J \mu_B \mathbf{J} \cdot \mathbf{B} + g'_I \mu_B \mathbf{I} \cdot \mathbf{B}, \tag{3.20}$$

where $\mathbf{B} = Be_z$ is the magnetic flux density of the field, $\mathbf{J}$ is the electronic angular momentum and $\mathbf{I}$ is the nuclear spin. The electronic g-factor g_J as well as the nuclear g-factor g'_I are expressed in units of the Bohr magneton μ_B. The contribution of the nuclear part is small compared the electronic part, as $g'_I = 5.36 \times 10^{-4}$ for $^{171}Yb^+$ [120]. Thus its treatment is only required if the electronic part of the quadratic Zeeman shift is known with comparable precision, as it is the case for the quadrupole transition [121].

As long as the magnetic field induced shifts are weak compared to the hyperfine splitting, H_Z can be diagonalized in the same basis of states $|\gamma JFm_F\rangle$ with the quantum numbers I, J, F, and m_F denoting the nuclear spin, the electronic angular momentum, the total angular momentum, and its projection on the direction of B. According to Ref. [122] the matrix elements of J_z are:

$$\langle \gamma JFm_F | J_z | \gamma JF'm_F \rangle = (-1)^{F-m_F} (\gamma JF||J_z||\gamma JF') \begin{pmatrix} F & 1 & F' \\ -m_F & 0 & m_F \end{pmatrix}, \tag{3.21}$$

with the reduced matrix element

$$(\gamma JF||J_z||\gamma JF') = (-1)^{I+J+1+F} \sqrt{J(J+1)(2J+1)(2F+1)(2F'+1)} \cdot \begin{Bmatrix} J & F & I \\ F' & J & 1 \end{Bmatrix}. \tag{3.22}$$

The induced linear frequency shift for the $\langle \gamma JFm_F|$ state is:

$$\Delta\nu_{Z1}(\gamma JFm_F) = \frac{(-1)^{F-m} \mu_B g_J B}{h} (\gamma JF||J_z||\gamma JF') \begin{pmatrix} F & 1 & F' \\ -m_F & 0 & m_F \end{pmatrix} \tag{3.23}$$

$$= \frac{\mu_B g_J B}{h} \frac{F(F+1) + J(J+1) - I(I-1)}{2F(F+1)} \cdot m_F, \tag{3.24}$$

and the previously neglected contribution from the nuclear magnetic moment is:

$$\Delta\nu_{Z1}(\gamma JFm_F) = -\frac{\mu_B g'_I B}{h} \frac{F(F+1) - J(J+1) + I(I-1)}{2F(F+1)} \cdot m_F. \tag{3.25}$$

The two clock transitions of Yb^+ are between states with $m_F = 0$, so that the transition frequency is not affected by the magnetic field according to the linear Zeeman effect, but they show the second-order Zeeman shift that can be calculated in second-order perturbation theory to be:

$$\Delta\nu_{Z1,I}(\gamma JFm_F) = \frac{\mu_B^2 g_J^2 B^2}{h} \sum_{F' \neq F} \frac{|\langle \gamma JFm_F | J_z | \gamma JF'm_F \rangle|^2}{E_F - E_{F'}}. \tag{3.26}$$

Here $(E_F - E_{F'})/h = \Delta\nu_{HF}$ is the hyperfine splitting frequency, and the contribution of the nuclear magnetic moment is included if g_J is replaced by $(g_J + g'_I)$.

According to this model, the Zeeman shifts of the relevant levels can in principle be calculated with very high precision. For the $^2S_{1/2}$ and the $^2D_{3/2}$ state accurate information on the electronic g-factors became recently available [123]. They can be used to calculate the linear Zeeman shift with high precision [121] and permit together with the high-accuracy measurements of the hyperfine splittings frequencies [121,124] similar accuracy for the quadratic Zeeman effect. For the $^2F_{7/2}$ state $\Delta\nu_{HF} = 3620.58(2)$ MHz was determined, but presently no precise information on the g-factor is available. In the pioneering work of W. F. Meggers, an experimental value $g_{7/2} = 1.145$ and the calculated $g_{7/2} = 1.143$ can be found [125]. For the two other states, the calculated values show better agreement with the accurate values from [123], so that the calculated value will be used for the $^2F_{7/2}$ state and its uncertainty is estimated as 3×10^{-3}.

The calculated shift coefficient due to the quadratic Zeeman effect on the octupole transition of $-2.14(9)$ mHz/μT^2 is approximately a factor of 25 times smaller than that of the quadrupole transition. This is caused by the fact that in the case of the octupole transition both levels are lowered by the magnetic field, whereas in the quadrupole transition, the $^2D_{3/2}(F = 2, m_F = 0)$ state is raised. This result for the octupole transition shows a clear discrepancy with a measurement of 1.72(3) mHz/μT^2 presented in Ref. [126].

The fact that the flux density at the position of the ion can be inferred from spectroscopy on the $\Delta m = 0$ and $\Delta m = \pm 1$ components of the quadrupole transition can be used to significantly improve the accuracy of the shift correction and give additional information about the discrepancy with the published value. Therefore, a stronger magnetic field is applied during the probe pulse period similar to that during the cooling period that leads to a linear Zeeman shift of the $\Delta m = 1$ component of the quadrupole transition of 4.60(2) MHz. Under this condition, the quadratic Zeeman shift on the octupole transition is found to be 661(5) Hz using an H-Maser as the reference. For the octupole transition, the effect of light shift is canceled by linear extrapolation to zero intensity and the observed Zeeman splitting frequency of 4.60(2) MHz includes a correction for its quadratic contribution of -14 kHz. The huge uncertainty in the linear Zeeman frequency results from the instability of the magnetic field and could easily be reduced by a few orders of magnitude.

It is convenient to express the sensitivity to the second-order Zeeman shift in terms of the $\Delta m_F = 1$ component of the quadrupole transition: $\Delta\nu_{Z1}(^2D, 3/2, 2, 1)$, as it is the directly observable measure for the magnetic flux density. Following this idea, the measured sensitivity of the octupole transition is $-28.8(3)$ pHz $\Delta\nu_{Z1}^{-2}(^2D, 3/2, 2, 1)$ and can be translated to -2.03(2) mHz/μT^2. This result is in good agreement with the value calculated with the measured hyperfine splitting frequencies and does not agree with the last published value [126].

In a similar measurement with a smaller instability of the magnetic field, the quadratic Zeeman shift coefficient for the quadrupole transition was determined to be 0.740(2) nHz/$\Delta\nu_{Z1}^2(^2\mathrm{D}, 3/2, 2, 1)$. The result shows very good agreement with 0.7404(3) nHz/$\Delta\nu_{Z1}^2(^2\mathrm{D}, 3/2, 2, 1)$ inferred from hyperfine splittings and the precise g-factors [121].

For the operation as a frequency standard, the constancy of $\Delta\nu_{Z1}(^2\mathrm{D}, 3/2, 2, 1) =$ 30 kHz is assumed to be better than 100 Hz over many days of operation, which was verified by repeated measurements over such a period. This instability dominates the uncertainty of the quadratic Zeeman shift on the quadrupole transition and is a minor contribution for the octupole transition. With the measured sensitivity, the relative shift of the octupole transition frequency due to the quadratic Zeeman effect is $-40.4(6) \times 10^{-18}$.

Magnetic fields from the environment are well suppressed by the μ-metal shielding. Quadratic Zeeman shifts could arise from RF currents of the trap drive. However, the low drive power and the high symmetry of our trap and its supply lines result in an expected RMS field that is well below the uncertainty of the applied magnetic field.

3.5 Background gas collisions

As the ion trap is operated in a vacuum chamber of limited quality, collisions with background gas molecules occur. It seems that so far no experimental investigation on frequency shifts induced by background gas collisions for optical frequency standards with single ions has been performed. For frequency standards based on transitions in the microwave range, however, this effect has been investigated for many different systems showing different sensitivities of the transition frequency. For the hyperfine transition of Ba^+ and Hg^+ very similar fractional frequency shifts due to He background gas of 5×10^{-11}/Pa and 4.3×10^{-11}/Pa have been observed [127,128]. For the hyperfine transition of the ground state of trapped $^{171}Yb^+$ ions, the He background gas shift has been evaluated as 1.3×10^{-9}/Pa [129], which is very close to the result for neutral caesium 1.1×10^{-11}/Pa. A surprisingly large shift of -3×10^{-6}/Pa has been observed for Be^+ [130]. The results for Yb^+ and Be^+ were not predicted by a theoretical approach given in Ref. [127]. It furthermore seems to be very difficult to translate results obtained for microwave transitions to that of optical transitions.

A different approach has been followed in Ref. [26], here the frequency shift is estimated assuming sudden changes of the atomic phase during the interrogation. It is assumed that each collision results in a phase change of $\pi/2$, which maximizes the frequency shift. For Rabi interrogation a frequency shift of $0.15k$, where k is the collision rate in hertz, is obtained by numerical integration of the optical Bloch equations and is independent of the interrogation time and the duty cycle [26].

This result is valid for interrogation with Rabi pulses, but very similar for Ramsey or "hyper-Ramsey" spectroscopy.

Following this approach requires an estimate on the collision rate $k = n\langle v\rangle\sigma$, where $\langle v\rangle$ is the mean speed of the background gas molecules, n is the number density and $\sigma = 2\pi d$ is the collision cross section. Here, $d = 10\ \mathrm{a_0} = 0.53$ nm can be assumed from theoretical investigations of Yb and He that is the dominant background gas constituent due to the glass vacuum chamber [131]. The number density is calculated as $p/(k_B T)$, where p is the pressure, k_B is Boltzmann's constant and T is the temperature. In this way, a rate of about 3 mHz is determined resulting in a shift of 0.4 mHz at a He pressure of 10^{-8} Pa at room temperature. At approximately the deduced collision rate, short drops of the fluorescence rate are observed. For operation as a frequency standard, these events can be selected and excluded based on the level of fluorescence signal in the state detection and subsequent cooling period. Up to now, this method is not implemented, and therefore an uncertainty of 0.4 mHz is assumed for both optical frequency standards.

3.6 Doppler shifts due to optical path length fluctuations

In this and the next section shifts of the optical frequency standard are discussed that do not result from variations of the atomic frequency reference directly, but are related with the measurement process and the experimental setup. As pointed out at the beginning of this chapter, variations of the distance between the ion and the point at which the frequency is detected can result in significant first and second-order Doppler shifts. The probe laser light is brought via single-mode polarization maintaining optical fiber to the optical table on which the ion trap and the slave laser are installed. To reduce variations of the optical path length from the probe laser system to the ion trap and to the frequency comb, path length stabilizations based on an integrating servo systems have been installed that use AOMs to steer the optical frequencies [132]. The remaining unstabilized path length on the optical table before the trap is about 2.5 m and the beam is guided in tubes to prevent air turbulence. A measurement of the variation of the temperature and air pressure in the laboratory indicated that no relative frequency uncertainties larger than 3×10^{-19} can be expected.

Another first-order Doppler shift can result from a displacement of the ion in the trap due to photo-induced patch fields, especially in case of spectroscopy on the octupole transition with high probe laser intensities. Most of the effect is expected to decay with a long time constant as observed in Ref. [133]. In our experiment, however, no significant changes of the compensation voltages have been observed, after probe pulses with high intensity were applied. Therefore no related frequency

shifts are expected. On a short timescale, patch charges might be present during the interrogation and lead to a Doppler shift of the frequency observed in the reference frame of the ion at the beginning of the interrogation period. Under the assumption that such fields build up and decay very rapidly, they appear in parts of the interrogation where the frequency sensitivity is relatively small [134]. If the "hyper-Ramsey" technique is applied, a possible frequency shift is well suppressed, since it would occur in both Ramsey pulses with comparable magnitude.

3.7 Gravitational Red Shift

The comparison of clocks at different positions in the gravitational potential, requires a correction $\Delta\nu_G/\nu_0 = -(\phi - \phi_0)/c^2$ if a frequency signal emitted at a gravitational potential ϕ is used for the comparison at ϕ_0 [135]. This is a direct consequence of the equivalence principle and the predicted shift has been verified to agree with the theoretical prediction within 7×10^{-5} [136]. For clocks not too far apart from each other on the surface of the earth, the correction can be simplified under the assumption of a small height difference $\Delta h = h - h_0$ using the local acceleration of gravity g to be $\Delta\nu_G/\nu_0 = -g\Delta h/c^2$. For comparisons of clocks at large distances, the geoid is used as the reference surface, however, different models for the geoid exist and the calculated gravitational potential causes an uncertainty of the correction of $\approx 3 \times 10^{-17}$ [137]. This can be a limiting factor if clocks with even smaller systematic uncertainty should be compared internationally.

If the agreement between two clocks has been established, the gravitational red shift can be used to probe the gravitational potential, but the precise detection of differences in the gravitational potential requires a stable and accurate frequency link between the two setups [138]. So far, only one experiment has demonstrated a measurement of the difference of the gravitational potential between two clocks in one building with an uncertainty comparable to that occurring due to established techniques in intercontinental clock comparisons [139].

3.8 AOM Chirp

In the so far unstabilized optical path of the octupole probe laser light an acousto-optic modulator (AOM) is installed for pulsing. Switching off the radio-frequency drive signal can induce excursions of the optical phase that occur on different time scales. At the very beginning and the end of a pulse, phase excursions for much less than 1 μs have been observed [140]. In our case, the contribution of these phase excursions is expected to be negligibly small due to the interrogation with much longer Rabi pulses. For the octupole transition, the "hyper-Ramsey" method suppresses this shift effect similar to the light shift as it appears with

comparable magnitude in both Ramsey pulses (see chapter 4). Beside these fast damping phase excursions, the temperature variation of the TeO_2 crystal changes its length and the optical density. To detect the frequency chirp, light after the 1.9 mm long crystal was analyzed by optical heterodyne detection, where a fraction of the probe laser light that did not pass the AOM serves as the local oscillator. By simultaneously detecting the beat frequency together with the temperature of the AOM's crystal, an agreement between the observed frequency chirp and the expected frequency shift based on tabulated values for TeO_2 and the measured temperature rise (see Fig. 3.11) has been found. Due to the size of the frequency shift, more precise evaluation is expected from the temperature measurement. The fractional frequency shift induced by a temperature rise $\Delta T/\tau$ is:

$$\frac{\Delta\nu}{\nu_0} = -\left(\frac{\Delta n}{\Delta T} + \alpha_L\right)\frac{\Delta T \cdot l}{\tau \cdot c}, \tag{3.27}$$

where l is the length of the crystal, c denotes the speed of light and the thermal expansion $\alpha_L(TeO_2) = 9 \times 10^{-6}$ and the thermal induced change of the refraction index $\Delta n/(\Delta T) = 9 \times 10^{-5}$ [141]. The measurement shown in Fig. 3.11 performed at maximum RF signal after a long dark period leads to a frequency shift of -8.0×10^{-16} and a linear scaling of the induced frequency shift with the applied power is expected. Since the shift also scales as $(1\text{-}T_{on}/T_{total})$ with the duty cycle of the AOM T_{on}/T_{total}, the AOM drive power remains switched on for 95% of the time. The drive power is only switched to create precisely defined pulse edges, and a mechanical shutter blocks the probe laser light during most of the dark periods. For the quadrupole transition the RF drive power is strongly reduced by more than 20 dB. For the octupole transition, the drive power is reduced by only 10 dB, but the shift effect is suppressed with the "hyper-Ramsey" method or the light shift extrapolation scheme, where the light shift is canceled by real-time extrapolation from two settings of the optical power to zero. Since the optical power is adjusted by linearly changing drive power, which determines the temperature rise, a significant suppression can be expected also for the AOM chirp. In the "hyper-Ramsey" scheme all shift effects are suppressed that occur similarly in both Ramsey pulses as discussed in section 4.1. The suppression is improved by the controlled "hyper-Ramsey" scheme, where shifts are canceled that occur also during interleaved Rabi spectroscopy (see section 4.3). In this way, spurious variations of the optical phase induced by temperature changes of the AOM crystal simultaneous with the probe cycle are well suppressed, and the corresponding relative uncertainty for the octupole frequency standard is only 3×10^{-19}.

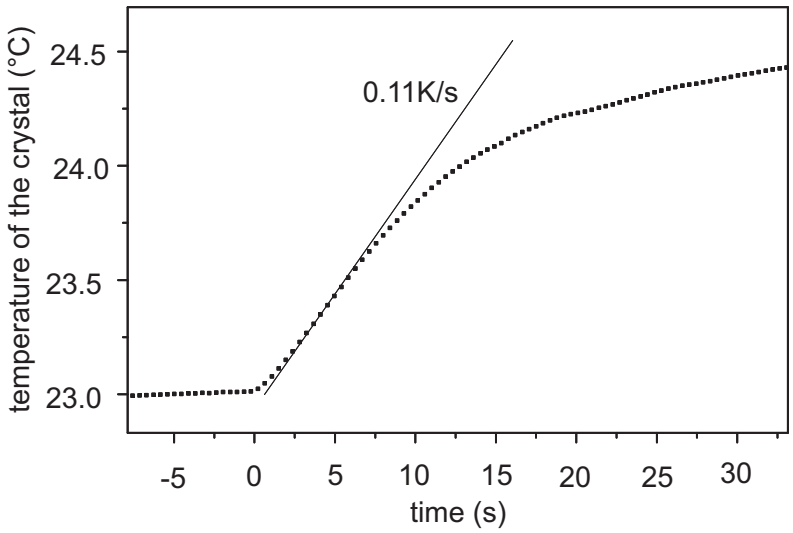

Figure 3.11: Temperature of the TeO_2 crystal of the acousto-optic modulator used in the experiment to create defined edges of the probe laser pulses. The measurement is performed by switching on the drive voltage at 0 s after a long off-period, so that the crystal temperature was close to room temperature. The applied RF drive power of 1 W is reduced under normal operation conditions by at least 10 dB.

3.9 Servo Error

A frequency shift between the probe laser that serves as the local oscillator of the frequency standard and the atomic resonance can occur due to insufficient compensation of frequency drifts of the probe laser. As discussed in section 2.5, the servo system corrects for the creep of the optical cavity by steering a linear frequency drift to the acousto-optic modulator in front of the cavity. The frequency drift is corrected every 10 s by the mean error signal since the last update times a gain factor [102]. Ideally the second-order integrator should cancel a possible servo error. A maximum servo error can be calculated using the gain factor, the maximum drift variation of the probe laser system and the cycle time [28]. This maximum deviation is in the 10^{-17} range for both optical frequency standards, however, it would only be valid for a period of a constant maximum change of the drift rate, which is certainly not the case. The expected uncertainty contribution due to nonlinear frequency drifts of the probe laser system has thus to be evaluated for each measurement taking into account the applied frequency corrections and the relative interrogation time. For all measurements with averaging times of several thousand seconds, the related uncertainty is not a significant contribution to the total systematic uncertainty.

3.10 Conclusion – Comparison of the E2 and E3 Frequency Shift Effects

The leading shift effects for each of the two optical frequency standards of $^{171}Yb^{+}$ are listed in Tab. 3.3. For both realizations, the dominating uncertainty is connected with the thermal radiation that affects the ion.

Effect	E2 transition		E3 transition	
	$\delta\nu/\nu_0(10^{-18})$	$u/\nu_0(10^{-18})$	$\delta\nu/\nu_0(10^{-18})$	$u/\nu_0(10^{-18})$
Blackbody radiation shift	-524	102	−70.7	2.6
Second-order Doppler	-3	2	−3.7	2.1
Light shift	0.0	1	0	1.5
Quadratic dc Stark	-7	4	−1.2	0.6
Quadrupole shift	0	14	0	0.3
Quadratic Zeeman shift	968	7	−40.4	0.6
Collisional shift	0	1	0	0.6
Path length instabilities	0	0.3	0	0.3
AOM chirp	0	8	0	0.3
Servo error	0	36	0	0.5
Total	434	110	−116.0	3.9

Table 3.3: Leading fractional frequency shift $\delta\nu/\nu_0$ effects and the related relative uncertainty u/ν_0 for an optical frequency standard with a single Yb^{+} ion based on the quadruple (E2) and octupole (E3) transition. For the E2 transition Rabi spectroscopy and for the E3 transition controlled "hyper-Ramsey" spectroscopy is used.

4 “Hyper-Ramsey” Spectroscopy

This chapter discusses the so-called “hyper-Ramsey” spectroscopy (HRS), an excitation scheme that enables light shift free spectroscopy of strongly forbidden transitions and suppresses shift effects that appear synchronously with the interrogation pulses, e.g. the AOM chirp. At first a short introduction and a theoretical description of the technique are given. In the second section, spectroscopic results obtained on the octupole transition are presented and the last section discusses the application of the method in an optical frequency standard, and a technique to measure the compensated shifts and ensure an efficient cancellation.

4.1 Introduction and theoretical description

Intended as a technological advantage in the early magnetic-resonance experiments with molecular beams, Ramsey's method of separated oscillatory fields was crucial for the progress in precision spectroscopy and the development of atomic clocks [142], and is an important tool in quantum information processing [143]. His basic idea was to replace the single long region, in which the atoms are interrogated with an oscillating field (Rabi method), by two short ones at the beginning and the end of the interaction zone. As a result, the two levels of the investigated quantum system are brought into a coherent superposition with the first interrogation followed by a free evolution period. After the second interrogation the population in the levels is detected, which show the effect of the interference of the second pulse with the time-evolved superposition states. In the original experiments with atomic and molecular beams this permitted the recording of a resonance lineshape with a width that is mainly determined by the total interaction time, without shifts and broadening through inhomogeneous excitation conditions. Ramsey's method is employed mainly to excite states with a natural lifetime exceeding the interaction time, so that primarily transitions forbidden by electric dipole selection rules are investigated. The advent of laser-cooled trapped ions and atoms led to a tremendous increase in the temporal separation of the two Ramsey interactions. For the microwave transition between the hyperfine components of the ground state of trapped $^{171}Yb^{+}$ ions, coherence times up to 10 minutes have been observed [144]. On an optical transition, the longest observed coherence between two Al^{+} ions of a few seconds was essentially limited by the natural lifetime of the excited states [145]. To overcome this limitation, states with longer lifetimes

are of particular interest, e.g. the $^2F_{7/2}$ state of Yb^+. However, the high probe light intensities required for excitation of these states will unavoidably lead to level shifts through the dynamical Stark effect. Beside the octupole transition discussed here, a wide range of precise frequency measurements presently suffer from significant uncertainties due to light shift. Here, two-photon [146–149], and magnetic-field induced transitions [150–153] are good examples.

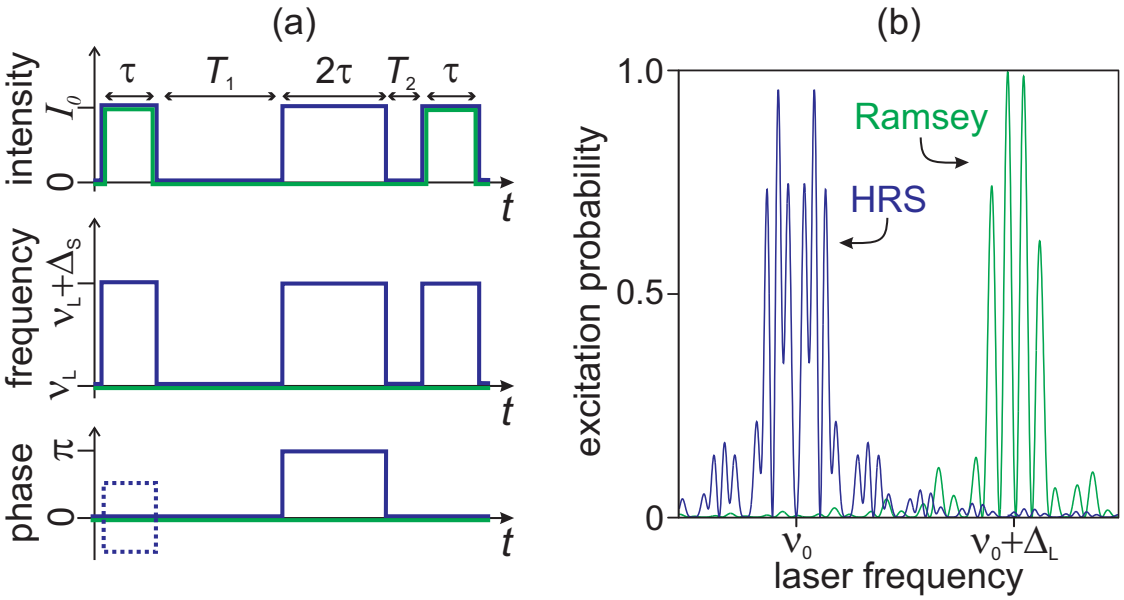

Figure 4.1: Pulse sequence (a) and resulting excitation spectrum (b) of the Ramsey (green) and the "hyper-Ramsey" spectroscopy (HRS) excitation scheme (blue). Here ν_L is the probe laser frequency and ν_0 the unperturbed transition frequency. The laser step frequency Δ_S is assumed to be equal to the light shift Δ_L and the intensity I_0 is chosen to obtain a pulse area $\pi/2$ for a pulse duration τ. A discriminator signal can be generated by alternately stepping the phase of the first pulse by $\pm\pi/2$ as indicated by the dotted lines. The spectra are calculated for the parameters $T_1 = 2\tau$, $T_2 = 0$, $\Delta_L = 4.1/\tau$ with equal dark period durations in both schemes.

This problem is approached in the HRS method proposed by Yudin *et al.*, that can be understood as a further development to the Ramsey technique [154]. The spectrum obtained with Ramsey excitation usually shows indications of the presence of light shift: the position and shape of the envelope reflects the excitation spectrum resulting from one of the pulses, whereas the Ramsey fringes result from coherent excitation with both pulses and the intermediate dark period. The fringes are less shifted than the envelope, because their shift is determined by the time average of the intensity. This results in a shifted and asymmetric Ramsey pattern [see

Fig. 4.1(b)], as observed in early demonstrations of optical Ramsey spectroscopy of a two-photon transition [155].

This intuitive picture suggests that the effect of the light shift Δ_L on the spectrum can be compensated by introducing a frequency step of the probe light $\Delta_\mathrm{S} = \Delta_\mathrm{L}$ during the interrogation pulses whereas the unshifted probe frequency ν_L is tuned across the resonance with the unperturbed atomic frequency ν_0, as proposed in [156]. The scheme can be made additionally insensitive against small changes of the laser intensity or errors in Δ_S by inserting an additional pulse with identical intensity and frequency and with a doubled duration between the Ramsey pulses. This feature bears resemblance to "echo" techniques [157] which can be used to suppress dephasing between the atomic oscillators during the free evolution. Here, however, the additional pulse compensates the dephasing between the atomic coherence and the probe laser field caused by the Ramsey pulses. The phase of the additional pulse is shifted by π relative to the Ramsey pulses in order to improve the robustness against variations of the pulse area. The frequency steps are applied in a phase-coherent way so that they do not introduce additional phase changes of the probe field. These are the essential elements of the HRS scheme [154]. The corresponding probe pulse pattern is sketched in Fig. 4.1(a).

The resulting resonance signal is calculated by numerical integration of the optical Bloch equations [158], describing the equation of motion of the pseudospin vector $\rho(u, w, z)$ in the rotating frame extended regarding the light shift Δ_L:

$$\begin{aligned}
\dot{u}(t) &= -\left(\Delta - \Delta_\mathrm{L} z(t)\right) v(t) - \frac{\Gamma_2 + \Gamma_1}{2} \cdot u(t) \\
\dot{v}(t) &= \left(\Delta - \Delta_\mathrm{L} z(t)\right) u(t) + \sqrt{z(t)}\Omega_0 w(t) - \frac{\Gamma_2 + \Gamma_1}{2} \cdot v(t) \\
\dot{w}(t) &= -\sqrt{z(t)}\Omega_0 v(t) - \Gamma_1 (w(t) + 1) \\
\dot{z}(t) &= \frac{d(I(t)/I_0)}{dt},
\end{aligned} \tag{4.1}$$

where $\Delta = \omega_0 - \omega_\mathrm{L}$ is the difference between resonant and the probe laser frequency. The intensity of the laser is described by z and the longitudinal decay rate Γ_1 due to a limited lifetime of the excited state can be assumed to be equal to zero for the octupole transition. The transversal decay rate that describes the loss of coherence is denoted with Γ_2. The excitation probability for a given time is equal to $(w(t) + 1)/2$. The relative optical phase during each pulse in the representation used in Eq. 4.1 is adjusted by the sign of the resonant Rabi frequency Ω_0 for $\pm\pi$ and the detuning δ during the dark period to achieve the relative phase of $\pm\pi/2$.

As shown in Fig. 4.1(a) the total dark period T can be divided into two parts, $T = T_1 + T_2$. The width of the central fringe is minimal for either $T_1 = 0$ or $T_2 = 0$. Introducing two dark periods may be technically advantageous because in this case both phase reversals can be carried out when the probe light is switched

off, which excludes the possibility that the phase reversal leads to transient pulse distortions [140]. For simplicity, the case $T_2 = 0$ will be assumed in the following and has been used in all experiments so far. The geometrical representation of Eq. 4.1 for the HRS sequence is shown in Fig. 4.2.

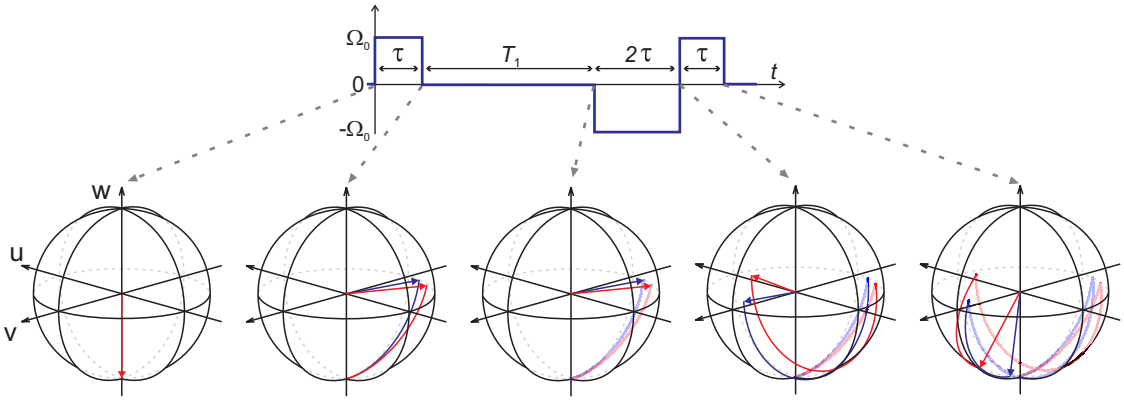

Figure 4.2: Geometrical representation for the interrogation with the HRS method. Blue arrows indicate the result for a small light shift Δ_L. For the red arrows a light shift of $2\Delta_L$ is assumed. The effect of the light shift in the first probe pulse is partly compensated by the light shift present in the second pulse.

Typical spectra calculated for the Ramsey and the HRS schemes are shown in Fig. 4.1(b). The remarkable result of the theoretical analysis [154] is that the linear dependence of the frequency corresponding to the central minimum of the HRS resonance signal on an error in the compensation frequency Δ_S can be eliminated over a range proportional to Ω_0. The immunity against an uncompensated light shift $\Delta_L - \Delta_S$ is illustrated in Fig. 4.3 by comparing the spectral dependence of the excitation probability for the Ramsey and HRS pulse sequences. For this comparison, a frequency step $\Delta_S \neq 0$ during the pulses was also used for the Ramsey case as in Ref. [156]. Here the fringe pattern position depends linearly on the residual light shift $\Delta_L - \Delta_S$ with a slope of $(1 + \pi T/4\tau)^{-1}$. In contrast to this, the HRS excitation shows a distinctly nonlinear dependence, so that the frequency of the minimum excitation probability remains nearly constant in a wide interval around the perfect compensation condition $\Delta_S = \Delta_L$. Beyond that range the position of the HRS fringe pattern shifts with a slope that is larger than in the case of Ramsey excitation. The spectral resolution obtained with the HRS scheme is only slightly reduced compared to Ramsey or Rabi excitation with the same total interrogation time (see Fig. 4.4)

In an atomic frequency standard the frequency of an oscillator is stabilized to the line center of the atomic resonance signal. As discussed in section 2.5, this can be achieved by alternately recording resonance signals with a fixed positive and neg-

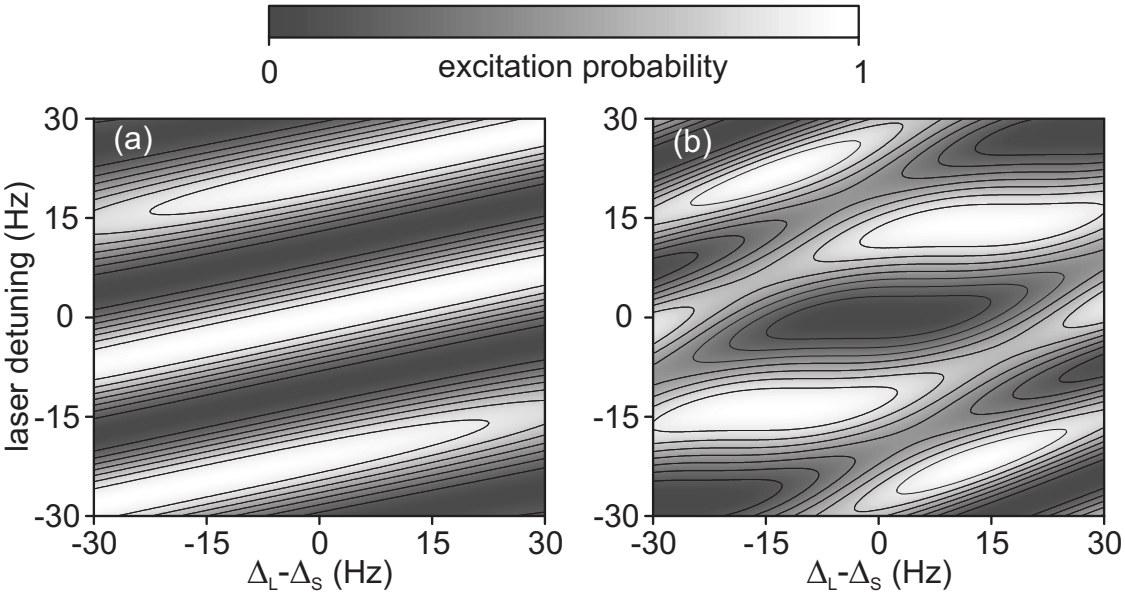

Figure 4.3: Calculated excitation probability as a function of the uncompensated light shift $\Delta_L - \Delta_S$ and of the laser detuning $\Delta\nu_0$ from the unperturbed transition frequency for (a) Ramsey and (b) HRS excitation. In accordance with typical parameters of the performed experiment, the duration of the $\pi/2$-pulse is $\tau = 9$ ms and that of the dark period $T = 36$ ms. For this comparison, a frequency step $\Delta_S \neq 0$ during the pulses was also used for the Ramsey case as in Ref. [156]

ative detuning around the line center. For the Ramsey excitation, a discriminator signal can also be produced by alternately applying phase steps of $\phi = \pm\pi/2$ to one of the excitation pulses while the excitation frequency is kept constant [159, 160]. If applied to the HRS excitation scheme as shown in Fig. 4.1(a), the latter technique is particularly advantageous because the immunity to light shift fluctuations is further enhanced (see below).

4.2 Spectroscopy of the Yb^+ Octupole Transition using the HRS Method

For the experimental investigation, the HRS pulse sequence is shaped by the acousto-optic modulator (AOM) in front of the ion trap. The drive frequency of 76 MHz is generated by a direct digital synthesizer, which enables fast and precise control of the intensity, frequency, and phase of the probe light field. The laser frequency was tracked with the fiber-laser based frequency comb generator using the caesium fountain clock CSF1 as the reference. The light shift Δ_L is determined

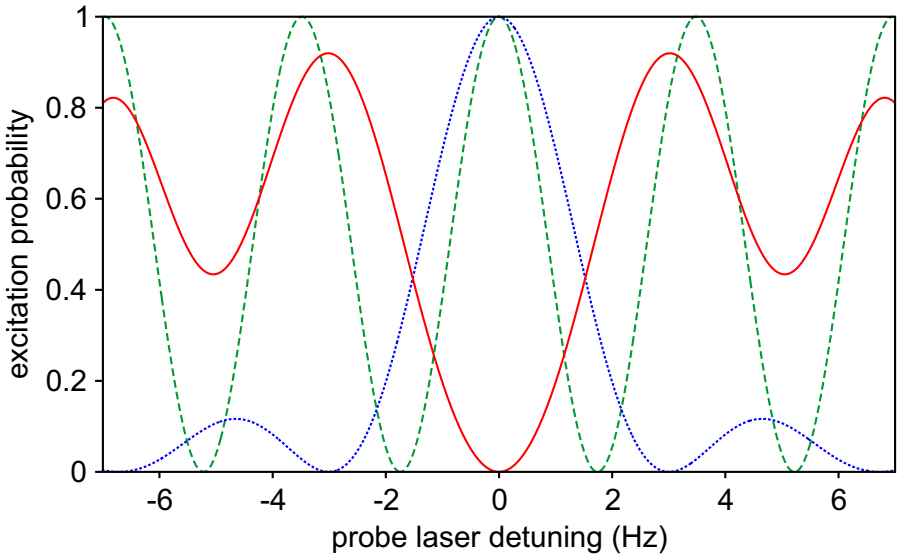

Figure 4.4: Comparison of the central feature of resonance spectra of a two-level system for a fixed interrogation time of 288 ms. The blue line shows the excitation probability for Rabi excitation with a single 288 ms long pulse, the result for Ramsey interaction with 1 ms long pulses and 286 ms free evolution period is shown as the green dotted line, and the result for the HRS method with $\tau = 36$ ms, $T_1 = 144$ ms, and $T_2 = 0$ ms is indicated by the solid red line. The linewidth (FWHM) of the central HRS fringe is with 3.2 Hz slightly larger compared to Rabi (2.8 Hz) and Ramsey (1.7 Hz) excitation.

by stabilizing the laser frequency to the resonance signal obtained with Rabi excitation and comparing it to the unperturbed transition frequency, that has been measured with the real-time extrapolation technique (see section 3.2.4).

Figure 4.5 shows experimental spectra obtained with the HRS scheme together with the calculated fringe patterns for full light shift compensation ($\Delta_L = \Delta_S$) and for the case $\Delta_L - \Delta_S = 10$ Hz, with a light shift $\Delta_L = 1090$ Hz in both cases. From a comparison of recorded spectra with calculated lineshapes, $\Delta_L - \Delta_S$ was determined with an uncertainty of 1 Hz. The scattering of the measured excitation probabilities is predominantly determined by quantum projection noise. Comparing the two cases, large differences appear in the shape of the excitation spectrum except for the position of the central minimum which is largely unaffected.

The predicted nonlinear dependence of the stabilized probe laser frequency on the uncompensated light shift $\Delta_L - \Delta_S$ will be experimentally investigated in the following. Therefore, the discriminator signal for stabilization to the atomic resonance is generated by alternately stepping the phase of the first probe light pulse by $\pm\pi/2$ as described above. With the interleaved servo technique the probe light

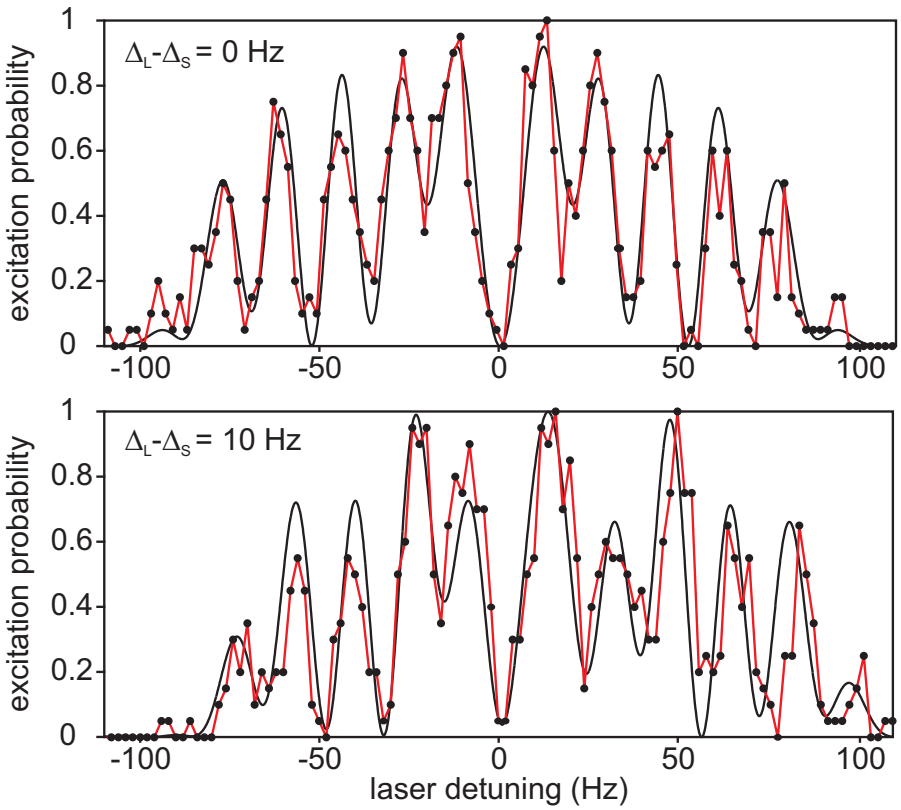

Figure 4.5: Excitation spectra of the octupole transition in $^{171}Yb^{+}$ using the HRS scheme with $\tau = 9$ ms and $T = 36$ ms with fully ($\Delta_L = \Delta_S$) and partially ($\Delta_L \neq \Delta_S$) compensated light shift for $\Delta_L \approx 1$ kHz. The laser detuning is relative to the unperturbed transition frequency and the data points are the result of 20 interrogations at each frequency step. The solid black lines show the calculated line shapes.

frequency is stabilized for different settings of Δ_S. In this way, the frequency offset resulting from a variation of Δ_S relative to the case of complete light shift compensation, $\Delta_L = \Delta_S$ can be determined. The magnitude of the light shift Δ_L is inferred from the resonant frequency using Rabi excitation measured against the ceasium fountain clock CSF1 and the known unperturbed transition frequency. The result of these measurements is presented in Fig. 4.6. Here, the duration of the probe pulse is reduced to the limit given by the maximal available probe light intensity and the experimental results are in very good agreement with the calculated dependence which is predominantly cubic around $\Delta_S = \Delta_L$. Also shown in Fig. 4.6 is the predicted dependence of the central minimum of the HRS spectrum on the residual light shift. The comparison of the two calculated curves with the experimental data confirms the superior light shift suppression that is obtained

if the laser frequency is stabilized by a discriminator signal produced by phase steps of $\phi = \pm\pi/2$ of the first excitation pulse [154]. Beside this theoretical advantage, it should be noted that a stabilization to the central minimum based on frequency stepping leads to experimental difficulties and uncertainties due to the strong asymmetry of the central fringe for $\Delta_L \neq \Delta_S$ (see Fig. 4.5).

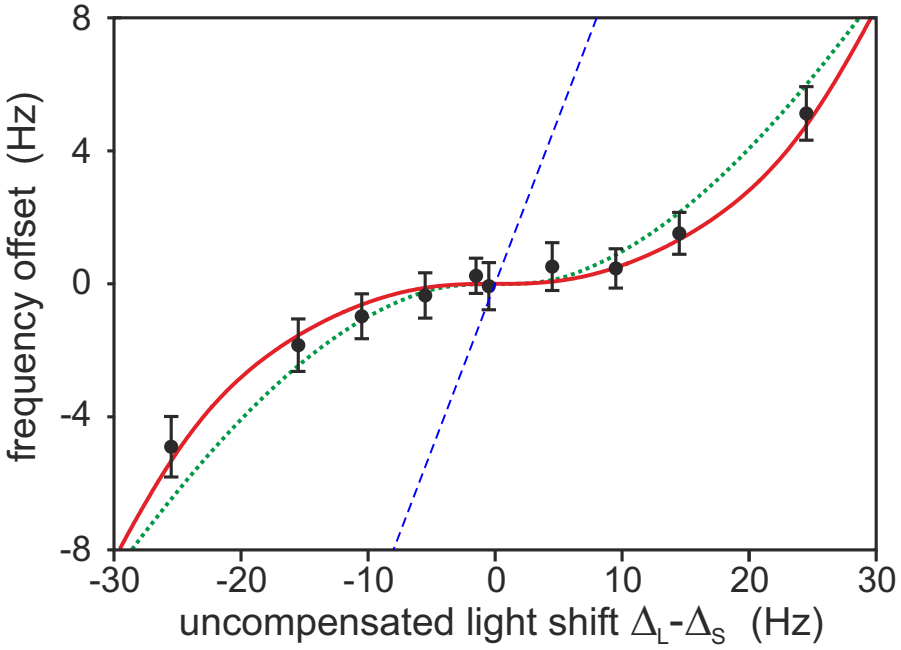

Figure 4.6: Frequency offset of the probe laser stabilized at $\Delta_L - \Delta_S$ relative to the fully compensated case $\Delta_S = \Delta_L$, for $T = 36$ ms, $\tau = 9$ ms and $\Delta_L = 1090$ Hz. The solid red line indicates the predicted dependence if the discriminator signal of the stabilization is generated by alternately stepping the phase of the initial pulse by $\pm\pi/2$. The dotted line shows the position of the central minimum of the HRS spectrum and the dashed line shows the dependence of the center frequency of a single pulse Rabi pattern obtained at the same intensity if the probe laser frequency is stepped by Δ_S during the interrogation.

Since the light shift Δ_L scales quadratically with the Rabi frequency Ω_0, and the range of efficient suppression is limited to $|\Delta_L - \Delta_S| < \Omega_0$, the relative range $|\Delta_L - \Delta_S|/\Delta_L$ increases if Ω_0 is reduced. Following this idea, Figure 4.7 shows the frequency shift induced by uncompensated light shift when the probe pulse duration is extended to near the coherence time of the probe laser. The results are again in good agreement with the calculated dependence, but a residual linear dependence on the uncompensated light shift might loom up. Such a residual linear dependence can be induced by incoherence or a reduction of the pulse area

in the second Ramsey and the "echo" pulse due to motional heating of the trapped ion. Therefore, it can be advantageous to apply the "echo" pulse before the free evolution period. In this way most of the additional linear dependence induced by the pulse area variation can be avoided. Limitations of the HRS method related with frequency noise of the probe laser or spontaneous decay are also addressed in Ref. [161]. Unfortunately, this reference contains a mistake; in Fig. 7 the line describing small incoherence is accidentally shifted [162]. To make it clear, in all discussed cases no frequency offset remains if the light shift is fully compensated by the step frequency ($\Delta_L = \Delta_S$).

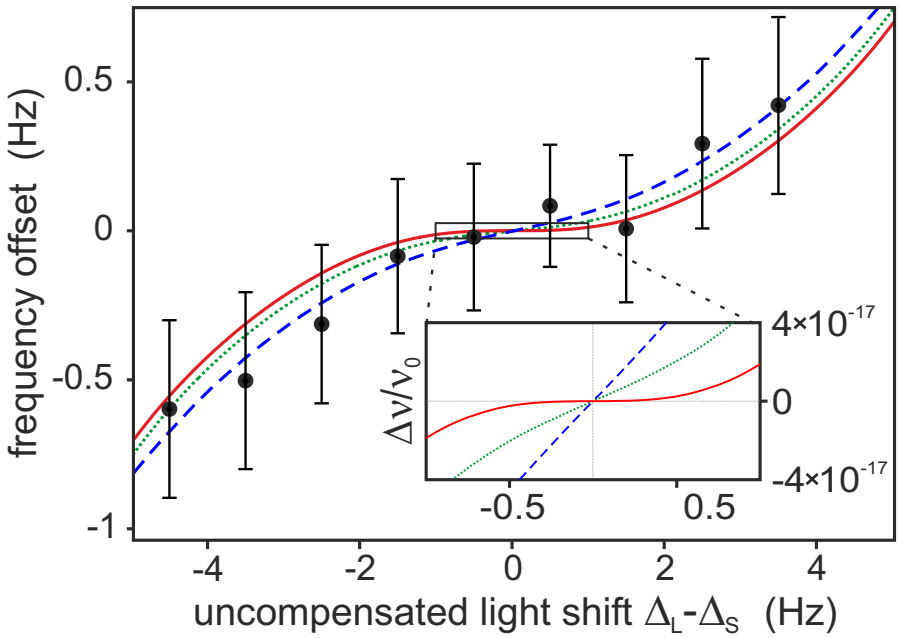

Figure 4.7: Frequency offset of the probe laser stabilized at $\Delta_L - \Delta_S$ relative to the fully compensated case $\Delta_S = \Delta_L$, for $\Delta_L = 60.5$ Hz, $T = 144$ ms and $\tau = 36$ ms, corresponding to a linewidth of the central HRS fringe of 3.2 Hz. The solid red line indicates the predicted dependence if the discriminator signal of the stabilization is generated by alternately stepping the phase of the initial pulse by $\pm\pi/2$. The calculation of the dotted line assumes the same technique, but also the limited coherence time of our probe laser ($\Gamma_2 = 1.5\ s^{-1}$). For the dashed line additionally motional heating of the ion is considered that reduces the pulse area during the last pulse by 10%. The inset is an enlarged view showing the frequency offset in units of the frequency ν_0 of the Yb^+ octupole transition.

4.3 Application of the HRS Method in an Optical Frequency Standard

The extraordinary advantage of the HRS method to suppress the light shift requires *a priori* knowledge of its magnitude. Although this can be achieved by light shift extrapolation, slow variations of Δ_{L} during the operation as a frequency standard can degrade the compensation. Furthermore, even if the mismatch is comparably small, decoherence and residual thermal motion of the ion can reduce the suppression efficiency. To avoid such limitations, the step frequency needs to be adjusted to the light shift in real time. In order to steer the step frequency, a stabilization using the HRS scheme is combined with a second servo system where Rabi spectroscopy with the same probe light intensity is performed. In this way the frequency offset $\nu_{\mathrm{Rabi}} - \nu_{\mathrm{HRS}}$ between the different excitation techniques is determined using the interleaved servo technique that was discussed before. The dependence on uncompensated light shift for both excitation schemes is sketched in Fig. 4.6 and is significantly larger for Rabi spectroscopy. Therefore, $\nu_{\mathrm{Rabi}} - \nu_{\mathrm{HRS}}$ is a sensitive measure for uncompensated light shift and can be used in a negative feedback loop to control the step frequency Δ_{S}.

The required gain of the feedback loop depends on the constancy of the light shift. In our case, slow relative variations of the light shift of less than 1%/h are typically observed. They predominantly result from pointing drifts and from a residual dependence of the optical power of the probe laser radiation at 467 nm on the ambient temperature. In a first test of this controlled HRS technique, the interleaved stabilization switched between the excitation methods after every fourth interrogation, so that 50% of the total measurement time are used for the light shift measurement. Due to the construction of the software that controls the experiment, the cycle time was equal in both modes. The frequency difference between the two modes was recorded every 10 s and 5% of the value were subtracted from Δ_S. Figure 4.8 shows a recording of the controlled step frequency, which approximates the light shift at the ion, and the frequency offset measured between the two servo systems. Here, the parameters $T = 122$ ms and $2\tau = 61$ ms were chosen and the orientation of the magnetic field was adjusted to permit similar excitation probability of the octupole transition with a comparable light shift for two mutually orthogonal directions.

To investigate the effect and the quality of the light shift control loop, the Allan variance of the frequency offset, is plotted in Fig. 4.9. The frequency instability is significantly below 1 Hz and decreases from a few 100 s on linearly with the integration time reaching the 26 mHz level after $\approx 10^4$ seconds. This clearly shows the operation of the servo system, so that the formerly purely systematic uncertainty of the light shift becomes a mainly statistical uncertainty.

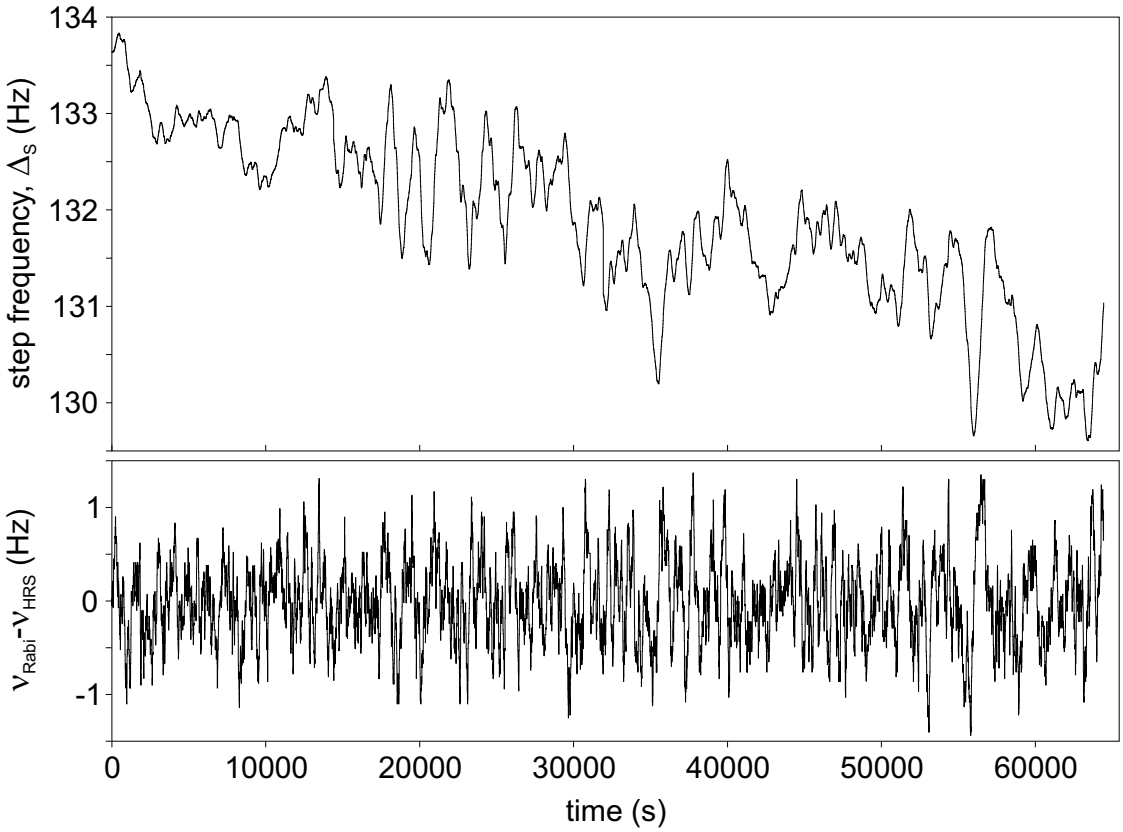

Figure 4.8: Frequency step Δ_S of the controlled HRS method versus the operation time of the frequency standard. The frequency step is controlled to compensate the light shift in the HRS method and for Rabi spectroscopy using the frequency difference $(\nu_{\mathrm{HRS}} - \nu_{\mathrm{Rabi}})$.

As discussed above, the frequency shift observed with the HRS method can have a residual linear dependence on the uncompensated light shift if motional heating and a limited coherence time of the probe laser frequency are taken into account. For $|\Delta_{\mathrm{L}} - \Delta_{\mathrm{S}}| \ll \Omega_0$ this linear contribution dominates, but the frequency shift for HRS is at least 15 times smaller than for the Rabi spectroscopy with the parameters of the present status of the experiment. Hence, the observed instability of 26 mHz for an averaging time of about 10^4 s (see Fig. 4.9) leads to a fractional frequency uncertainty of 2.7×10^{-18}. This constitutes a shift suppression by nearly five orders of magnitude and is, however, a rather conservative estimate, since the step frequency control loop operates the entire measurement time, so that the observed instability could be extrapolated to the total measurement time. Depending on the expected total measurement time and the instability of the light shift, the duty cycle of the operation with the HRS method can be increased. This reduces the long-term frequency instability of the frequency standard, but increases the

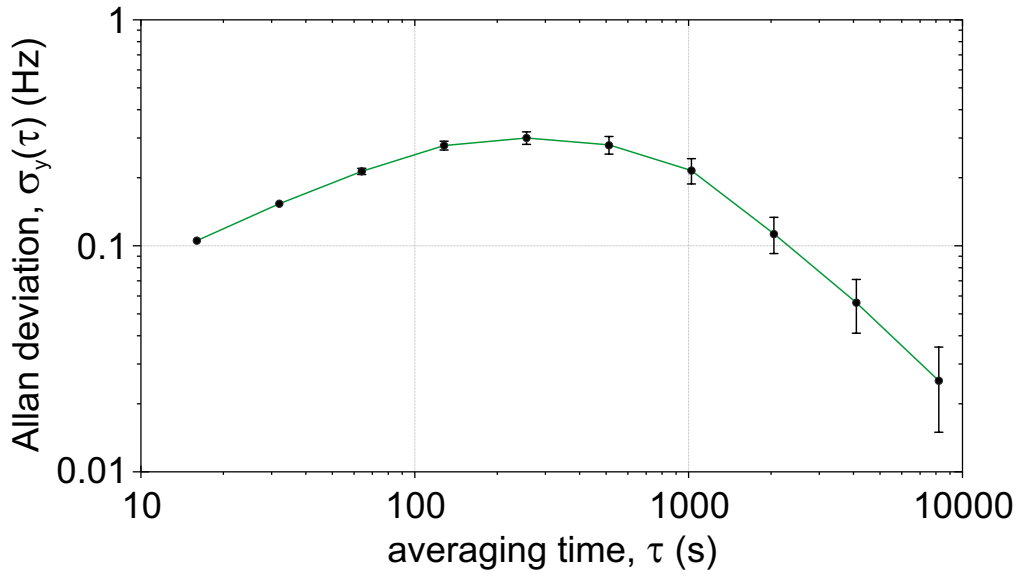

Figure 4.9: Allan deviation $\sigma_y(\tau)$ of the frequency difference $(\nu_{\mathrm{HRS}} - \nu_{\mathrm{Rabi}})$ versus the averaging time τ. The line is a guide to the eyes.

instability of the frequency offset. A too large instability of frequency offset can certainly limit the light shift cancellation, but tests of operation with HRS duty cycles of 66% and 75% did not show significant increase of the systematic uncertainty if long continuous measurements are performed.

To summarize, the controlled HRS method permits efficient elimination of the probe laser induced light shift and any transition frequency shift which appears synchronously with the interaction with the probe light. Beside the AOM chirp, a well-known example for this is the Zeeman shift in optical frequency standards relying on magnetic-field induced transitions [150–153]. In contrast to extrapolation techniques this scheme does neither require precise intensity measurements nor information on the relation between intensity and shift.

5 Absolute Frequency Measurements

In this chapter measurements of the $^2S_{1/2}(F = 0) \rightarrow {}^2D_{3/2}(F = 2)$ and $^2S_{1/2}(F = 0) \rightarrow {}^2F_{7/2}(F = 3)$ transition frequency versus caesium fountain clocks will be discussed. The first section describes the optical frequency comb generator that was used to perform the measurements of the optical frequency with respect to a microwave reference. In the second section, two measurements of the transition frequency of the octupole transition will be discussed and the last section describes a similar measurement of the quadrupole transition frequency.

5.1 Measurement and comparison of optical frequencies

Optical frequency standards vastly benefit from the 4 to 5 orders of magnitude higher transition frequencies when compared to microwave references. Even though optical standards had been developed for many years, comparisons with other standards, especially the primary microwave reference, was very difficult. Such measurements were mainly based on harmonic frequency chains to bridge the spectral difference [163], and a phase-coherent measurement was particularly difficult, as it required simultaneous operation of several phase-locked loops [164]. The advent of the optical frequency comb generator at the beginning of the present century has changed this situation significantly, as it allows for phase-coherent measurements and comparisons of a wide range of optical frequencies with an accuracy comparable to that obtained in the microwave regime [165].

As shown in Fig. 5.1, the output of a mode-locked laser with a repetition rate f_{rep} of ultrashort pulses in the time domain can be interpreted as a comb in the frequency domain. The width of the comb spectrum is given by the inverse of the duration of a single pulse in the time domain. The frequency ν_n of the nth mode of the comb can be calculated as an integer number n times f_{rep} plus a constant frequency offset f_{CEO}, which arises due to the fact that the group and phase velocities inside the laser cavity are different and is related to the pulse-to-pulse carrier envelope offset $\Delta\phi$ in the time domain. While the repetition rate can be measured easily with a fast photodetector, a convenient measurement of f_{CEO}

requires the comb to span a full octave, i.e. the spectrum contains ν_n and ν_{2n}. In this case, f_{CEO} can be measured by heterodyne detection of $\nu_{2n} = 2nf_{\mathrm{rep}} + f_{\mathrm{CEO}}$ with the frequency doubled nth mode of the comb at $2\nu_n = 2nf_{\mathrm{rep}} + 2f_{\mathrm{CEO}}$. One way to operate the frequency comb is to stabilize f_{CEO} and f_{rep} to an accurate microwave reference, which in turn determines the frequency of each mode of the comb.

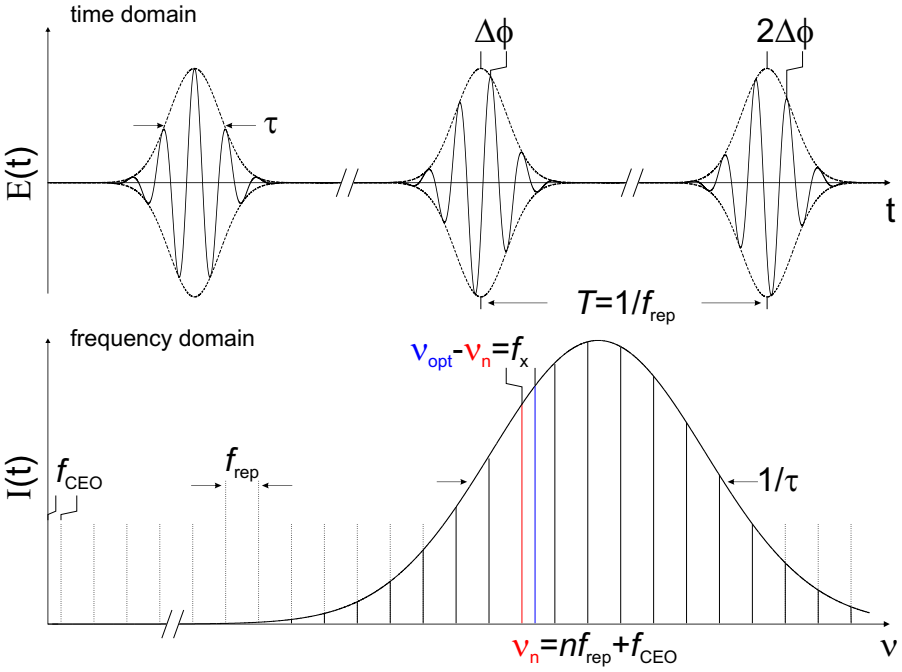

Figure 5.1: Output of a mode-locked ultrashort pulse laser in the time and frequency domain. In the time domain a pulse-to-pulse phase slip $\Delta\phi$ results from dispersion within the laser resonator and results in an offset frequency $f_{\mathrm{CEO}} = \Delta\phi/2\pi$. If f_{CEO} and f_{rep} are stabilized to a well defined reference, the frequency comb can be used as a "ruler". Various optical frequencies ν_{opt} can be measured and compared in a phase-coherent fashion, by simultaneous recording of the beat frequency f_x between a comb mode ν_n and the optical radiation under investigation.

The stabilized frequency comb can be used to measure laser radiation by heterodyne detection. The measured beat frequency f_x permits to calculate the laser frequency as $\nu_{\mathrm{L}} = mf_{\mathrm{rep}} + f_{\mathrm{CEO}} \pm f_x$. The integer number m and the sign in front of f_x are deduced from a measurement of the optical wavelength e.g. with a commercially available wavemeter.

Besides the very specific application to measure optical frequencies, frequency combs have wide application in spectroscopy and metrology. The precise compari-

son of two optical frequencies is another metrological application. If the comparison is based on a measurement of the frequency difference, a fraction of the noise of the microwave reference enters the measurement process. The fraction is equal to the ratio of the frequency difference and the absolute frequency. The frequency comb setup in our laboratory makes use of the transfer oscillator concept of Telle *et al.* [166], which is based on measurements of frequency ratios rather than frequency differences. The technique relies on fast radio frequency electronics to track and process the detected signals f_{CEO}, f_{rep}, and f_x, with a transfer bandwidth in the megahertz range. The technique is particularly advantageous, if the frequency comb does not provide sufficient controlling elements to stabilize the frequency comb with a high bandwidth to an optical reference e.g. a high finesse cavity. Besides the measurement of frequency ratios of optical radiation, signal processing can also be used to transfer the stability of an optical resonator to the microwave regime by controlling the frequency of a dielectric resonator oscillator (DRO) [115, 121]. Due to the high spectral purity of the optically stabilized microwave oscillator, it can replace the quartz-based local oscillator of a fountain clock and thus reduces the clock instability related with the Dick effect to an insignificant level. Following this idea, the reference cavity of the probe laser system was used as the reference for the DRO that served as the local oscillator of the caesium fountain clock CSF2 in the measurements discussed here [167]. A detailed description of the stabilization of the DRO and the decreased instability of the fountain clock is given in detail in Refs. [121, 168].

5.2 Measurement of the $^2\mathrm{S}_{1/2} \rightarrow {}^2\mathrm{F}_{7/2}$ Transition Frequency

5.2.1 Measurement in October 2010

In the first precise measurement of the $^2\mathrm{S}_{1/2}(F = 0) \rightarrow {}^2\mathrm{F}_{7/2}(F = 3)$ transition frequency at PTB in October 2010 versus the caesium fountain clock CSF1 in our laboratory [116, 117], the real-time extrapolation scheme discussed in section 3.2.4 was used to cancel the effect of the light shift by the probe laser system. Figure 5.2 shows the result of eight measurements of the extrapolated transition frequency obtained with different settings of the optical power resulting in a high intensity I_H and a low intensity I_L at the position of the ion. All results agree within the statistical uncertainty, which is determined by the frequency instability of CSF1 and the measurement time and yield no evidence for systematic shifts related to the choice of I_H and I_L. The observed fractional frequency instability of the measurement is compared in Fig. 5.3 to that obtained in a previous measurement of the quadrupole transition frequency with the same fountain [85]. The very good agreement of the data results from the fact that the combined instability is dominated by the con-

tribution of the fountain clock of $\approx 1.4 \times 10^{-13}/\sqrt{\tau(\mathrm{s})}$ to the fractional frequency instability, where τ is the measurement time. For the quadrupole transition, the frequency standard can be operated with an instability of about $7 \times 10^{-15}/\sqrt{\tau(\mathrm{s})}$, which is inferred from a measurement of the stability of the frequency difference between two independently operating interleaved stabilizations with the same interrogation period. The result was limited by the quantum projection noise and an improved instability for extended interrogation times is not expected due to the limited lifetime of the $^2\mathrm{D}_{3/2}(F = 2)$ of 53 ms [85,102]. Here, it is assumed that the observed instability of the frequency difference results from two oscillators with the same instability and that the instability of the frequency standard will decrease by $\sqrt{2}$, if it is operated without interleaved stabilization. For the frequency standard based on the octupole transition, a similar instability is expected. In comparison with the quadrupole standard, the instability is decreased due to the larger interrogation times, but the operation with interleaved stabilization is required to extrapolate the light shift.

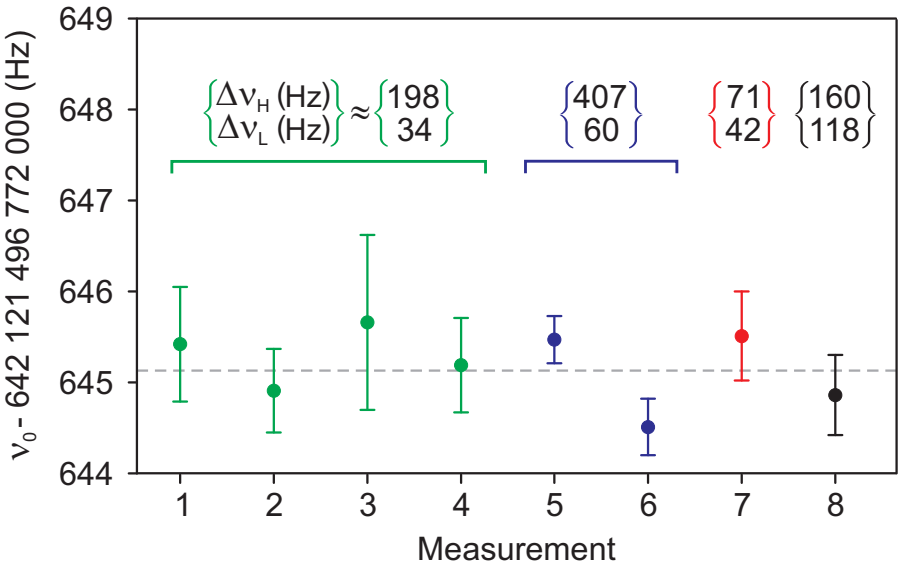

Figure 5.2: Measurements of the octupole transition frequency ν_0 for various combinations of probe pulse intensities and resulting time-averaged light shift magnitudes $\Delta\nu_H$ and $\Delta\nu_L$ used in an interleaved servo extrapolation scheme (see text). The error bars represent the statistical uncertainty, and the dashed gray line indicates the mean value that determines ν_0.

Table 5.1 summarizes the leading systematic frequency shifts and their uncertainty present during the measurement. The magnetic field was kept constant for all measurements, thus no suppression of a residual quadrupole shift or the tensorial quadratic Stark shift can be expected. For the frequency shift evaluation as

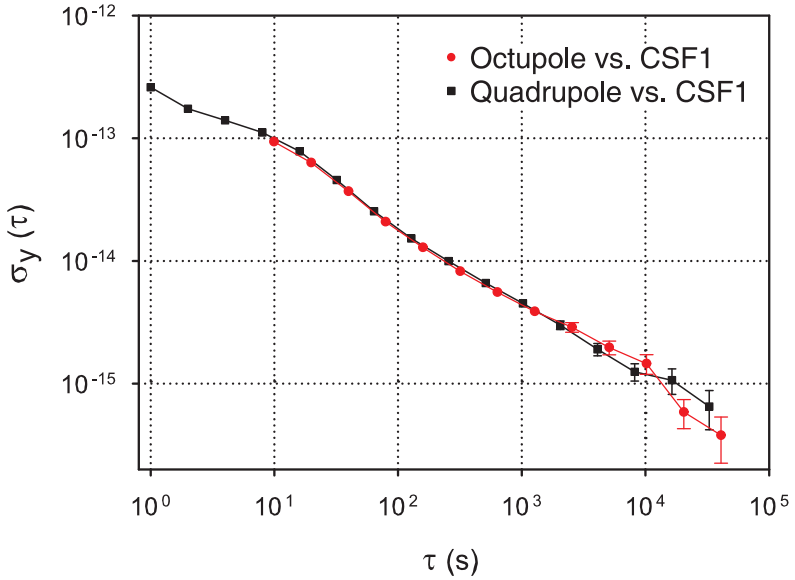

Figure 5.3: Comparison of the Allan deviation of the octupole transition frequency measurement and a previously performed measurement of the quadrupole transition frequency using the fountain clock CSF1 [85]. Both measurements show white frequency noise dependence and average as $sigma_y(\tau) \approx 1.4 \times 10^{-13}/\sqrt{\tau(\mathrm{s})}$

published in Ref. [29], the second-order Zeeman shift was calculated according to the sensitivity (1.72(3) mHz/μT) published in Ref. [126]. This value leads to an underestimation of the shift as discussed in section 3.4, where a different sensitivity of 2.03(2) mHz/μT has been determined.

The blackbody radiation shift during the measurement can now be calculated with significantly smaller uncertainty, as discussed in section 3.2.7, since the previously assigned uncertainty was mainly caused by the uncertainty of the differential static scalar polarizability. The fractional frequency shift of the octupole transition during the first measurement was $-111(50) \times 10^{-18}$.

To correct for the gravitational red shift, that appears since the caesium atoms are at an averaged height of 0.644(5) m above the Yb^+ ion in the trap, the measured frequency is increased by $70.3(6) \times 10^{-18}$.

The mean value of the results presented in Fig. 5.2 obtained with a total measurement time of 87 h determines the octupole transition frequency to be 642 121 496 772 645.13(51) Hz. Here, the total fractional uncertainty of 8.0×10^{-16} results from the combination of the statistical contribution (2.5×10^{-16}), the systematic uncertainty of the caesium fountain clock (7.6×10^{-16}) and the systematic uncertainty due to the realization of the octupole transition frequency (0.5×10^{-16}). The achieved total uncertainty represented an improvement by more than a factor

Effect	$\delta\nu/\nu_0$ (10^{-18})	u/ν_0 (10^{-18})
Light shift extrapolation	0	42
Quadrupole shift	0	22
Second-order Doppler shift	0	16
Quadratic dc Stark shift	0	4
Servo error	0	3
Blackbody radiation shift	−71	3
Second-order Zeeman shift	−40	1
Total	−111	50

Table 5.1: Leading fractional shifts $\delta\nu/\nu_0$ of the octupole transition frequency ν_0 and uncertainty contributions u/ν_0.

of 15 in comparison with the measurement presented in Fig. 3.1 and a factor of 20 with the previously published result [114].

5.2.2 Measurement in December 2012

The second precise measurement of the octupole transition frequency was performed in December 2012. In contrast to the first measurement, the controlled "hyper-Ramsey" spectroscopy was used to reduce the uncertainty due to the light shift and the transition frequency was averaged for three mutually orthogonal orientations of the magnetic field to cancel the quadrupole shift. Measurements of the motional sidebands allowed for an improved estimate on the residual second-order Doppler shift. Due to the limited resolution of the direct digital synthesis generator of 32 bits used for generating the RF signal for the pulsing AOM, a frequency correction of $-34.8(1) \times 10^{-18}$ was applied to obtain the expected offset of 76 MHz. All other leading systematic frequency shifts and uncertainty contributions present during the measurement of the octupole transition frequency are shown in Table 3.3.

Another significant difference to the first measurement was, that additionally PTB's second fountain clock CSF2 was operating, with a smaller systematic uncertainty. Furthermore, an optically stabilized microwave oscillator was used for this clock, allowing for a smaller frequency instability. Beside the microwave reference, an optical lattice clock was operating during the measurement and could be used for comparisons for about half of the entire measurement period [39, 134].

Figure 5.4 compares the observed fractional instabilities of the transition frequency measured with the two fountain clocks and the frequency ratio of the

$5s^2\,{}^1S_0 \rightarrow 5s5p\,{}^3P_0$ transition of ^{87}Sr and the octupole transition. The latter can be used to estimate the frequency instability of the single ion clock to be $5.3 \times 10^{-15}/\sqrt{\tau(\mathrm{s})}$, as the contribution of the optical lattice clock is expected to be significant smaller, resulting from the superior signal-to-noise ratio and the smaller short-term instability of their probe laser system [39]. It should be noted, that in half of all interrogation cycles of the frequency standard based on the octupole transition, Rabi spectroscopy was performed to control the step frequency of the HRS method, which was used for the rest of time. If Rabi interrogations are only performed for 1/4 of all measurement cycles, the instability should decrease by about 18% which reduces the measurement time by 33% to reach the same statistical uncertainty.

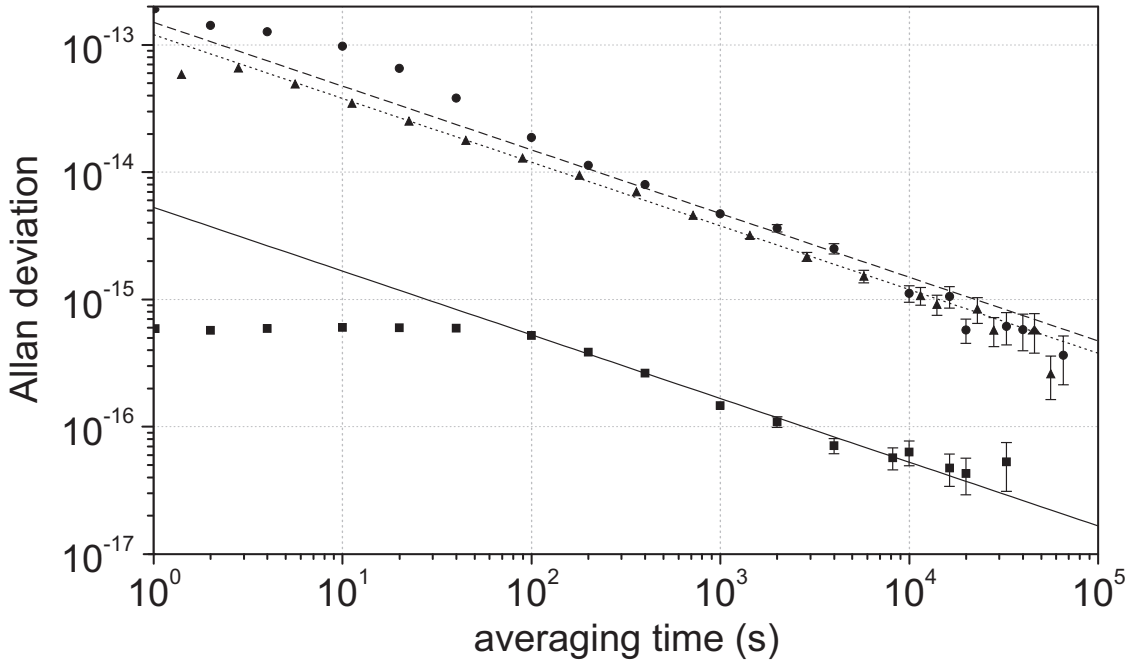

Figure 5.4: Allan deviation of the octupole transition frequency measured against CSF1 (triangles) and CSF2 (circles). The observed instability can be described by white frequency noise, and an averaging as $1.5 \times 10^{-13}/\sqrt{\tau(\mathrm{s})}$ and $1.2 \times 10^{-13}/\sqrt{\tau(\mathrm{s})}$ is found by linear regression for CSF1 and CSF2, respectively. The squares indicate the fractional instability of the frequency ratio between the octupole transition frequency and the $5s^2\,{}^1S_0 \rightarrow 5s5p\,{}^3P_0$ transition of ^{87}Sr, realized in a frequency standard with about 1500 atoms trapped in an optical lattice. Due to its superior frequency instability, the fitted $5.3 \times 10^{-15}/\sqrt{\tau(\mathrm{s})}$ dependence is attributed to the single ion clock.

The measurement of the absolute octupole transition frequency with the two fountain clocks was performed for about 350000 s between the 10$^{\text{th}}$ and 18$^{\text{th}}$ of December 2012 leading to relative statistical uncertainties of 2.5×10^{-16} and 2.0×10^{-16} for CSF1 and CSF2. The systematic uncertainties of the caesium fountains are 7.3×10^{-16} for CSF1 and 4.0×10^{-16} for CSF2. The results of both frequency measurements are corrected for the gravitational red shift. Averaging the two values and combing it with the 3.9×10^{-18} uncertainty due to the realization of the optical transition yields the frequency of the unperturbed octupole transition as $\nu_0(E3) = 642\ 121\ 496\ 772\ 645.34(25)$ Hz. The individual results of $\nu_0(E3) - 0.17(50)$ Hz and $\nu_0(E3)+0.06(29)$ Hz of CSF1 and CSF2 are in very good agreement and this measurement constitutes one of the most precise measurements of optical transition frequencies [30]. This result was also used together with the observed frequency ratio to determine the frequency of $5s^2\,{}^1S_0 \rightarrow 5s5p\,{}^3P_0$ transition realized in the optical lattice clock [39].

In between the first and the second measurement of the octupole transition frequency at PTB, its value was also determined using light-shift extrapolation at the National Physical Laboratory (UK) in a similar single ion experiment [169]. The published value of $\nu_0(E3) = 642\ 121\ 496\ 772\ 646.22(67)$ Hz is in good agreement with our result and the agreement can be improved, if the values are corrected according to the difference between the caesium fountain as evaluated by the Bureau International des Poids et Mesures (BIPM) relative to the international atomic timescale (TAI) [170]. Following the first two measurements of the octupole transition frequency with an accuracy comparable with the best realization of the SI second, the frequency has been endorsed to the list of secondary representations of the SI second. The recommended value of the frequency is 642 121 496 772 645.6 Hz with a fractional uncertainty of 1.3×10^{-15}. Figure 5.5 summarizes the absolute frequency measurements of the octupole transition.

5.3 Measurement of the $^2S_{1/2} \rightarrow {}^2D_{3/2}$ Transition Frequency

The frequency $\nu_0(E2)$ of the unperturbed quadrupole transition was determined from data comprising a total measurement time of 64.5 h within a 5-day period in August 2012 using CSF1 and CSF2 as the reference. The measurement is reported in detail in Ref. [121], and the measurement with CSF2 has been the first evaluation of an optical transition frequency, in which a fountain clock used the optically stabilized microwave as the local oscillator. The frequency $\nu_0(E2)$ was simultaneously measured by the fountain CSF1. Here the frequency difference between the CSF1 quartz oscillator and a hydrogen maser was registered by a phase comparator while the maser frequency was linked to the stabilized probe laser

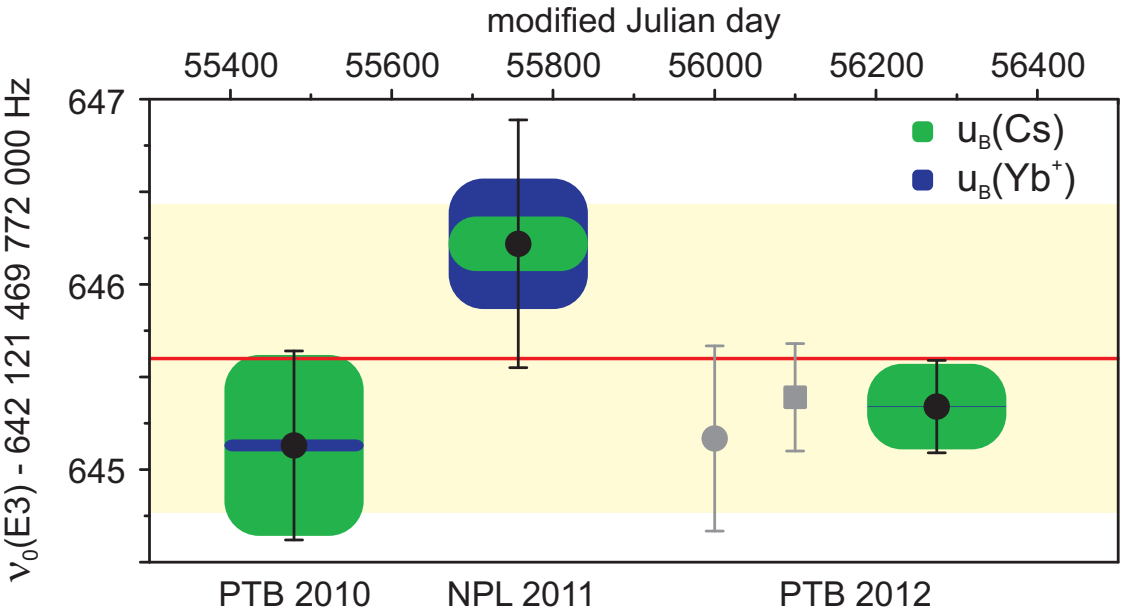

Figure 5.5: Results of absolute frequency measurements at PTB in 2010 [29], at NPL (UK) in 2011 [169] and in 2012 at PTB. The last measurement was performed versus two fountain clocks and the individual results of this measurement are plotted at a shifted position in gray. Here, the result of CSF1, which was also used in 2010, is indicated by a circle and that of CSF2 is shown as a square. The error bars indicate the total uncertainty, and the blue and green intervals illustrate the systematic uncertainty of the caesium fountain reference and the optical frequency standard. The red line shows the recommended frequency of the transition as a secondary representation of the SI second and the light yellow region the associated uncertainty [58].

frequency by means of the frequency comb generator. A significant contribution to the systematic uncertainty of a caesium fountain results from the collisional shift [167]. It is determined through an adiabatic passage technique that reduces the density of launched Cs clouds by exactly a factor of 2 [171, 172]. In all other measurements with caesium fountains presented here, the collisional shift and its uncertainty were evaluated in a separate measurement. During this measurement, however, for CSF2 a complete evaluation of this shift effect was performed. As a consequence, the frequency instability of the fountain clock was degraded and due to the limited total measurement time, the uncertainty of the collisional shift became the leading contribution to the systematic uncertainty of CSF2 and amounts to 5.5×10^{-16}. The leading systematic shift effects and the associated uncertainty contributions of the optical frequency standard are listed in Table 5.2.

Effect	$\delta\nu/\nu_0$ (10^{-18})	u/ν_0 (10^{-18})
Blackbody radiation shift	−524	102
Quadrupole shift and tensor second-order dc Stark shift	0	14
Scalar second-order dc Stark shift	−13	7
Second-order Zeeman shift	968	7
Second-order Doppler shift	−5	3
Servo error	0	36
Total	426	110

Table 5.2: Leading fractional shifts $\delta\nu/\nu_0(E2)$ and associated uncertainty contributions u/ν_0 of the single-ion frequency standard based on the quadrupole transition.

The systematic uncertainties of CSF1 and CSF2 during the measurement are 7.4×10^{-16} and 5.9×10^{-16} and the statistical uncertainties of the measurements are 3.2×10^{-16} and 2.8×10^{-16}. The fractional difference between the frequencies measured by CSF1 and CSF2 is 2.6×10^{-16}. The weighted mean yields the absolute frequency of the $^{171}\mathrm{Yb}^+$ $^2\mathrm{S}_{1/2}(F = 0) \rightarrow {}^2\mathrm{D}_{3/2}(F = 2)$ transition as $\nu_0(E2) = 688\,358\,979\,309\,307.82(36)$ Hz. The total uncertainty of 0.36 Hz (relative uncertainty 5.2×10^{-16}) is dominated by the systematic uncertainty of the caesium fountain references. Figure 5.6 shows that the present result is in good agreement with those obtained in the last 7 years [85, 173, 174] with different experimental configurations and systematic shift evaluation methods.

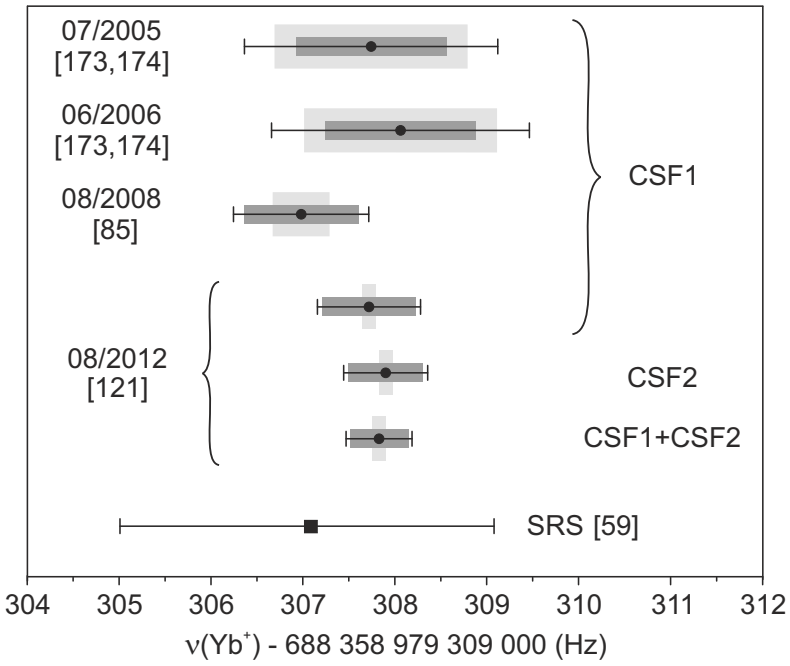

Figure 5.6: Results and uncertainties of the recent and of previous measurements of the absolute frequency $\nu_0(E2)$ of the quadrupole transition. The corresponding references are indicated in the figure. The black error bars show the total measurement uncertainty including the statistical contribution. The widths of the dark and light gray rectangles show the systematic uncertainties of the Cs reference and of the optical frequency standard, respectively. The data point "SRS" shows the recommended frequency and uncertainty of $\nu_0(E2)$ as a secondary representation of the SI second [58].

6 Conclusion and Outlook

A frequency standard based on the octupole transition of a single $^{171}Yb^{+}$ ion with a small systematic uncertainty has been realized. A new repump scheme in combination with a probe laser system with a low short-term instability permits the cycling interrogation on the reference transition. The so-called "hyper-Ramsey" spectroscopy with a real-time stabilization of its parameters reduces the previously limiting light shift by 5 orders of magnitude. The other *clock* transition of $^{171}Yb^{+}$, the quadrupole transition at 436 nm, can either serve as the reference in a frequency standard, or be employed to determine residual fields. In combination with the measured small sensitivities of the octupole transition frequency, a shift evaluation with very small uncertainties can be performed. From a measurement where infrared radiation was studied by the effect of near infrared lasers, the frequency shift induced by thermal radiation at room temperature can be corrected with high precision. As a result, the frequency standard is presently evaluated with a relative systematic uncertainty of 3.9×10^{-18}, which appears to be the smallest among all atomic clocks.

Following the first two measurements of the octupole transition frequency with an accuracy comparable with the best realization of the SI second at NPL and PTB [29, 169], the octupole transition frequency has been endorsed to the list of secondary representations of the SI second [58]. A later measurement versus the two fountain clocks of PTB is in very good agreement with the first result.

A further reduction of the systematic uncertainty of the octupole frequency standard can be achieved by proceeding the investigations of the Stark shift induced by infrared and near-infrared lasers. Here, a relative uncertainty below 1% seems to be within reach. A comparably low uncertainty can be expected from the evaluation of the effective temperature perturbing the ion, so that uncertainties related with thermal radiation at room temperature of not larger than 1×10^{-18} are expected within the next year. Finally, the thermal radiation shift might be canceled by cooling to cryogenic temperatures. If the cooling is performed with liquid nitrogen, the fractional shift at 77 K is only 3×10^{-19}.

Currently, the residual motion of the ion can only be evaluated precisely along one direction. Addressing this limitation, a second ion trap with improved optical access is presently under investigation. Of particular importance is a reduction of the heating rate, since the motional heating of the ion during its interrogation presently prevents significantly longer interaction times. A reduction of the heating rate is particularly advantageous if two ion clocks based on the octupole transition

are compared using the same probe laser as the local oscillator. In this case, relative frequency differences of the two systems can be observed with interrogation periods significantly larger than the coherence time of the probe laser system. This cancellation of the common-mode noise has been demonstrated for single ions in one trap [145] and is used for measurements between optical lattice clocks [34]. Due to the extraordinary long lifetime of the $^2F_{7/2}$ state, this technique can be employed to compare single-ion clocks with frequency instabilities that have so far only been demonstrated with optical lattice clocks.

The very good agreement of the octupole transition frequency measurement at PTB and NPL suggests to determine the frequency ratio of the two systems, which is independent from the caesium reference. Such a direct comparison might be performed based on satellite links, as it has recently been demonstrated between optical clocks at NICT in Japan and PTB [175]. Unfortunately, aside from large instabilities even for long averaging times, a significant contribution to the total uncertainty resulted from systematics of the employed satellite link. The presently most promising technique to link optical clocks on intracontinental scale are stabilized optical fibers [176, 177]. But even if each clock can realize the transition frequency with highest accuracy, and the link does not contribute, the agreement of the two clocks is concealed by the daily local altitude fluctuations and hence gravitational field variations at the 10^{-17} level [178]. On the other hand, this illustrates that optical clocks can actually be used to perform so-called "relativistic geodesy" [41].

The high accuracy of clock comparisons is also employed to test fundamental physics; the measurements presented in chapter 5 yield strict limits for temporal variations of fundamental constants. Even tighter constraints on the temporal variation of the fine structure constant α are expected from further comparisons of the particularly sensitive octupole transition frequency with others transition frequencies realized in optical clocks of high accuracy. This proposal is presently perused and it should be noted that comparisons with the quadrupole transition frequency can also yield small uncertainties for $d\alpha/dt$, as its uncertainty mainly results from the shift induced by thermal radiation which drops out if the frequency comparisons are performed separated in time under otherwise unchanged conditions.

Bibliography

[1] A. Einstein, Annalen der Physik **322**, 891 (1905).

[2] A. Scheibe and U. Adelsberger, Z. Phys. **127**, 416 (1950).

[3] A. Scheibe and U. Adelsberger, Z. Phys. **129**, 233 (1951).

[4] L. Essen, Ann. franç. Chronom. **1**, 343 (1955).

[5] L. Essen and J. V. L. Parry, Philosophical Transactions of the Royal Society of London. Series A, Mathematical and Physical Sciences **250**, 45 (1957).

[6] W. Markowitz, R. G. Hall, L. Essen, and J. V. L. Parry, Phys. Rev. Lett. **1**, 105 (1958).

[7] N. F. Ramsey, Phys. Rev. **78**, 695 (1950).

[8] M. A. Kasevich, E. Riis, S. Chu, and R. G. DeVoe, Phys. Rev. Lett. **63**, 612 (1989).

[9] A. Clairon, P. Laurent, G. Santarelli, S. Ghezali, S. Lea, and M. Bahoura, IEEE Trans. Instrum. Meas. **44**, 128 (1995).

[10] R. Wynands and S. Weyers, Metrologia **42**, 64 (2005).

[11] J. Guena, M. Abgrall, D. Rovera, P. Laurent, B. Chupin, M. Lours, G. Santarelli, P. Rosenbusch, M. Tobar, R. Li, K. Gibble, A. Clairon, and S. Bize, IEEE Trans. Ultrason. Ferroelect. Freq. Contr. **59**, 391 (2012).

[12] T. P. Heavner, E. A. Donley, F. Levi, G. Costanzo, T. E. Parker, J. H. Shirley, N. Ashby, S. Barlow, and S. R. Jefferts, Metrologia **51**, 174 (2014).

[13] D. Allan, Proceedings of the IEEE **54**, 221 (1966).

[14] J. E. Gray and D. Allan, in *28th Annual Symposium on Frequency Control. 1974*, 243 (1974).

[15] W. M. Itano, J. C. Bergquist, J. J. Bollinger, J. M. Gilligan, D. J. Heinzen, F. L. Moore, M. G. Raizen, and D. J. Wineland, Phys. Rev. A **47**, 3554 (1993).

[16] R. Drever, J. Hall, F. Kowalski, J. Hough, G. Ford, A. Munley, and H. Ward, Applied Physics B **31**, 97 (1983).

[17] B. C. Young, F. C. Cruz, W. M. Itano, and J. C. Bergquist, Phys. Rev. Lett. **82**, 3799 (1999).

[18] T. Kessler, C. Hagemann, C. Grebing, T. Legero, U. Sterr, F. Riehle, M. J. Martin, L. Chen, and J. Ye, Nat. Photon. **6**, 687 (2012).

[19] T. Udem, S. A. Diddams, K. R. Vogel, C. W. Oates, E. A. Curtis, W. D. Lee, W. M. Itano, R. E. Drullinger, J. C. Bergquist, and L. Hollberg, Phys. Rev. Lett. **86**, 4996 (2001).

[20] J. Stenger, H. Schnatz, Chr. Tamm, and H. R. Telle, Phys. Rev. Lett. **88**, 073601 (2002).

[21] T. Ido and H. Katori, Phys. Rev. Lett. **91**, 053001 (2003).

[22] M. Takamoto, F.-L. Hong, R. Higashi, and H. Katori, Nature **435**, 321 (2005).

[23] W. Paul and H. Steinwedel, Z. Naturforschung A **8**, 448 (1953).

[24] W. Neuhauser, M. Hohenstatt, P. Toschek, and H. Dehmelt, Phys. Rev. Lett. **41**, 233 (1978).

[25] J. C. Bergquist, R. G. Hulet, W. M. Itano, and D. J. Wineland, Phys. Rev. Lett. **57**, 1699 (1986).

[26] T. Rosenband, D. Hume, P. Schmidt, C. Chou, A. Brusch, L. Lorini, W. Oskay, R. Drullinger, T. Fortier, J. Stalnaker, S. Diddams, W. Swann, N. Newbury, W. Itano, D. Wineland, and J. Bergquist, Science **319**, 1808 (2008).

[27] C. W. Chou, D. B. Hume, J. C. J. Koelemeij, D. J. Wineland, and T. Rosenband, Phys. Rev. Lett. **104**, 070802 (2010).

[28] S. Falke, H. Schnatz, J. S. R. Vellore Winfred, T. Middelmann, S. Vogt, S. Weyers, B. Lipphardt, G. Grosche, F. Riehle, U. Sterr, and C. Lisdat, Metrologia **48**, 399 (2011).

[29] N. Huntemann, M. Okhapkin, B. Lipphardt, S. Weyers, Chr. Tamm, and E. Peik, Phys. Rev. Lett. **108**, 090801 (2012).

[30] R. Le Targat, L. Lorini, Y. Le Coq, M. Zawada, J. Guéna, M. Abgrall, M. Gurov, P. Rosenbusch, D. Rovera, B. Nagórny, R. Gartman, P. G. Westergaard, M. E. Tobar, M. Lours, G. Santarelli, A. Clairon, S. Bize, P. Laurent, P. Lemonde, and J. Lodewyck, Nature commun. **4**, 2109 (2013).

[31] N. Hinkley, J. Sherman, N. Phillips, M. Schioppo, N. Lemke, K. Beloy, M. Pizzocaro, C. Oates, and A. Ludlow, Science **341**, 1215 (2013).

[32] B. Bloom, T. Nicholson, J. Williams, S. Campbell, M. Bishof, X. Zhang, W. Zhang, S. Bromley, and J. Ye, Nature **506**, 71 (2014).

[33] P. Dubé, A. A. Madej, M. Tibbo, and J. E. Bernard, Phys. Rev. Lett. **112**, 173002 (2014).

[34] I. Ushijima, M. Takamoto, M. Das, T. Ohkubo, and H. Katori, arXiv preprint arXiv:1405.4071 (2014).

[35] T. L. Nicholson, M. J. Martin, J. R. Williams, B. J. Bloom, M. Bishof, M. D. Swallows, S. L. Campbell, and J. Ye, Phys. Rev. Lett. **109**, 230801 (2012).

[36] J. A. Sherman, N. D. Lemke, N. Hinkley, M. Pizzocaro, R. W. Fox, A. D. Ludlow, and C. W. Oates, Phys. Rev. Lett. **108**, 153002 (2012).

[37] K. Beloy, J. A. Sherman, N. D. Lemke, N. Hinkley, C. W. Oates, and A. D. Ludlow, Phys. Rev. A **86**, 051404 (2012).

[38] T. Middelmann, S. Falke, C. Lisdat, and U. Sterr, Phys. Rev. Lett. **109**, 263004 (2012).

[39] S. Falke, N. Lemke, C. Grebing, B. Lipphardt, S. Weyers, V. Gerginov, N. Huntemann, C. Hagemann, A. Al-Masoudi, S. Häfner, S. Vogt, U. Sterr, and C. Lisdat, New J. Phys. **16**, 073023 (2014).

[40] T. Middelmann, C. Lisdat, S. Falke, J. Winfred, F. Riehle, and U. Sterr, IEEE Trans. Instrum. Meas. **60**, 2550 (2011).

[41] A. Bjerhammar, Bulletin géodésique **59**, 207 (1985).

[42] C. Will, Living Rev. Relativity **9** (2006).

[43] J. Guéna, M. Abgrall, D. Rovera, P. Rosenbusch, M. E. Tobar, P. Laurent, A. Clairon, and S. Bize, Phys. Rev. Lett. **109**, 080801 (2012).

[44] E. Peik, B. Lipphardt, H. Schnatz, T. Schneider, Chr. Tamm, and S. G. Karshenboim, Phys. Rev. Lett. **93**, 170801 (2004).

[45] T. M. Fortier, N. Ashby, J. C. Bergquist, M. J. Delaney, S. A. Diddams, T. P. Heavner, L. Hollberg, W. M. Itano, S. R. Jefferts, K. Kim, F. Levi, L. Lorini, W. H. Oskay, T. E. Parker, J. Shirley, and J. E. Stalnaker, Phys. Rev. Lett. **98**, 070801 (2007).

[46] S. Blatt, A. D. Ludlow, G. K. Campbell, J. W. Thomsen, T. Zelevinsky, M. M. Boyd, J. Ye, X. Baillard, M. Fouché, R. Le Targat, A. Brusch, P. Lemonde, M. Takamoto, F.-L. Hong, H. Katori, and V. V. Flambaum, Phys. Rev. Lett. **100**, 140801 (2008).

[47] E. Peik, Nucl. Phys. B (Proc. Suppl.) **203**, 18 (2010).

[48] V. A. Dzuba and V. V. Flambaum, Phys. Rev. A **77**, 012515 (2008).

[49] K. Sugiyama and J. Yoda, Phys. Rev. A **55**, R10 (1997).

[50] N. Timoney, I. Baumgart, M. Johanning, A. F. Varon, M. B. Plenio, A. Retzker, and C. Wunderlich, Nature **476**, 185 (2011).

[51] K. Pyka, J. Keller, H. Partner, R. Nigmatullin, T. Burgermeister, D. Meier, K. Kuhlmann, A. Retzker, M. Plenio, W. Zurek *et al.*, Nature commun. **4**, 2571 (2013).

[52] R. Islam, C. Senko, W. Campbell, S. Korenblit, J. Smith, A. Lee, E. Edwards, C.-C. Wang, J. Freericks, and C. Monroe, Science **340**, 583 (2013).

[53] M. Steiner, H. M. Meyer, C. Deutsch, J. Reichel, and M. Köhl, Phys. Rev. Lett. **110**, 043003 (2013).

[54] S. C. Webster, S. Weidt, K. Lake, J. J. McLoughlin, and W. K. Hensinger, Phys. Rev. Lett. **111**, 140501 (2013).

[55] N. Shiga, M. Mizuno, K. Kido, P. Phoonthong, and K. Okada, arXiv preprint arXiv:1401.1288 (2014).

[56] N. Yu and L. Maleki, Phys. Rev. A **61**, 022507 (2000).

[57] Chr. Tamm, D. Engelke, and V. Bühner, Phys. Rev. A **61**, 053405 (2000).

[58] www.bipm.org/en/publications/mep.html.

[59] M. Roberts, P. Taylor, G. P. Barwood, P. Gill, H. A. Klein, and W. R. C. Rowley, Phys. Rev. Lett. **78**, 1876 (1997).

[60] E. Biémont, J.-F. Dutrieux, I. Martin, and P. Quinet, J. Phys. B **31**, 3321 (1998).

[61] W. C. Martin, R. Zalubas, and L. Hagan, *Atomic Energy Levels –The Rare-Earth Elements*, Nat. Bur. Stand., U.S.1978 (1978).

[62] S. G. Porsev, M. S. Safronova, and M. G. Kozlov, Phys. Rev. A **86**, 022504 (2012).

[63] V. A. Dzuba, V. V. Flambaum, and M. V. Marchenko, Phys. Rev. A **68**, 022506 (2003).

[64] P. J. Blythe, S. A. Webster, K. Hosaka, and P. Gill, J. Phys. B **36**, 981 (2003).

[65] I. Sherstov, M. Okhapkin, B. Lipphardt, Chr. Tamm, and E. Peik, Phys. Rev. A **81**, 021805 (2010).

[66] H. G. Dehmelt, Phys. Rev. **103**, 1125 (1956).

[67] E. C. Beaty, Journal of Applied Physics **61**, 2118 (1987).

[68] D. Bate, K. Dholakia, R. Thompson, and D. Wilson, Journal of Modern Optics **39**, 305 (1992).

[69] D. J. Berkeland, J. D. Miller, J. C. Bergquist, W. M. Itano, and D. J. Wineland, J. Appl. Phys. **83**, 5025 (1998).

[70] T. Schneider, E. Peik, and Chr. Tamm, Phys. Rev. Lett. **94**, 230801 (2005).

[71] D. J. Wineland, R. E. Drullinger, and F. L. Walls, Phys. Rev. Lett. **40**, 1639 (1978).

[72] W. D. Phillips, Rev. Mod. Phys. **70**, 721 (1998).

[73] D. J. Wineland and W. M. Itano, Phys. Rev. A **20**, 1521 (1979).

[74] W. M. Itano, J. C. Bergquist, J. J. Bollinger, and D. J. Wineland, Physica Scripta **1995**, 106 (1995).

[75] D. Leibfried, R. Blatt, C. Monroe, and D. Wineland, Rev. Mod. Phys. **75**, 281 (2003).

[76] Chr. Tamm, Applied Physics B **56**, 295 (1993).

[77] A. S. Bell, P. Gill, H. A. Klein, A. P. Levick, Chr. Tamm, and D. Schnier, Phys. Rev. A **44**, R20 (1991).

[78] V. Bühner, Schmale spektrale Strukturen in der Resonanzfluoreszenz eines gespeicherten Atoms, Ph.D. thesis, Universität Hannover (2001).

[79] S. Olmschenk, D. Hayes, D. N. Matsukevich, P. Maunz, D. L. Moehring, K. C. Younge, and C. Monroe, Phys. Rev. A **80**, 022502 (2009).

[80] T. Schneider, Optical frequency standard with a single $^{171}Yb^{+}$ ion, Ph.D. thesis, Universität Hannover (2005).

[81] P. Dubé, A. A. Madej, Z. Zhou, and J. E. Bernard, Phys. Rev. A **87**, 023806 (2013).

[82] F. Diedrich, J. C. Bergquist, W. M. Itano, and D. J. Wineland, Phys. Rev. Lett. **62**, 403 (1989).

[83] C. Balzer, A. Braun, T. Hannemann, C. Paape, M. Ettler, W. Neuhauser, and C. Wunderlich, Phys. Rev. A **73**, 041407 (2006).

[84] M. Johanning, A. Braun, D. Eiteneuer, C. Paape, C. Balzer, W. Neuhauser, and C. Wunderlich, Applied Physics B **103**, 327 (2011).

[85] Chr. Tamm, S. Weyers, B. Lipphardt, and E. Peik, Phys. Rev. A **80**, 043403 (2009).

[86] H. G. Dehmelt, Bull. Am. Phys. Soc. **20**, 60 (1975).

[87] P. Gill, H. A. Klein, A. P. Levick, M. Roberts, W. R. C. Rowley, and P. Taylor, Phys. Rev. A **52**, R909 (1995).

[88] P. Taylor, M. Roberts, S. V. Gateva-Kostova, R. B. M. Clarke, G. P. Barwood, W. R. C. Rowley, and P. Gill, Phys. Rev. A **56**, 2699 (1997).

[89] P. Taylor, M. Roberts, G. M. Macfarlane, G. P. Barwood, W. R. C. Rowley, and P. Gill, Phys. Rev. A **60**, 2829 (1999).

[90] R. W. Berends, E. H. Pinnington, B. Guo, and Q. Ji, J. Phys. B **26**, L701 (1993).

[91] T. Hänsch and B. Couillaud, Optics Communications **35**, 441 (1980).

[92] K. Numata, A. Kemery, and J. Camp, Phys. Rev. Lett. **93**, 250602 (2004).

[93] Y. Y. Jiang, A. D. Ludlow, N. D. Lemke, F. W., J. A. Sherman, L.-S. Ma, and C. W. Oates, Nat. Photon. **5**, 158 (2011).

[94] J. Millo, D. V. Magalhães, C. Mandache, Y. Le Coq, E. M. L. English, P. G. Westergaard, J. Lodewyck, S. Bize, P. Lemonde, and G. Santarelli, Phys. Rev. A **79**, 053829 (2009).

[95] J.-P. Richard and J. J. Hamilton, Review of Scientific Instruments **62**, 2375 (1991).

[96] S. Seel, R. Storz, G. Ruoso, J. Mlynek, and S. Schiller, Phys. Rev. Lett. **78**, 4741 (1997).

[97] T. Legero, T. Kessler, and U. Sterr, J. Opt. Soc. Am. B **27**, 914 (2010).

[98] T. Legero, Private communication.

[99] T. Nazarova, F. Riehle, and U. Sterr, Applied Physics B **83**, 531 (2006).

[100] Chr. Tamm, Private communication.

[101] D. L. Platus, in *SPIE's International Symposium on Optical Science, Engineering, and Instrumentation*, volume 3786, 98 (1999).

[102] E. Peik, T. Schneider, and Chr. Tamm, J. Phys. B **39**, 145 (2006).

[103] G. J. Dick, in *Proceedings of the 19th Annual Precise Time and Time Interval (PTTI) Applications and Planning Meeting*, 133 (1988).

[104] A. Einstein, Annalen der Physik **328**, 197 (1907).

[105] H. E. Ives and G. R. Stilwell, J. Opt. Soc. Am. **28**, 215 (1938).

[106] H. J. Hay, J. P. Schiffer, T. E. Cranshaw, and P. A. Egelstaff, Phys. Rev. Lett. **4**, 165 (1960).

[107] W. Kündig, Phys. Rev. **129**, 2371 (1963).

[108] D. Hasselkamp, E. Mondry, and A. Scharmann, Zeitschrift für Physik A Atoms and Nuclei **289**, 151 (1979).

[109] P. T. H. Fisk, Reports on Progress in Physics **60**, 761 (1997).

[110] J. R. P. Angel and P. G. H. Sandars, Proceedings of the Royal Society of London. Series A, Mathematical and Physical Sciences **305**, 125 (1968).

[111] W. Itano, J. Res. Natl. Inst. Stand. Technol. **105**, 829 (2000).

[112] S. N. Lea, S. A. Webster, and G. P. Barwood, in *Proceedings of the 20th European Frequency and Time Forum*, 302 (2006).

[113] V. A. Dzuba, A. Kozlov, and V. V. Flambaum, arXiv preprint arXiv:1403.5002 (2014).

[114] K. Hosaka, S. A. Webster, A. Stannard, B. R. Walton, H. S. Margolis, and P. Gill, Phys. Rev. A **79**, 033403 (2009).

[115] B. Lipphardt, G. Grosche, U. Sterr, Chr. Tamm, S. Weyers, and H. Schnatz, IEEE Trans. Instrum. Meas. **58**, 1258 (2009).

[116] S. Weyers, U. Hübner, R. Schröder, Chr. Tamm, and A. Bauch, Metrologia **38**, 343 (2001).

[117] S. Weyers, A. Bauch, R. Schröder, and Chr. Tamm, in *Proceedings of the 6th Symposium Frequency Standards and Metrology*, 64, World Scientific (2002).

[118] P. Balling, Doležal, and C. Sanner, To be published.

[119] G. P. Barwood, H. S. Margolis, G. Huang, P. Gill, and H. A. Klein, Phys. Rev. Lett. **93**, 133001 (2004).

[120] L. Olschewski, Zeitschrift für Physik **249**, 205 (1972).

[121] Chr. Tamm, N. Huntemann, B. Lipphardt, V. Gerginov, N. Nemitz, M. Kazda, S. Weyers, and E. Peik, Phys. Rev. A **89**, 023820 (2014).

[122] I. I. Sobelman, *Atomic Spectra and Radiative Transitions*, Springer-Verlag, Heidelberg, 2nd edition (1992).

[123] G. H. Gossel, V. A. Dzuba, and V. V. Flambaum, Phys. Rev. A **88**, 034501 (2013).

[124] P. Fisk, M. Sellars, and C. Lawn, M.A.and Coles, IEEE Trans. Ultrason. Ferroelect. Freq. Contr. **44**, 344 (1997).

[125] W. F. Meggers, Journal of Research of the National Bureau of Standards **71A**, 396 (1967).

[126] K. Hosaka, S. A. Webster, P. J. Blythe, A. Stannard, D. Beaton, H. S. Margolis, S. N. Lea, and P. Gill, IEEE Trans. Instrum. Meas. **54**, 759 (2005).

[127] L. Cutler, R. Giffard, and M. McGuire, Applied Physics B **36**, 137 (1985).

[128] J. Vetter, M. Stuke, and E. Weber, Zeitschrift für Physik A Atoms and Nuclei **273**, 129 (1975).

[129] Chr. Tamm, D. Schnier, and A. Bauch, Applied Physics B **60**, 19 (1995).

[130] J. J. Bollinger, D. J. Heinzen, W. M. Itano, S. L. Gilbert, and D. J. Wineland, IEEE Trans. Instrum. Meas. **40**, 126 (1991).

[131] H. Hotop, M.-W. Ruf, A. J. Yencha, and B. Fricke, Annalen der Physik **502**, 635 (1990).

[132] L.-S. Ma, P. Jungner, J. Ye, and J. L. Hall, Opt. Lett. **19**, 1777 (1994).

[133] A. Härter, A. Krükow, A. Brunner, and J. Hecker Denschlag, Applied Physics B **114**, 275 (2014).

[134] S. Falke, M. Misera, U. Sterr, and C. Lisdat, Applied Physics B **107**, 301 (2012).

[135] D. Kleppner, R. Vessot, and N. Ramsey, Astrophysics and Space Science **6**, 13 (1970).

[136] R. F. C. Vessot, M. W. Levine, E. M. Mattison, E. L. Blomberg, T. E. Hoffman, G. U. Nystrom, B. F. Farrel, R. Decher, P. B. Eby, C. R. Baugher, J. W. Watts, D. L. Teuber, and F. D. Wills, Phys. Rev. Lett. **45**, 2081 (1980).

[137] N. K. Pavlis and M. A. Weiss, Metrologia **40**, 66 (2003).

[138] A. Yamaguchi, M. Fujieda, M. Kumagai, H. Hachisu, S. Nagano, Y. Li, T. Ido, T. Takano, M. Takamoto, and H. Katori, Applied Physics Express **4**, 082203 (2011).

[139] C. W. Chou, D. B. Hume, T. Rosenband, and D. J. Wineland, Science **329**, 1630 (2010).

[140] C. Degenhardt, T. Nazarova, C. Lisdat, H. Stoehr, U. Sterr, and F. Riehle, IEEE Trans. Instrum. Meas. **54**, 771 (2005).

[141] I. Stefanskii, S. Mikhalevich, Y. Burak, and V. Sapovskii, Journal of Applied Spectroscopy **51**, 790 (1989).

[142] N. F. Ramsey, Rev. Mod. Phys. **62**, 541 (1990).

[143] H. Häffner, C. Roos, and R. Blatt, Physics Reports **469**, 155 (2008).

[144] P. T. H. Fisk, M. Sellars, M. Lawn, C. Coles, A. Mann, and D. Blair, IEEE Trans. Instrum. Meas. **44**, 113 (1995).

[145] C. W. Chou, D. B. Hume, M. J. Thorpe, D. J. Wineland, and T. Rosenband, Phys. Rev. Lett. **106**, 160801 (2011).

[146] Y. Millerioux, D. Touahri, L. Hilico, A. Clairon, R. Felder, F. Biraben, and B. de Beauvoir, Optics Communications **108**, 91 (1994).

[147] T. Badr, M. D. Plimmer, P. Juncar, M. E. Himbert, Y. Louyer, and D. J. E. Knight, Phys. Rev. A **74**, 062509 (2006).

[148] T. Zanon-Willette, A. D. Ludlow, S. Blatt, M. M. Boyd, E. Arimondo, and J. Ye, Phys. Rev. Lett. **97**, 233001 (2006).

[149] C. G. Parthey, A. Matveev, J. Alnis, B. Bernhardt, A. Beyer, R. Holzwarth, A. Maistrou, R. Pohl, K. Predehl, T. Udem, T. Wilken, N. Kolachevsky, M. Abgrall, D. Rovera, C. Salomon, P. Laurent, and T. W. Hänsch, Phys. Rev. Lett. **107**, 203001 (2011).

[150] A. V. Taichenachev, V. I. Yudin, C. W. Oates, C. W. Hoyt, Z. W. Barber, and L. Hollberg, Phys. Rev. Lett. **96**, 083001 (2006).

[151] X. Baillard, M. Fouché, R. L. Targat, P. G. Westergaard, A. Lecallier, Y. L. Coq, G. D. Rovera, S. Bize, and P. Lemonde, Opt. Lett. **32**, 1812 (2007).

[152] N. Poli, Z. W. Barber, N. D. Lemke, C. W. Oates, L. S. Ma, J. E. Stalnaker, T. M. Fortier, S. A. Diddams, L. Hollberg, J. C. Bergquist, A. Brusch, S. Jefferts, T. Heavner, and T. Parker, Phys. Rev. A **77**, 050501 (2008).

[153] T. Akatsuka, M. Takamoto, and H. Katori, Phys. Rev. A **81**, 023402 (2010).

[154] V. I. Yudin, A. V. Taichenachev, C. W. Oates, Z. W. Barber, N. D. Lemke, A. D. Ludlow, U. Sterr, C. Lisdat, and F. Riehle, Phys. Rev. A **82**, 011804 (2010).

[155] L. Hollberg and J. L. Hall, Phys. Rev. Lett. **53**, 230 (1984).

[156] A. Taichenachev, V. Yudin, C. Oates, Z. Barber, N. Lemke, A. Ludlow, U. Sterr, C. Lisdat, and F. Riehle, JETP Letters **90**, 713 (2010).

[157] W. S. Warren and A. H. Zewail, J. Chem. Phys. **78**, 2279 (1983).

[158] L. Allen and J. H. Eberly, *Optical Resonance and Two-Level Atoms*, Dover publications, New York (1987).

[159] N. F. Ramsey and H. B. Silsbee, Phys. Rev. **84**, 506 (1951).

[160] V. Letchumanan, P. Gill, E. Riis, and A. G. Sinclair, Phys. Rev. A **70**, 033419 (2004).

[161] K. Tabatchikova, A. Taichenachev, and V. Yudin, JETP Letters **97**, 311 (2013).

[162] V. I. Yudin, Private communication.

[163] D. A. Jennings, J. L. Hall, H. P. Layer, C. R. Pollock, F. R. Petersen, R. E. Drullinger, K. M. Evenson, and J. S. Wells, Opt. Lett. **8**, 136 (1983).

[164] H. Schnatz, B. Lipphardt, J. Helmcke, F. Riehle, and G. Zinner, Phys. Rev. Lett. **76**, 18 (1996).

[165] T. W. Hänsch, Rev. Mod. Phys. **78**, 1297 (2006).

[166] H. Telle, B. Lipphardt, and J. Stenger, Applied Physics B **74**, 1 (2002).

[167] V. Gerginov, N. Nemitz, S. Weyers, R. Schröder, D. Griebsch, and R. Wynands, Metrologia **47**, 65 (2010).

[168] S. Weyers, B. Lipphardt, and H. Schnatz, Phys. Rev. A **79**, 031803 (2009).

[169] S. A. King, R. M. Godun, S. A. Webster, H. S. Margolis, L. A. M. Johnson, K. Szymaniec, P. E. G. Baird, and P. Gill, New J. Phys. **14**, 013045 (2012).

[170] http://www.bipm.org/en/scientific/tai/ftp_server/publication.html.

[171] S. Weyers, R. Schröder, and R. Wynands, in *Proceedings of the 20th European Frequency and Time Forum*, 173 (2006).

[172] J. Shirley, F. Levi, T. Heavner, D. Calonico, D.-H. Yu, and S. Jefferts, IEEE Trans. Ultrason. Ferroelect. Freq. Contr. **53**, 2376 (2006).

[173] E. Peik, B. Lipphardt, H. Schnatz, R. Wynands, S. Weyers, T. Schneider, T. Schneider, and Chr. Tamm, in *Proceedings of the Eleventh Marcel Grossmann Meeting on General Relativity*, 941 (2008).

[174] Chr. Tamm, B. Lipphardt, H. Schnatz, R. Wynands, S. Weyers, T. Schneider, and E. Peik, IEEE Trans. Instrum. Meas. **56**, 601 (2007).

[175] H. Hachisu, M. Fujieda, S. Nagano, T. Gotoh, A. Nogami, T. Ido, S. Falke, N. Huntemann, C. Grebing, B. Lipphardt *et al.*, Optics Lett. in press, arXiv preprint arXiv:1403.6285 (2014).

[176] K. Predehl, G. Grosche, S. M. F. Raupach, S. Droste, O. Terra, J. Alnis, T. Legero, T. W. Hänsch, T. Udem, R. Holzwarth, and H. Schnatz, Science **336**, 441 (2012).

[177] S. Droste, F. Ozimek, T. Udem, K. Predehl, T. W. Hänsch, H. Schnatz, G. Grosche, and R. Holzwarth, Phys. Rev. Lett. **111**, 110801 (2013).

[178] D. Kleppner, Physics Today **59**, 10 (2006).

Danksagung

Die vorliegende Arbeit wäre ohne die Unterstützung zahlreicher Personen und ohne die hervorragenden Arbeitsumgebungen, die sich über viele Jahre entwickelt haben, sicherlich nicht möglich gewesen. Für beides möchte ich mich an dieser Stelle bedanken.

Zunächst gilt mein Dank Ekkehard Peik, der mir die Möglichkeit gab, auf diesem höchst spannenden Themenbereich zu forschen, mich immer unterstützte und sich stets bemühte, möglichst optimale Arbeitsbedingungen zu schaffen. Außerdem möchte ich mich für seine immer hilfsbereite und freundliche Art bedanken und das Vertrauen in mich, unsere Resultate bei verschiedensten Gelegenheiten zu präsentieren.

In ganz ähnlicher Weise gilt mein Dank Christian Tamm, der mich bei meiner Arbeit am Frequenznormal betreute und von dem ich sehr viel lernen konnte. Durch seine kontinuierliche Entwicklung des Frequenznormals, trägt er einen wesentlichen Anteil an den schönen Resultaten und der hervorragenden experimentellen Umgebung, die mir geboten wurde.

Bei Burghard Lipphardt bedanke ich mich für die Unterstützung bei Allem rund um Elektronik und den Frequenzkamm. Neben seiner sympathischen Art, die für eine besonders positive Atmosphäre bei der Arbeit in der Uhrenhalle sorgte, möchte ich ihm für seine große Leidenschaft danken, die eine dauerhafte Verfügbarkeit des Frequenzkamms ermöglichte, der wiederum für die Spektroskopie des Oktupolübergangs so wichtig ist.

Jedoch würde der Frequenzkamm keine Hilfestellung leisten können, ohne eine solide Referenz. Was mich zu den nächsten *Bewohnern* der Uhrenhalle bringt. Ich möchte mich bei Vladislav Gerginov und Stefan Weyers für die tolle Zusammenarbeit bedanken.

Maxim Okhapkin war ein hervorragender Lehrer im Labor, als es darum ging, den neuen Uhrenlaser aufzubauen und sorgte auch außerhalb des Labors für eine unterhaltsame Atmosphäre. Ich wünsche ihm, dass er den Übergang bald finden wird.

In der letzten Phase der Arbeit bereicherte Christian Sanner unser Team, was ich als großen Gewinn sehe. Ich schätze ihn nicht nur als fachlich exzellenten und sym-

pathischen Kollegen im Labor und Büro, sondern auch für seine stets hilfsbereite Art, die sich auch in einer Durchsicht dieser Arbeit widerspiegelt, vielen Dank!

Beim gesamten Team um die Strontium Gitteruhr und den Frequenzkamm im Fachbereich 4.3 möchte ich mich für die tolle Zusammenarbeit bedanken. Ich hoffe, dass die langen Nächte gemeinsam mit Christian Lisdat, Stephan Falke, Nathan Lemke, Christian Grebing, Ali Al-Masoudi, Sebastian Häffner bald belohnt werden. Bei Uwe Stehr möchte ich mich bedanken für die Diskussionen zu "hyper-Ramsey" und für das Ausleihen eines Laser für die Untersuchungen der Lichtverschiebung. Für eine ebenso freundliche und unkomplizierte Überlassung eines anderen Lasers bedanke ich mich bei Sebastian Raupach. Bei Piet Schmidt bedanke ich mich für die immer freundliche Unterstützung und die Übernahme der Gutachtertätigkeit. Letzteres gilt in gleicher Form für Alan Madej, der mir als sehr symphatischer und gewissenhafter Wissenschaftler bekannt ist.

Einen wesentlichen Beitrag zum Erfolg unserer Untersuchungen leisteten auch viele andere Mitarbeiter des Fachbereichs Zeit und Frequenz. Ganz persönlich möchte ich mich bei Andreas Hoppmann für das immer beispielhafte Umsetzen aller Wünsche im Bereich Elektronik bedanken. Für die zuverlässige Arbeit der mechanischen Werkstatt gilt mein Dank Thomas Leder und Martin Menzel.

Neben dem hervorragenden Arbeitsumfeld trägt einen wesentlichen Anteil am gelingen der Arbeit mein persönliches Umfeld. Meinen Eltern danke ich für ihre dauerhafte Unterstützung und ihr großes Verständnis. Zuletzt möchte ich mich bei dem Menschen bedanken, der mich in den letzten Jahren durch alle Höhen und Tiefen begleitet hat und immer dafür gesorgt hat, dass es mehr Sonnenschein als Regen gab, Danke Gini!